

DEPARTMENT OF PHYSICS, UNIVERSITY OF JYVÄSKYLÄ

**JET TRANSVERSE MOMENTUM DISTRIBUTIONS
MEASURED BY ALICE**

**BY
TOMAS SNELLMAN**

PHD thesis

Supervisors: Jan Rak, Dong Jo Kim

Jyväskylä, Finland
December, 2018

3 Contents

4	1	Introduction	3
5	1.1	Quantum chromodynamics	4
6	1.1.1	Foundation of QCD	4
7	1.1.2	Asymptotic Freedom	5
8	1.2	Heavy ion physics	9
9	1.2.1	History	9
10	1.3	Features of Heavy-Ion Collisions	11
11	1.3.1	Collision Geometry	11
12	1.3.2	Nuclear Geometry	12
13	1.3.3	Hydrodynamical Modelling	15
14	1.4	Flow	18
15	1.4.1	Anisotropic Flow	19
16	1.4.2	High p_T Phenomena	20
17	1.5	Hard processes	21
18	1.5.1	pQCD factorization	21
19	1.5.2	Jet hadronisation	23
20	1.5.3	Jet energy loss	27
21	1.5.4	Monte Carlo Implementations	36
22	1.6	QGP in Small systems	36
23	1.6.1	Collective phenomena	37
24	1.6.2	Absence of jet quenching	38
25	1.6.3	Centrality determination in small systems	39
26	2	Experimental setup and data samples	43
27	3	Experimental Details	44
28	3.1	CERN	44
29	3.2	Large Hadron Collider	46
30	3.2.1	LHC experiments	47
31	3.3	ALICE	47
32	3.3.1	Tracking	48
33	3.3.2	TPC	50
34	3.3.3	TPC upgrade	50
35	3.3.4	Optical scanning	53
36	3.3.5	Particle identification	53

37	3.3.6	Electromagnetic Calorimeter	54
38	3.3.7	Forward detectors	55
39	3.3.8	Muon spectrometer	56
40	3.3.9	Trigger	56
41	4	Event and track selection	57
42	5	Analysis method	57
43	5.1	Jet Finding	57
44	5.1.1	Anti k_T algorithm	57
45	5.2	j_T	58
46	5.2.1	1 over j_T	58
47	5.3	Unfolding	59
48	5.3.1	Bayesian unfolding	60
49	5.3.2	Toy Monte Carlo	60
50	5.3.3	Pythia Response matrices	61
51	5.3.4	2D response matrices	62
52	5.3.5	Unfolding algorithm	62
53	5.3.6	Effect of number of iterations	62
54	5.3.7	Effect of different prior	63
55	5.3.8	Effect of p_T truncation	63
56	5.3.9	Unfolding closure test	63
57	5.4	Background	65
58	5.4.1	Perpendicular cone background	66
59	5.4.2	Random background	66
60	5.4.3	Auto-correlations	69
61	5.5	Fitting	69
62	6	Systematic uncertainties	70
63	7	TPC Upgrade?	72
64	8	Systematic errors	73
65	8.1	Background subtraction	73
66	8.2	Unfolding	73
67	8.3	Tracking	73
68	8.4	Combining systematics	73
69	9	Results	76
70	9.1	statistics	76
71	9.2	Data	76
72	9.3	Inclusive results	76

73	9.4	Background	77
74	9.5	Comparison between A and C side	77
75	9.6	Subtracted signal	77
76	9.7	Fitting	78
77	9.7.1	Results	78
78	9.8	Comparison to dihadron results	78
79	9.9	Different R parameters	82
80	10	Discussion	85
81	10.1	Discussion	85
82	10.1.1	Dihadron j_T	85
83	11	Summary	89

84 List of Figures

85	1	QCD phase diagram	7
86	2	η/s vs $(T - T_c)/T_c$	8
87	3	The definitions of the Reaction Plane and Participant Plane coordinate systems	11
88	4	Interaction between partons in central and peripheral collisions.	12
89	5	An illustration of the multiplicity distribution in ALICE measurement with centrality classes.	13
90	6	The results of one Glauber Monte Carlo simulation.	16
91	7	Schematic representation of a heavy-ion collision	17
92	8	Charged particle spectra	18
93	9	Illustration of flow in momentum space in central and peripheral collisions.	19
94	10	QCD Leading Order	21
95	11	Hard scattering	21
96	12	Jet showering	22
97	16	Elliptic flow, v_2 from $p_T = 1$ to 60 GeV/ c	31
98	17	Photon spectrum	32
99	18	Measurements of the nuclear modification factor R_{AA} in central heavy-ion collisions	34
100	19	A comparison between observed $R_{AA}(\Delta\phi, p_T)$ and R_{AA} using v_2	35
101	20	Calculations of the intial energy density in small collision systems at RHIC and the resulting hydrodynamic evolution.	37
102	21	Two-particle correlation results in PbPb, pPb, and pp collisions at the LHC [].	38

109	22	RpA in proton-lead collisions	39
110	23	Distribution of the sum of amplitudes in the V0A hodoscopes (Pb-going), as well as the NBD-Glauber fit (explained in the text). Centrality classes are indicated by vertical lines. The inset shows a zoom-in on the most peripheral events. [1]	41
111			
112			
113			
114	24	Top: Scatter plot of number of participating nucleons versus impact parameter; Bottom: Scatter plot of multiplicity versus the number of participating nucleons from the Glauber fit for V0A. The quantities are calculated with a Glauber Monte Carlo of p-Pb (left) and Pb-Pb (right) collisions. [1]	42
115			
116	25	CERN collider complex	45
117			
118	26	ALICE	48
119			
120	27	ITS	49
121			
122	28	TPC	51
123			
124	29	An example image taken of a GEM foil with false colors.	53
125			
126	30	Illustration of \vec{j}_T . The jet fragmentation transverse momentum, \vec{j}_T , is defined as the transverse momentum component of the track momentum, \vec{p}_{track} , with respect to the jet momentum, \vec{p}_{jet}	58
127			
128	31	Results from unfolding in Toy Monte Carlo	61
129			
130	32	Unfolding with different number of iterations	63
131			
132	33	Effect of changing minimum jet p_T used in unfolding from 5 to 10 GeV	64
133			
134	34	Effect of changing minimum jet p_T used in unfolding from 5 to 10 GeV	64
135			
136	35	j_T Response matrices in single jet p_T bins	66
137			
138	36	Pythia closure test results. Fake tracks include also tracks that do exist in the true dataset, but for one reason or another were not given j_T values. j_T is only calculated for tracks that are associated with jets	67
139			
140	37	j_T signal with random bacgkround subtraction fits in different jet p_T bins	73
141			
142	38	Differences between perpendicular cone and random background subtraction in the resulting RMS values.	74
143			
144	39	j_T signal with random bacgkround subtraction fits in different jet p_T bins	74
145			
146	40	Differences between Bayesian and SVD unfolding in the resulting RMS values	74
147			
148	41	Inclusive j_T with background	77
149			
150	42	j_T background with two different methods	78
151			

148	45	Comparison of inclusive j_T distributions between A and C side for minimum bias and EMCAL triggered data.	79
149			
150	46	j_T signal with background subtracted	80
151	47	Comparison of the effect of background method on j_T signal.	80
152	48	j_T signal fits in different jet p_T bins	81
153	49	RMS values extracted from the fits for the gaussian (narrow) and inverse gamma (wide) components	81
154	50	RMS values extracted from the fits for the gaussian (narrow) and inverse gamma (wide) components	82
155	51	Jet j_T results are compared to results obtained in the dihadron analysis. This is done both in jet p_T and trigger p_T bins by converting between them.	82
156	52	Pythia R parameters j_T	83
157	53	Pythia R parameters RMS	84
158	54	Dihadron j_T results	85
159	55	RMS values of the narrow and wide j_T components in the dihadron correlation analysis. Results from pp collisions at $\sqrt{s} = 7$ TeV (circular symbols) and from p–Pb collisions at $\sqrt{s_{NN}} = 5.02$ TeV (square symbols) are compared to PYTHIA 8 tune 4C simulations at $\sqrt{s} = 7$ TeV (short dashed line) and at $\sqrt{s} = 5.02$ TeV (long dashed line). Different panels correspond to different x_{\parallel} bins with $0.2 < x_{\parallel} < 0.4$ on the left, $0.4 < x_{\parallel} < 0.6$ in the middle, and $0.6 < x_{\parallel} < 1.0$ on the right. The statistical errors are represented by bars and the systematic errors by boxes. [2]	86
160			
161	56	Comparison of results with dihadron j_T results. Dihadron trigger p_T bins are converted to jet p_T bins using observed mean $p_{T,jet}$ values in $p_{T,trigger}$ bins. Dihadron results are for $0.2 < x_{\parallel} < 0.4$	87
162	57	PYTHIA R parameters j_T	88
163	58	Results of calculating j_T with respect to the jet axis or the leading hadron. The assumption is that because the leading hadron is an imperfect estimate of the jet axis, low j_T tracks should on average be shifted to higher j_T	88
164			
165			
166			
167			
168			
169			
170			
171			
172			
173			
174			
175			
176			
177			
178			
179			

180 1 Introduction

181 At sufficiently high energies quarks and gluons are no longer bound to hadrons,
182 but they form a deconfined state known as Quark-Gluon plasma (QGP). The
183 main goal of heavy ion physics is the study of QGP and its properties. One of the
184 experimental observables that is sensitive to the properties of QGP is the azimuthal
185 distribution of particles in the plane perpendicular to the beam direction.

186 When nuclei collide at non-zero impact parameter (non-central collisions), their
187 overlap region is asymmetric. This initial spatial asymmetry is converted via multi-
188 ple collisions into an anisotropic momentum distribution of the produced particles.
189 For low momentum particles ($p_T \lesssim 3$ GeV/c), this anisotropy is understood to
190 result from hydrodynamically driven flow of the QGP [3–7].

191 One way to characterize this anisotropy is with coefficients from a Fourier se-
192 ries parametrization of the azimuthal angle distribution of emitted hadrons. The
193 second order coefficient, v_2 which is also known as elliptic flow, shows clear depen-
194 dence on centrality. The collision geometry is mainly responsible for the elliptic
195 flow. Higher harmonics don't depend that much on centrality. These higher har-
196 monics carry information about the fluctuations in collisions. The event-by-event
197 fluctuations have an increasing importance in measurements and it has been ob-
198 served that measurements of elliptic flow in central collisions and measurements
199 of higher order harmonics are consistent with the assumption that flow in these
200 cases is mainly due to fluctuations [8].

201 At LHC energies $\sqrt{s_{NN}} = 2.76\text{GeV}$ it has been observed that in general there
202 is little difference to flow at RHIC energies. The v_2 coefficient is about 20% greater
203 at LHC than at RHIC, depending on the centrality bin. The particle identified
204 v_2 for kaons and pions follows the same trend. However it was observed that for
205 proton v_2 the quark number scaling does not work [9]. So far there is no agreement
206 of why this scaling breaks down at LHC or why it works so well at RHIC energies.

207 **1.1 Quantum chromodynamics**

208 **1.1.1 Foundation of QCD**

209 There are four known basic interactions in the universe: gravity, electromagnetic,
210 weak and strong interactions. The standard model of particle physics includes
211 three of these excluding the gravitational interaction. The theory of strong inter-
212 actions is known as Quantum Chromodynamics (QCD).

213 The development of QCD began after the introduction of new powerful particle
214 accelerators that were capable of particle physics research in the 1950s. Before this
215 particles were mainly discovered from cosmic rays. Positrons, neutrons and muons
216 were discovered in the 1930s and charged pions were discovered in 1947 []. The
217 neutral pion was discovered in 1950 [10].

218 The Lawrence Berkeley National Laboratory started the Bevalac accelerator in
219 1954, Super Proton Synchrotron (SPS) in CERN began operating in 1959 and the
220 Alternating Gradient Synchrotron at Brookhaven started in 1960. With an energy
221 of 33GeV AGS was the most powerful accelerator of that time. By the beginning
222 of 1960s several new particles had been discovered. These include antiprotons,
223 antineutrons, Δ -particles and the six hyperons (Ξ^0 , Ξ^- , Σ^\pm , Σ^0 and Λ).

224 Facing this number of different particles started the search for symmetries. Al-
225 ready in 1932 Heisenberg [11] had proposed an isospin model to explain similarities
226 between the proton and the neutron. In 1962 Gell-Mann and Ne'eman presented
227 that particles sharing the same quantum numbers (spin, parity) could be organ-
228 ised using the symmetry of SU(3). [12] Heisenberg's Isospin model followed the
229 symmetry of SU(2). Using the SU(3) model known baryons and mesons could be
230 presented as octets. This also lead to the discovery of the Ω^- particle since this
231 was missing from the SU(3) decoupler that included heavier baryons.

232 The most simple representation of SU(3) was a triplet. Inside this triplet
233 particles would have electric charges $2/3$ or $-1/3$. These had not been however
234 detected. In 1964 Gell-Mann [13] and Zweig proposed that baryons and mesons
235 would bound states of these three hypothetical triplet particles that Gell-Mann
236 called quarks. Now we know that these are the u , d and s quarks. This original
237 quark model was violating the Pauli exclusion principle. For example the Ω^-
238 particle is comprised of three s quarks which would have exactly the same quantum
239 states.

240 The first one to present the idea of colour was Greenberg already in 1964 [14].
241 In 1971 Gell-Mann and Frtizsch presented their model, which solved the antisym-
242 metry problem. They added a colour quantum number to quarks, which separated
243 quarks of the same species. In the new colour model the baryonic wave function
244 became

$$(qqq) \rightarrow (q_r q_g q_b - q_g q_r q_b + q_b q_r q_g - q_r q_b q_g + q_g q_b q_r - q_b q_g q_r), \quad (1)$$

245 The colour model was also supported by experimental evidence. The decay
 246 rate of a neutral pion with the addition of colours is

$$\Lambda(\pi^0 \rightarrow \gamma\gamma) = \frac{\alpha^2}{2\pi} \frac{N_c^2}{3^2} \frac{m_\pi^3}{f_\pi^2}. \quad (2)$$

247 For $N_c = 3$ this gives 7.75eV and the measured value is (7.86 ± 0.54) eV [15].

248 Another observable that combines the colour information also to the number
 249 of quark flavours is The Drell-Ratio R [16]

$$R = \frac{\sigma(e^+ + e^- \rightarrow \text{hadrons})}{\sigma(e^+ + e^- \rightarrow \mu^+ + \mu^-)} = N_c \sum_f Q_f^2. \quad (3)$$

250 This ratio has the numerical value 2 when including the three light quarks u , d
 251 and s . When the collision energy reaches the threshold of heavy quark (c and
 252 b) production processes this increases to $^{10}/3$ (for $f = u, d, s, c$) and $^{11}/3$ (for $f =$
 253 u, d, s, c, b). The threshold of $t\bar{t}$ production, $\sqrt{s} \approx 350$ GeV has not been reached
 254 so far by any e^+e^- colliders.

255 The colour model explained why no free quarks had been observed. Only colour
 256 neutral states are possible. The simplest ways of producing a colour neutral object
 257 are the combination of three quarks, and the combination of a quark-antiquark
 258 pair. These are known as baryons and mesons.

259 After the addition of colour the main ingredients of QCD had been established.
 260 The final quantum field theory of Quantum Chromodynamics formed quickly be-
 261 tween 1972 and 1974. Main part of this was the work Gross, Wilczek, Politzer
 262 and George did for non-abelian gauge field theories [17–21]. Gross, Wilczek and
 263 Politzer received the Nobel Prize in Physics for their work. The role of gluons was
 264 as a colour octet was presented by Fritzsch, Gell-Mann and Leutwyler in 1973 [22].
 265 The theory had now 8 massless gluons to mediate the strong interaction.

266 However, these gluons had not been discovered. Indirect evidence of the ex-
 267 istence had been seen as it was observed that only about half of the momentum
 268 of protons was transported by the quarks [23]. Direct evidence should be seen in
 269 electron-electron collisions as a third, gluonic, jet in addition to two quark jets.
 270 Three jet events were first seen in 1979 at the PETRA accelerator at DESY [24–26].

271 1.1.2 Asymptotic Freedom

272 In Quantum Electrodynamics (QED) The electric charge is screened. In the
 273 vicinity of a charge, the vacuum becomes polarized. Virtual charged particle-
 274 antiparticle pairs around the charge are arranged so that opposing charges face

each other. Since the pairs also include an equal amount opposite charge compared to the original charge the average charge seen by an observer at a distance is smaller. When the distance to the charge increases the effective charge decreases until the coupling constant of QED reaches the fine-structure constant $\alpha = \frac{1}{137}$.

Contrary to QED QCD is a non-abelian theory. In other words the generators of the symmetry group of QCD, SU(3), do not commute. This has the practical consequence that gluons interact also with other gluons, whereas in QED the neutral carrier particles, photons, only interact with charged particles. There is screening also in QCD because of the colour charges, but in addition to that there is antiscreening because of the gluon interactions. In QCD the antiscreening effect is stronger than screening. For larger distances to the colour charge the coupling constant is larger. This explains why no free colour charges can be observed. When the distance between charges increases the interaction strengthens until it is strong enough to produce a new quark-antiquark pair.

On the other hand, at very small distances the coupling constant approaches 0. This is called asymptotic freedom. For large energies and small distances the coupling constant is negligible. In 1975 Collins [27] predicted a state where individual quarks and gluons are no longer confined into bound hadronic states. Instead they form a bulk QCD matter that Edward Shuryak called Quark-Gluon plasma in his 1980 review of QCD and the theory of superdense matter [28]. QGP can be seen as a separate state of matter. A schematic view of a phase diagram for QCD matter is shown in Fig. 1.

In the early universe at the age of 10^{-6} s after the Big Bang the conditions preferred the existence of QGP instead of hadronic matter. Nowadays bulk QCD matter, its properties and its phase transitions between hadronic matter and the quark-gluon plasma (QGP) can be explored in the laboratory, through collisions of heavy atomic nuclei at ultra-relativistic energies. The study of QCD matter at high temperature is of fundamental and broad interest. The phase transition in QCD is the only phase transition in a quantum field theory that can be probed by any present or foreseeable technology.

One important property of the QGP is the shear viscosity to entropy ratio, η/s . It is believed that this ratio has an universal minimum value of $1/4\pi \approx 0.8$, which holds for all substances. This limit would be reached in the strong coupling limit of certain gauge theories [30]. The temperature dependance of the ratio is shown in Fig. 2. The minimum value of η/s is found in the vicinity of the critical temperature, T_c [31]. Finding the η/s values in QGP matter would therefore also provide a way of determining the critical point of QCD matter.

The η/s value for the matter created in Au-Au collisions at RHIC ($\sqrt{s_{NN}}$) has been estimated to be 0.09 ± 0.015 [31], which is very close to the lowest value for a wide class of thermal quantum field theories [30] for all relativistic quantum field

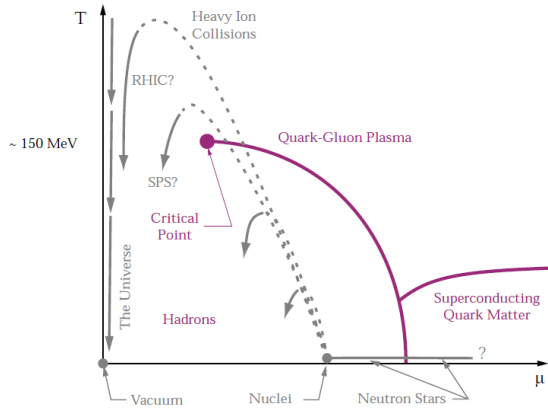


Figure 1: A schematic outline for the phase diagram of QCD matter at ultra-high density and temperature. The quark chemical potential μ that is on the x-axis represents the imbalance between quarks and antiquarks. At zero temperature this corresponds to the number of quarks but at higher temperatures there are also additional pairs of quarks and antiquarks. Along the horizontal axis the temperature is zero, and the density is zero up to the onset transition where it jumps to nuclear density, and then rises with increasing μ . Neutron stars are in this region of the phase diagram, although it is not known whether their cores are dense enough to reach the quark matter phase. Along the vertical axis the temperature rises, taking us through the crossover from a hadronic gas to the quark-gluon plasma. This is the regime explored by high-energy heavy-ion colliders. [29]

³¹⁵ theories at finite temperature and zero chemical potential. This suggests that the
³¹⁶ the matter created goes through a phase where it is close to the critical point of
³¹⁷ QCD.

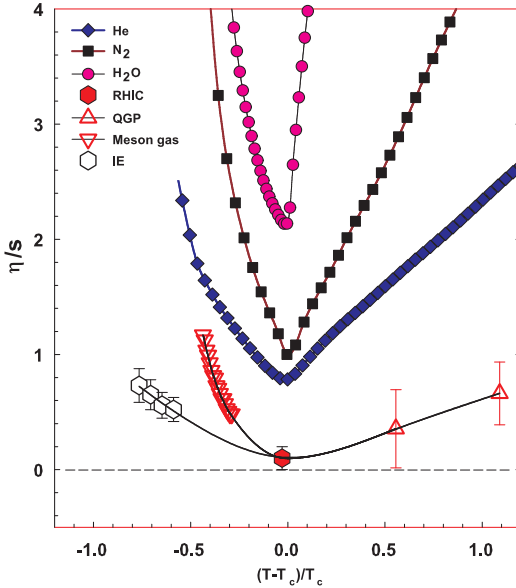


Figure 2: η/s as a function of $(T - T_c)/T_c$ for several substances as indicated. The calculated values for the meson-gas have an associated error of $\sim 50\%$. The lattice QCD value $T_c = 170$ MeV is assumed for nuclear matter. The lines are drawn to guide the eye. [31]

318 1.2 Heavy ion physics

319 The Quark Gluon Plasma (QGP) is experimentally accessible by colliding heavy
320 ions at high energies. Nowadays research of Heavy-Collisions is mainly performed
321 at two particle colliders; the The Relativistic Heavy Ion Collider (RHIC) at BNL
322 in New York, USA and he Large Hadron Collider (LHC) at CERN in Switzer-
323 land. Energy densities at these colliders should be enough to produce QGP and
324 convincing evidence of the creation has been seen at both colliders.

325 The development of heavy ion physics is strongly connected to the development
326 of particle colliders. Experimental study of relativistic heavy ion collisions has been
327 carried out for three decades, beginning with the Bevalac at Lawrence Berkeley
328 National Laboratory (LBNL) [32], and continuing with the AGS at Brookhaven
329 National Laboratory (BNL) [33], CERN SPS [34], RHIC at BNL and LHC at
330 CERN. The first colliders could not produce enough energy to create QGP matter
331 so they could only probe the hadronic state.

332 The collective motion of matter in a heavy-ion collision has been modeled using
333 several models e.g. the Blast wave Model [35] has been used successfully. Another
334 model growing in popularity is the hydrodynamical approach which is further
335 discussed in section 1.3.3.

336 1.2.1 History

337 The first heavy-ion collisions were done at the Bevalac experiment at the Lawrence
338 Berkeley National Laboratory [32] and at the Joint Institute for Nuclear Research
339 in Dubna [36] at energies up to 1GeV per nucleon. In 1986 the Super Proton
340 Synchrotron (SPS) at CERN started to look for QGP signatures in O+Pb col-
341 lisions. The center-of-mass energy per colliding nucleon pair ($\sqrt{s_{NN}}$) was 19.4
342 GeV [34]. These experiments did not find any decisive evidence of the existence
343 of QGP. In 1994 a heavier lead (Pb) beam was introduced for new experiments
344 at $\sqrt{s_{NN}} \approx 17$ GeV. At the same time the Alternating Gradient Synchrotron
345 (AGS) at BNL, Brookhaven collided ions up to ^{32}S with a fixed target at energies
346 up to 28GeV [33]. Although the discovery of a new state of matter was reported
347 at CERN, these experiments provided no conclusive evidence of QGP. Now SPS
348 is used with 400 GeV proton beams for fixed-target experiments, such as the SPS
349 Heavy Ion and Neutrino Experiment (SHINE) [37], which tries to search for the
350 critical point of strongly interacting matter.

351 The Relativistic Heavy Ion Collider (RHIC) at BNL in New York, USA started
352 its operation in 2000. The top center-of-mass energy per nucleon pair at RHIC, 200
353 GeV, was reached in the following years. The results from the experiments at RHIC
354 have provided a lot of convincing evidences that QGP was created [3,4,38,39]. The
355 newest addition to the group of accelerators capable of heavy-ion physics is the

³⁵⁶ Large Hadron Collider (LHC) at CERN, Switzerland. LHC started operating in
³⁵⁷ November 2009 with proton-proton collisions. First Pb-Pb heavy ion runs started
³⁵⁸ in November 2010 with $\sqrt{s_{NN}} = 2.76$ TeV, over ten times higher than at RHIC.
³⁵⁹ Among the six experiments at LHC, the Large Ion Collider Experiment (ALICE)
³⁶⁰ is dedicated to heavy ion physics. Also CMS and ATLAS have active heavy ion
³⁶¹ programs.

362 **1.3 Features of Heavy-Ion Collisions**

363 **1.3.1 Collision Geometry**

364 In contrast to protons atomic nuclei are objects with considerable transverse size.
365 The properties of a heavy-ion collision depend strongly on the impact parameter
366 b which is the vector connecting the centers of the two colliding nuclei at their
367 closest approach. One illustration of a heavy-ion collision is shown in Fig. 3.

368 Impact parameter defines the reaction plane which is the plane spanned by b
369 and the beam direction. Ψ_{RP} gives the angle between the reaction plane and some
370 reference frame angle. Experimentally the reference frame is fixed by the detector
371 setup. Reaction plane angle cannot be directly measured in high energy nuclear
 collisions, but it can be estimated with the event plane method [40].

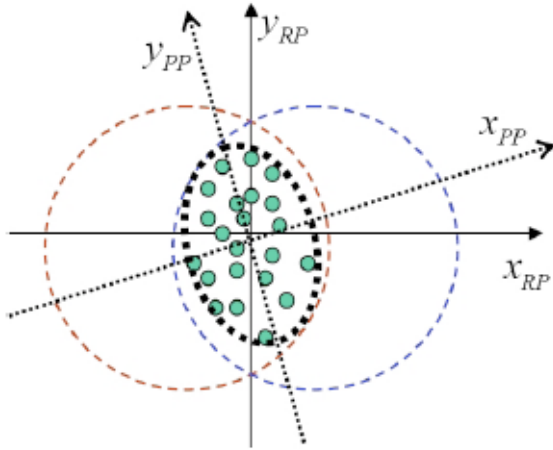


Figure 3: The definitions of the Reaction Plane and Participant Plane coordinate systems [41]. The dashed circles represent the two colliding nuclei and the green dots are partons that take part in the collision. x_{PP} and x_{RP} are the participant and reaction planes. The angle between x_{RP} and x_{PP} is given by Eq. (4). y_{PP} and y_{RP} are lines perpendicular to the participant and reaction planes.

372
373 Participant zone is the area containing the participants. The distribution of
374 nucleons in the nucleus exhibits time-dependent fluctuations. Because the nucleon
375 distribution at the time of the collision defines the participant zone, the axis of
376 the participant zone fluctuates and can deviate from the reaction plane. The angle
377 between the participant plane and the reaction plane is defined by [42]

$$\psi_{PP} = \arctan \frac{-2\sigma_{xy}}{\sigma_y^2 - \sigma_x^2 + \sqrt{(\sigma_y^2 - \sigma_x^2)^2 + 4\sigma_{xy}^2}}, \quad (4)$$

378 where the σ -terms are averaged over the energy density.

$$\sigma_y^2 = \langle y^2 \rangle - \langle y \rangle^2, \sigma_x^2 = \langle x^2 \rangle - \langle x \rangle^2, \sigma_{xy} = \langle xy \rangle - \langle x \rangle \langle y \rangle \quad (5)$$

379 The impact parameter is one way to quantize the centrality of a heavy-ion
 380 collision but it is impossible to measure in a collision. It can be estimated from
 381 observed data using theoretical models, but this is always model-dependent and
 382 to compare results from different experiments one needs an universal definition for
 383 centrality. The difference between central and peripheral collisions is illustrated
 384 in Fig. 4. In a central collision the overlap region is larger than in a peripheral
 385 collision. Larger overlap region translates into a larger number of nucleons partici-
 386 pating in the collision, which in turn leads to a larger number of particles produced
 387 in the event.

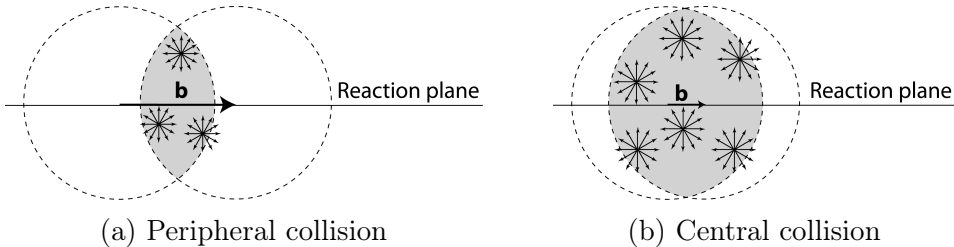


Figure 4: Interaction between partons in central and peripheral collisions. The snowflakes represent elementary parton-parton collisions. When the impact parameter b is large the number of elementary collisions is small. Particle production is small. Smaller impact parameter increases the number of elementary collisions. This increases particle production.

388 Usually centrality is defined by dividing collision events into percentile bins by
 389 the number participants or experimentally by the observed multiplicity. Centrality
 390 bin 0-5% corresponds to the most central collisions with the highest multiplicity
 391 and higher centrality percentages correspond to more peripheral collisions with
 392 lower multiplicities. A multiplicity distribution from ALICE measurements [43]
 393 illustrating the centrality division is shown in Fig. 5. The distribution is fitted
 394 using a phenomenological approach based on a Glauber Monte Carlo [44] plus a
 395 convolution of a model for the particle production and a negative binomial distri-
 396 bution.

397 1.3.2 Nuclear Geometry

398 To model heavy-ion collisions one must first have a description as good as possible
 399 of the colliding objects. Atomic nuclei are complex ensembles of nucleons. The
 400 nuclei used in heavy-ion physics have in the order of 200 nucleons. Mostly used

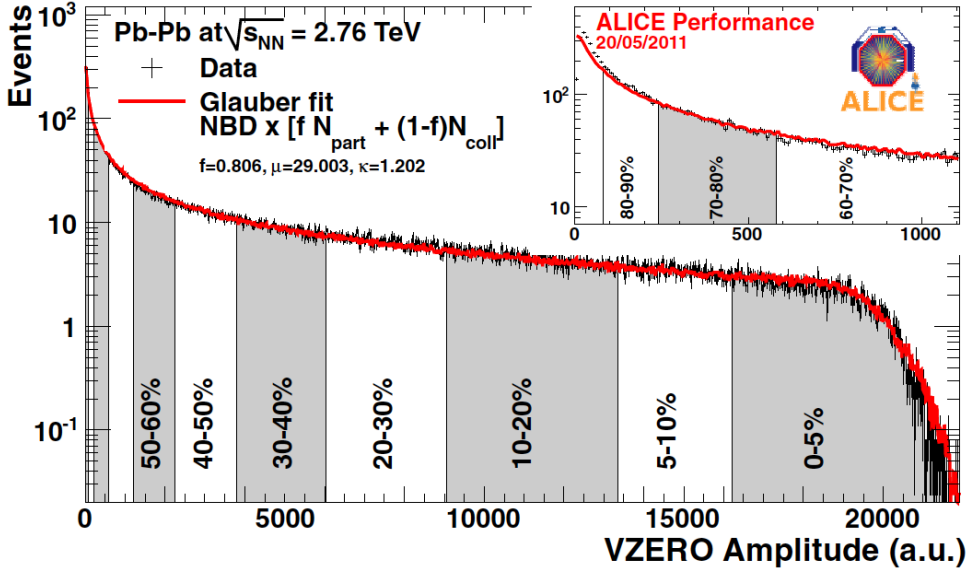


Figure 5: An illustration of the multiplicity distribution in ALICE measurements. The red line shows the fit of the Glauber calculation to the measurement. The data is divided into centrality bins [43]. The size of the bins corresponds to the indicated percentile.

401 nuclei are ^{208}Pb at LHC and ^{197}Au at RHIC. The distribution of these nucleons
 402 within a nucleus is not uniform and is subject to fluctuations in time.

403 Nuclear geometry in heavy-ion collisions is often modelled with the Glauber
 404 Model. The model was originally developed to address the problem of high energy
 405 scattering with composite particles. Glauber presented his first collection of papers
 406 and unpublished work in his 1958 lectures [45]. In the 1970's Glauber's work
 407 started to have utility in describing total cross sections. Maximon and Czyz applied
 408 it to proton-nucleus and nucleus-nucleus collisions in 1969 [46].

409 In 1976 [47] Białas, Bleszyński, and Czyz applied Glauber's approach to
 410 inelastic nuclear collisions. Their approach introduced the basic functions used in
 411 modern language including the thickness function and the nuclear overlap function.
 412 Thickness function is the integral of the nuclear density over a line going through
 413 the nucleus with minimum distance s from its center

$$T_A(s) = \int_{-\infty}^{\infty} dz \rho(\sqrt{s^2 + z^2}). \quad (6)$$

414 This function gives the thickness of the nucleus, i.e. the amount material seen by
 415 a particle passing through it.

⁴¹⁶ Overlap function is an integral of the thickness functions of two colliding nuclei
⁴¹⁷ over the overlap area. This can be seen as the material that takes part in the
⁴¹⁸ collision. It is given as a function of the impact parameter b

$$T_{AB}(b) = \int ds^2 T_A(\bar{s}) T_B(\bar{s} - \bar{b}) \quad (7)$$

⁴¹⁹ The average overlap function, $\langle T_{AA} \rangle$, in an A-A collisions is given by [48]

$$\langle T_{AA} \rangle = \frac{\int T_{AA}(b) db}{\int (1 - e^{-\sigma_{pp}^{inel} T_{AA}(b)}) db}. \quad (8)$$

⁴²⁰ Using $\langle T_{AA} \rangle$ one can calculate the mean number of binary collisions

$$\langle N_{coll} \rangle = \sigma_{pp}^{inel} \langle T_{AA} \rangle, \quad (9)$$

⁴²¹ where the total inelastic cross-section, σ_{pp}^{inel} , gives the probability of two nucleons
⁴²² interacting. The number of binary collisions is related to the hard processes in a
⁴²³ heavy-ion collision. Each binary collision has equal probability for direct produc-
⁴²⁴ tion of high-momentum partons. Thus the number of high momentum particles is
⁴²⁵ proportional to $\langle N_{coll} \rangle$.

⁴²⁶ Soft production on the other hand is related to the number of participants.
⁴²⁷ It is assumed that in the binary interactions participants get excited and further
⁴²⁸ interactions are not affected by previous interactions because the time scales are
⁴²⁹ too short for any reaction to happen in the nucleons. After the interactions ex-
⁴³⁰ cited nucleons are transformed into soft particle production. Production does not
⁴³¹ depend on the number of interactions a nucleon has gone through. The average
⁴³² number of participants, $\langle N_{part} \rangle$ can also be calculated from the Glauber model

$$\begin{aligned} \langle N_{part}^{AB}(b) \rangle &= \int ds^2 T_A(\bar{s}) \left[1 - \left[1 - \sigma_{NN} \frac{T_B(\bar{s} - \bar{b})}{B} \right]^B \right] \\ &+ \int ds^2 T_B(\bar{s}) \left[1 - \left[1 - \sigma_{NN} \frac{T_A(\bar{s} - \bar{b})}{A} \right]^A \right]. \end{aligned} \quad (10)$$

⁴³³ Glauber calculations require some knowledge of the properties of the nuclei.
⁴³⁴ One requirement is the nucleon density distribution, which can be experimen-
⁴³⁵ tally determined by studying the nuclear charge distribution in low-energy elec-
⁴³⁶ tron scattering experiments [44]. The nucleon density is usually parametrized by
⁴³⁷ a Woods-Saxon distribution

$$\rho(r) = \frac{\rho_0}{1 + \exp\left(\frac{r-R}{a}\right)}, \quad (11)$$

438 where ρ_0 is the nucleon density in center of the nucleus, R is the nuclear radius
 439 and a parametrizes the depth of the skin. The density stays relatively constant as
 440 a function of r until around R where it drops to almost 0 within a distance given
 441 by a .

442 Another observable required in the calculations is the total inelastic nucleon-
 443 nucleon cross-section $\sigma_{\text{inel}}^{\text{NN}}$. This can be measured in proton-proton collisions at
 444 different energies.

445 There are two often used approaches to Glauber calculations. The optical ap-
 446 proximation is one way to get simple analytical expressions for the nucleus-nucleus
 447 interaction cross-section, the number of interacting nucleons and the number of
 448 nucleon-nucleon collisions. In the optical Glauber it is assumed that during the
 449 crossing of the nuclei the nucleons move independently and they will be essentially
 450 undeflected.

451 With the increase of computational power at hand the Glauber Monte Carlo
 452 (GMC) approach has emerged as a method to get a more realistic description of
 453 the collisions. In GMC the nucleons are distributed randomly in three-dimensional
 454 coordinate system according to the nuclear density distributions. Also nuclear
 455 parameters, like the radius R can be sampled from a distribution. A heavy-ion
 456 collision is then treated as a series of independent nucleon-nucleon collisions, where
 457 in the simplest model nucleons interact if their distance in the plane orthogonal
 458 to the beam axis, d , satisfies

$$d < \sqrt{\sigma_{\text{inel}}^{\text{NN}}} \quad (12)$$

459 The average number of participants and binary collisions can then be determined
 460 by simulating many nucleus-nucleus collisions. The results of one GMC Pb-Pb
 461 event with impact parameter $b = 9.8\text{fm}$ is shown in Fig. 6

462 1.3.3 Hydrodynamical Modelling

463 The relativistic version of hydrodynamics has been used to model the deconfined
 464 phase of a heavy-ion collision with success. Heavy-ion collisions produce many
 465 hadrons going into all directions. It is expected that tools from statistical physics
 466 would be applicable to this complexity [49]. The power of relativistic hydrodynam-
 467 ics lies in its simplicity and generality. Hydrodynamics only requires that there is
 468 local thermal equilibrium in the system. In order to reach thermal equilibrium the
 469 system must be strongly coupled so that the mean free path is shorter than the
 470 length scales of interest [50].

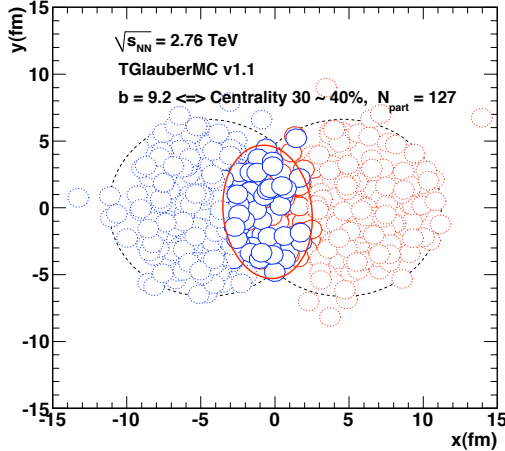


Figure 6: The results of one Glauber Monte Carlo simulation. Big circles with black dotted boundaries represent the two colliding nuclei. The participant zone is highlighted with the solid red line. Small red and blue circles represent nucleons. Circles with thick boundaries are participants i.e. they interact with at least one nucleon from the other nucleus. Small circles with dotted boundaries are spectators which do not take part in the collision.

471 The use of relativistic hydrodynamics in high-energy physics dates back to
 472 Landau [51] and the 1950's, before QCD was discovered. Back then it was used
 473 in proton-proton collisions. Development of hydrodynamics for the use of heavy-
 474 ion physics has been active since the 1980's, including Bjorken's study of boost-
 475 invariant longitudinal expansion and infinite transverse flow [?]. Major steps were
 476 taken later with the inclusion of finite size and and dynamically generated trans-
 477 verse size [?, ?], a part of which was done at the University of Jyväskylä. The role
 478 of hydrodynamics in heavy-ion physics was strengthened when QGP was observed
 479 to behave like a liquid by RHIC [3].

480 The evolution of a heavy-ion event can be divided into four stages. A schematic
 481 representation of the evolution of the collisions is shown in Fig. 7. Stage 1 follows
 482 immediately the collision. This is known as the pre-equilibrium stage. Hydrody-
 483 namic description is not applicable to this regime because thermal equilibrium is
 484 not yet reached. The length of this stage is not known but it is assumed to last
 485 about $1 \text{ fm}/c$ in proper time τ .

486 The second stage is the regime where thermal equilibrium or at least near-
 487 equilibrium is reached. In this stage hydrodynamics should be applicable if the
 488 temperature is above the deconfinement temperature [50]. This lasts about $5 -$
 489 $10 \text{ fm}/c$ until the temperature of the system sinks low enough for hadronization to

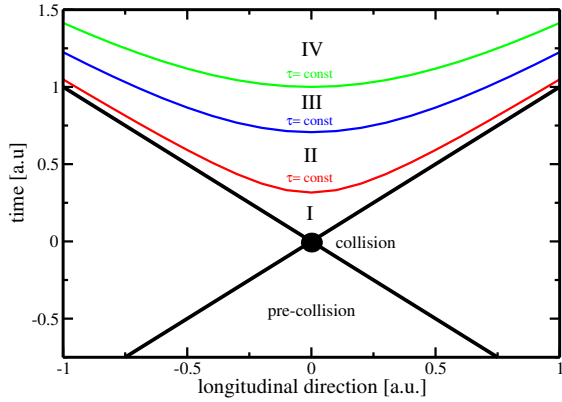


Figure 7: Schematic representation [50] of a heavy-ion collision as the function of time and longitudinal coordinates z . The various stages of the evolution correspond to proper time $\tau = \sqrt{t^2 - z^2}$ which is shown as hyperbolic curves separating the different stages.

490 occur. Now the system loses its deconfined, strongly coupled, state and hydrodynamics can no longer be used. The third stage is the hadron gas stage where the 491 hadrons still interact. This ends when hadron scattering becomes rare and they 492 no longer interact. In the final stage hadrons are free streaming and they fly in 493 straight lines until they reach the detector.

494 The hydrodynamical approach treats the ensemble of particles as a fluid. It 495 uses basic equations from hydrodynamics and thermodynamics but with a few 496 modifications to account for the relativistic energies. The calculation is based 497 on a collection of differential equations connecting the local thermal variables like 498 temperature, pressure etc. to local velocities of the fluid. One also needs equations 499 of state that connect the properties of the matter, e.g. temperature and pressure 500 to density. Given initial conditions and equations of state the calculation gives the 501 time-evolution of the system.

502 At first only ideal hydrodynamics was used. Ideal hydrodynamics does not 503 include viscosity but it is a relatively good approximation and it could predict 504 phenomena like elliptic flow. For more detailed calculations also viscosity must be 505 considered and viscosity itself is an interesting property of QGP.

506 In this thesis I compare my results of identified particle flow to calculations from 507 two hydrodynamical models; VISHNU model by Song *et al.* [52] and calculations 508 by Niemi *et al.* [53].

510 1.4 Flow

511 In a heavy-ion collision the bulk particle production is known as flow. The pro-
 512 duction is mainly isotropic but a lot of studies including my thesis focus on the
 513 small anisotropies. After the formation of the QGP, the matter begins to expand
 514 as it is driven outwards by the strong pressure difference between the center of the
 515 collision zone and the vacuum outside the collision volume. The pressure-driven
 516 expansion is transformed into flow of low-momentum particles in the hadroniza-
 517 tion phase. Since the expansion is mainly isotropic the resulting particle flow is
 518 isotropic with small anisotropic corrections that are of the order of 10% at most.
 519 The isotropic part of flow is referred to as radial flow.

520 The transverse momentum spectra dN/dp_T in heavy-ion collisions is shown

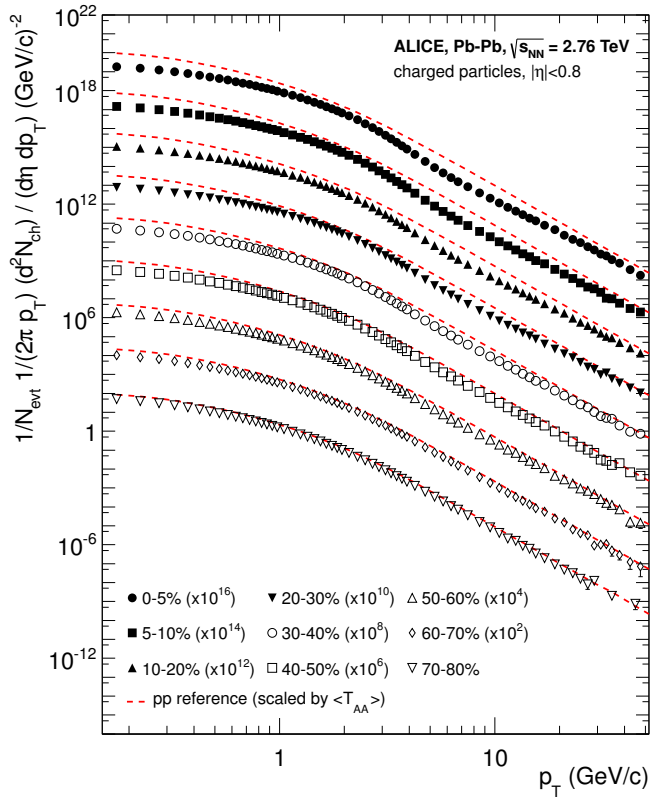


Figure 8: Charged particle spectra measured by ALICE [54] for the 9 centrality classes given in the legend. The distributions are offset by arbitrary factors given in the legend for clarity. The distributions are offset by arbitrary factors given in the legend for clarity. The dashed lines show the proton-proton reference spectra scaled by the nuclear overlap function determined for each centrality class and by the Pb-Pb spectra scaling factors [54].

521 in Fig. 8. The vast majority of produced particles have small p_T . The difference
 522 between the yield of 1 GeV/c and 4 GeV/c particles is already 2-3 orders of mag-
 523 nitude. Any observables that are integrated over p_T are therefore dominated by
 524 the small momentum particles.

525 1.4.1 Anisotropic Flow

526 In a non-central heavy-ion collision the shape of the impact zone is almond-like.
 527 In peripheral collisions the impact parameter is large which means a strongly
 528 asymmetric overlap region. In a central collision the overlap region is almost
 529 symmetric in the transverse plane. In this case the impact parameter is small.
 530 Collisions with different impact parameters are shown in Fig. 4.

531 The pressure gradient is largest in-plane, in the direction of the impact pa-
 532 rameter b , where the distance from high pressure, at the collision center, to low
 533 pressure, outside the overlap zone, is smallest. This leads to stronger collective
 534 flow into in-plane direction, which in turn results in enhanced thermal emission
 535 through a larger effective temperature into this direction, as compared to out-of-
 536 plane [5, 6, 55]. The resulting flow is illustrated in Fig. 9. Flow with two maxima
 537 in the direction of the reaction plane is called elliptic flow. This is the dominant

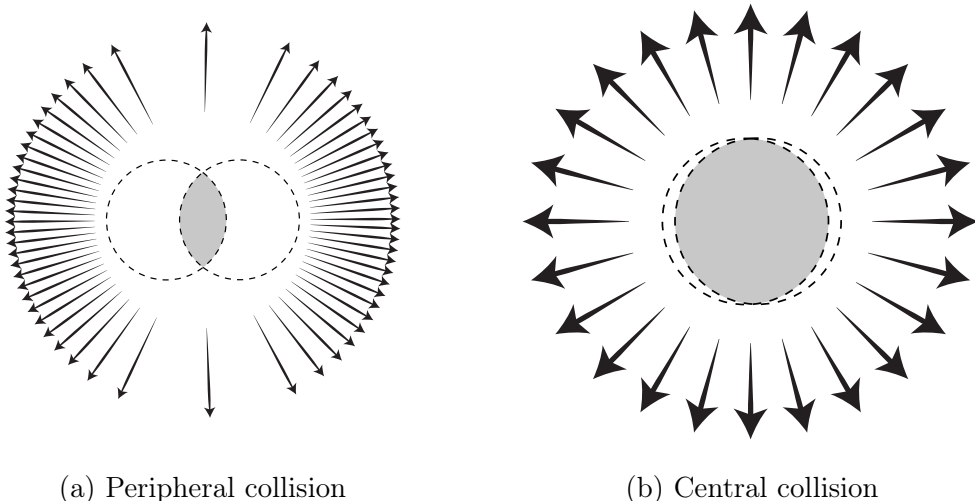


Figure 9: Illustration of flow in momentum space in central and peripheral collisions. The density of the arrows represent the magnitude of flow seen at a large distance from the collision in the corresponding azimuthal direction. In a peripheral collision momentum flow into in-plane direction is strong and flow into out-of-plane direction is weak. In a central collision anisotropy in flow is smaller, but the total yield of particles is larger.

part of anisotropic flow. Also more complex flow patterns can be identified. The most notable of these is the triangular flow, which is mainly due to fluctuations in the initial conditions.

Flow is nowadays usually quantified in the form of a Fourier composition

$$E \frac{d^3N}{dp^3} = \frac{1}{2\pi p_T} \frac{d^2N}{dp_T d\eta} \left(1 + \sum_{n=1}^{\infty} 2v_n(p_T, \eta) \cos(n(\phi - \Psi_n)) \right), \quad (13)$$

where the coefficients v_n give the relative strengths of different anisotropic flow components and the overall normalisation gives the strength of radial flow. Elliptic flow is represented by v_2 and v_3 represents triangular flow. The first coefficient, v_1 , is connected to directed flow. This will however in total be zero because of momentum conservation. It can be nonzero in some rapidity or momentum regions but it must be canceled by other regions.

The first approaches to quantifying the anisotropy of flow did not use the Fourier composition. Instead they approached the problem with a classic event shape analysis using directivity [56] or sphericity [5, 57] to quantify the flow.

The first experimental studies of anisotropy were performed at the AGS [58] in 1993. They noted that the anisotropy of particle production in one region correlates with the reaction plane angle defined in another region.

The first ones to present the Fourier decomposition were Voloshin and Zhang in 1996 [59]. This new approach was useful for detecting different types of anisotropy in flow, since the different Fourier coefficients give different harmonics in flow. They also show the relative magnitude of each harmonic compared to radial flow.

Some parts of the Fourier composition approach were used for Au-Au collisions at $\sqrt{s_{NN}} = 11.4\text{GeV}$ at AGS in 1994 [60]. This analysis still focused on event shapes but they constructed these shapes using Fourier composition from different rapidity windows.

1.4.2 High p_T Phenomena

The measurement of anisotropic flow coefficients can be extended to very high transverse momenta p_T . High p_T measurements of v_2 from CMS [61] are shown in Fig. 16. For high transverse momenta v_2 values are positive and they decrease slowly as a function of p_T . At high transverse momentum the v_2 values don't, however, represent flow.

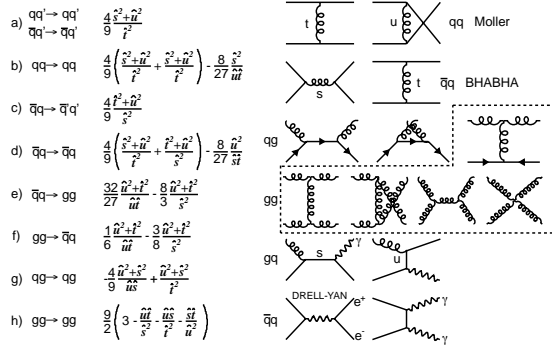


Figure 10: The basic pQCD processes and their quadratic matrix elements

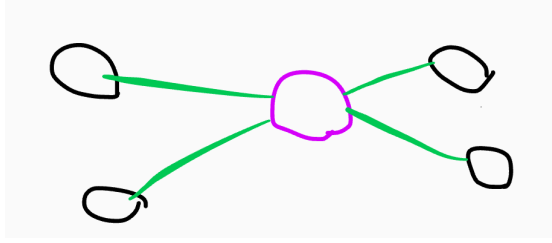


Figure 11: Schematic view of hard scattering process of $p + p \rightarrow 2 \text{jets}$

568 1.5 Hard processes

569 1.5.1 pQCD factorization

The term Hard Scattering is used in connection with the scattering of two point-like constituents (partons) of colliding nucleons, when the momentum transfer Q^2 is large ($Q \gg \Lambda_{\text{QCD}}$). Figure ?? shows the incoming partons, quarks or gluons, as they exchange a space-like virtual gluon and produce two highly virtual outgoing partons. The outgoing partons will eventually fragment into collimated showers of partons, referred to as jets

Jet fragmentation can be factorised into three components; the parton distribution functions f_a , f_b that give the probability of getting a parton with momentum fraction x of the proton, the cross section of the elementary scattering $ab \rightarrow cd$ (Fig. 10) and the fragmentation functions that give the probability of getting hadron h from the parton.

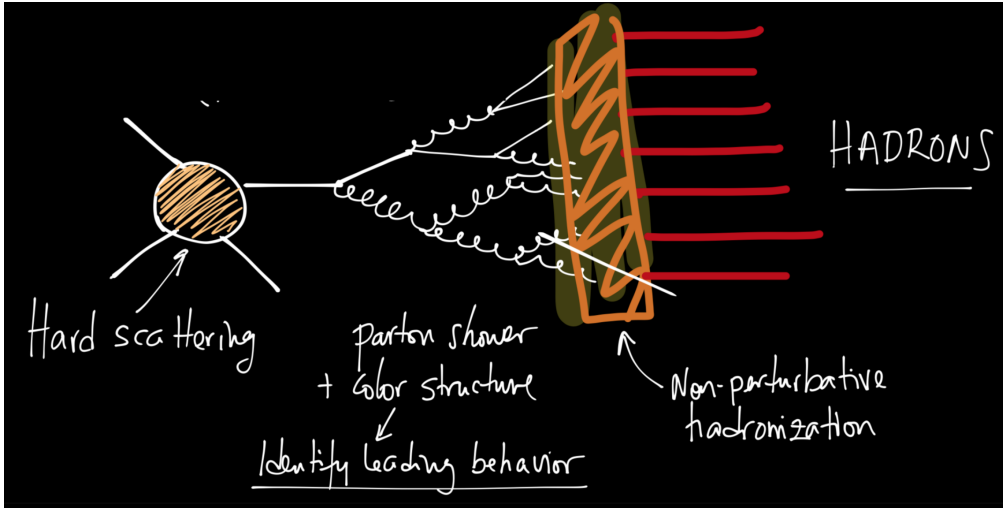


Figure 12: REPLACE FIGURE An illustration of jet showering. The highly virtual parton from the hard scattering will produce a shower of softer partons. When the virtuality is low enough the shower will go through a hadronisation process that produces the hadrons, which will be eventually observed in the detector.

$$\frac{d\sigma_{pp}^h}{dy d^2 p_T} = K \sum_{abcd} \int dx_a dx_b f_a(x_a, Q^2) f_b(x_b, Q^2) \frac{d\sigma}{dt} (ab \rightarrow cd) \frac{D_{h/c}^0}{\pi z_c}$$

$$x_a = \frac{|p_a|}{|p_{proton}|}$$

581 Parton Distribution Function

582 Parton Distribution Functions (PDFs) are essential to calculate the scattering cross
583 section. They are extracted from comprehensive global analysis of experimental
584 results from a variety of fixed-target and collider experiments. PDFs $f_a(x)$ give the
585 differential probability for parton a to carry momentum fraction x of the proton
586 momentum.

587 PDFs cannot be calculated from first principles. In practice the PDFs are
588 measured in Deeply Inelastic Scattering (DIS) experiments and are extrapolated
589 to the relevant momentum scales at LHC using the Dokshitzer-Gribov-Lipatov-
590 Altarelli-Parisi (DGLAP) evolution scheme [?] 14.

$$\mu_F^2 \frac{\partial f_i(x, \mu_F^2)}{\partial \mu_F^2} = \sum_j \frac{\alpha_s(\mu_F)}{2\pi i} \int_x^1 \frac{dz}{z} P_{ij}(z) f_j\left(\frac{x}{z}, \mu_F^2\right), \quad (14)$$

591 where μ_F is a factorization scale. The splitting functions P_{ij} describe a probability
 592 to radiate parton i from parton j as a function of the momentum fraction z
 593 carried away by the offspring parton.

594 The final component in the factorization, fragmentation functions, describe
 595 the distribution of the fractional momenta of particles radiated from the outgoing
 596 parton. Fragmentation function are given with respect to the momentum fraction
 597 z which is defined as the longitudinal momentum fraction of jet momentum p_{jet}
 598 carried away by the jet fragment p_{part}

$$z = \frac{\bar{p}_{\text{part}} \cdot \bar{p}_{\text{jet}}}{p_{\text{jet}}^2} = \frac{p_{\text{part}}}{p_{\text{jet}}} \Big|_{\bar{p}_{\text{part}} \times \bar{p}_{\text{jet}} = 0} \quad (15)$$

599 Fragmentation function $D(z)$ then gives the average multiplicity m of jet frag-
 600 ments having $z > z_0$ [].

$$m(z_0) = \int_{z_0}^1 D(z) dz \Rightarrow m(0) \equiv \langle m \rangle = \int_0^1 D(z) dz \quad (16)$$

601 Because of momentum conservation the sum of all jet fragments must be equal
 602 to the jet momentum, i.e.

$$\sum p_{i,\text{part}} = p_{\text{jet}} \Rightarrow \sum z_i = 1 \Rightarrow \int_0^1 z D(z) dz = 1 \quad (17)$$

603 A natural consequence is that the average momentum fraction is the inverse of
 604 the average multiplicity

$$\langle z \rangle = \frac{\int_0^1 z D(z)}{\int_0^1 D(z)} = \frac{1}{\langle m \rangle} \quad (18)$$

605 1.5.2 Jet hadronisation

606 When the parton shower reaches a scale close to Λ_{QCD} , the perturbative descrip-
 607 tion is no longer valid. Thus the hadronisation stage must be described in a
 608 non-perturbative manner. One simple scenario that is used in several theory calcu-
 609 lations is the so-called local parton-hadron duality [62]. In the local parton-hadron
 610 duality hypothesis it is assumed that there exists a low virtuality scale Q_0 in which
 611 the hadronisation happens, that is independent of the scale of the primary hard
 612 process. At this scale the partons are transformed into hadrons, assuming that the
 613 flow of momentum and quantum numbers for the hadrons can be directly obtained
 614 from those of partons introducing only small normalising constants.

615 Hadronisation is assumed to be universal, i.e. it shouldn't depend on the
 616 collision energy or system.

617 **Lund string model**

618 One common implementation in MC generators is the Lund string fragmentation
 619 algorithm [63]. The string model is based on the fact that in QCD linear confinement
 620 is expected over large distances [64]. This can be modelled by imagining a
 621 colour flux tube being stretched between the outgoing partons. The left side of
 622 Fig. 14 illustrates this point for a $q\bar{q}$ -pair. The tube is assumed to have a uniform
 623 fixed transverse size of about 1 fm along its length, which leads to a linearly rising
 624 potential $V(r) = \kappa r$, where the string constant κ describes the amount of energy
 625 per unit length. A value of $\kappa \approx 1\text{GeV}/\text{fm} \approx 0.2\text{GeV}^2$ can be obtained from hadron
 626 mass spectroscopy.

627 The evolution of string fragmentation is illustrated schematically on the right
 628 side of Fig. 14. This figure is drawn in a light cone presentation, so the initial
 629 quark and antiquark are going to separate directions at the speed of light, which
 630 assumes them as massless. The string between them, illustrated in the figure by
 631 the red line, stretches until its potential energy becomes high enough that it can
 632 break, forming a new quark-antiquark pair. If the original pair was $q\bar{q}$ and the
 633 new pair $q'\bar{q}'$, now two new pairs $q\bar{q}'$ and $q'\bar{q}$ have formed. As these particles
 634 are also moving away from each other, the strings between them can stretch and
 635 break, creating yet more pairs. The process continues until the invariant mass of
 636 the system connected by the string becomes small enough and a final state meson
 637 is formed.

638 To mathematically model the string one can use a massless relativistic string
 639 with no transverse degrees of freedom. The gluons are represented as energy and
 640 momentum carrying kinks on the string with incoherent sums of one colour charge
 641 and one anticolour charge. When this string breaks, it is classically required that
 642 the created quark and antiquark are produced at a certain distance if they are to
 643 have any mass or transverse momentum. However, taking into account quantum
 644 mechanics, the pair must be created at one point and then tunnel out to the
 645 classically allowed region. Thus the probability to create a new quark-antiquark
 646 pair becomes proportional to the tunnelling probability [63].

$$P_{\text{tunnelling}} \propto \exp\left(\frac{-\pi m_\perp^2}{\kappa}\right) = \exp\left(\frac{-\pi m^2}{\kappa}\right) \left(\frac{-\pi p_\perp^2}{\kappa}\right), \quad (19)$$

647 where the transverse mass m_\perp is defined as $m_\perp^2 = m^2 + p_\perp^2$. The transverse
 648 momentum is now defined to be transverse to the string axis. This formula gives
 649 flavour-independent Gaussian p_\perp -distribution for the created $q\bar{q}$ pairs.

650 As explained above the string fragmentation would only produce mesons in
 651 the final state, but we know that also baryons are created in the process. In the
 652 string fragmentation model baryon production is included by adding a probability
 653 that a diquark-antidiquark pair is created instead of a quark-antiquark pair when

654 a string breaks.

655 The kinematics of each string breaking are determined iteratively. Since there
656 is no natural ordering, the string breaking can be considered in any order and
657 the answer obtained must be the same. One can start from the q leg and work
658 one's way to the \bar{q} leg, or vice versa. This give a left-right symmetry of the
659 string fragmentation. In the Lund model this is taken into account by defining a
660 symmetric fragmentation function

$$f(z) \propto \frac{1}{z} (1-z)^a \exp\left(-\frac{bm_{\perp}^2}{z}\right) \quad (20)$$

661 to break the string into a hadron and a remainder system. In the function z is
662 the fraction of light-cone momentum p^+ given to the hadron in the string breaking,
663 m_{\perp} is the transverse mass of the hadron and a and b are tuneable parameters of
664 the model. For heavy quarks this has to be modified as

$$f(z) \propto \frac{1}{z^{1+bm_Q^2}} (1-z)^a \exp\left(-\frac{bm_{\perp}^2}{z}\right) \quad (21)$$

665 The process can be thought as follows: first start from the q-leg of a $q\bar{q}$ system
666 and choose to consider the breaking to new $q'\bar{q}'$ pair closest to this leg. Now the
667 breaking will produce a hadron $q\bar{q}'$ and a remainder system spanning from $q'\bar{q}$.
668 Then the process is continued until the \bar{q} -leg is reached. A small detail here is
669 that in equation (20) it is assumed that the mass of the remainder system is large.
670 Thus some patching up is needed for the last two hadrons coming from a string.
671 The patching up is done such that the place where it happens looks as closely like
672 any other string break as possible.

673 One additional possibility one must consider is that a string can have such a
674 low mass that it cannot break at all. In this case a single hadron is generated out
675 of the string and if necessary energy and momentum are exchanged with other
676 partons in the event.

677 After all the hadrons are produced, the short-lived ones can still decay before
678 the set of final state particles in the simulation is obtained []

679 Cluster model

680 Instead of a string model HERWIG [] uses a cluster model [65] for hadronisation.
681 The advantage of cluster models is that they require a smaller number of param-
682 eters than string models. The model is based on the preconfinement property of
683 parton showers, i.e. the colour structure of the shower at any evolution scale Q_0 is
684 such that colour singlet combinations of partons can be formed with an asymptot-
685 ically universal invariant mass distribution. The invariant mass does not depend

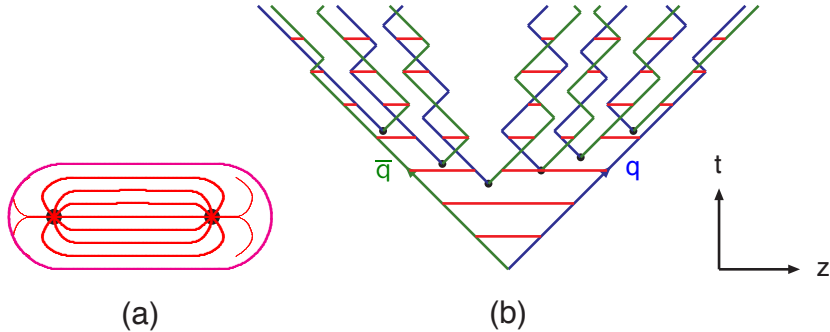


Figure 13: (a) A flux tube spanned between a quark and an antiquark. (b) The motion and breakup of a string system, with the two transverse degrees of freedom suppressed (diagonal lines are (anti)quarks, horizontal ones snapshots of the string field). [64]

on the initial hard process scale Q , but only on Q_0 and the QCD scale Λ_{QCD} , when $Q \gg Q_0$.

The cluster model starts from transforming all gluons non-perturbatively into $q\bar{q}$ pairs, which requires that the gluons get a mass, which must be at least twice the lightest quark mass. After the gluons are transformed into quarks, the adjacent colour lines can be clustered together to colour singlet states with mesonic quantum numbers. The momentum of these clusters is defined to be the sum of the momenta of the clustering partons. According to preconfinement, the mass distribution of these clusters is independent of the details of the hard scattering. Additionally the clusters can be regarded as highly excited hadron resonances and decayed into the final state hadrons.

Some of these initial clusters are too heavy to reasonably describe an excited state of a hadron. These must be split before they are allowed to decay. The cluster C is split if its mass fulfills the condition []

$$M_C^p \geq M_{\max}^p + (m_1 + m_2)^p, \quad (22)$$

where $m_{1,2}$ are the masses of the constituents partons of the cluster and M_{\max} and p are the main parameters of the model. These have to be chosen separately for clusters containing light, charmed and bottom quarks. When a cluster is split, a pair of light quarks is generated from the vacuum and two new clusters are made, both containing one quark from the original cluster and one from the newly generated pair. The splitting is continued until no clusters with masses M_C fulfilling the equation 22 remains.

When are clusters are light enough, they decay into final state hadrons. If the mass of the cluster is high enough for decaying into a baryon-antibaryon pair,

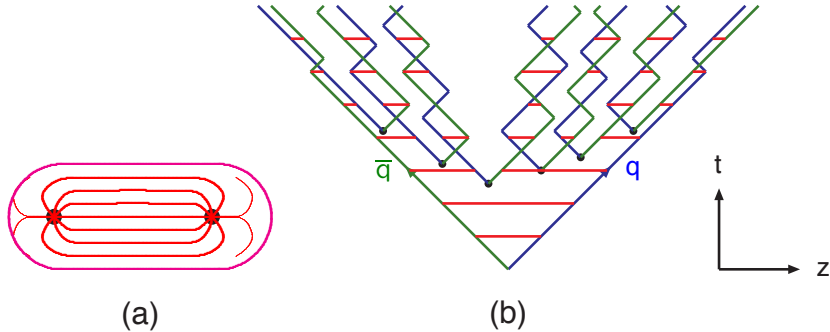


Figure 14: Colour structure of a parton shower to leading order in N_c . [64]

there is a parameter deciding whether the cluster undergoes mesonic or baryonic decay. For a mesonic decay a quark-antiquark pair is created from the vacuum and for the baryonic decay a diquark-antidiquark pair is made. Then the exact decay products are chosen and the cluster decays isotropically in the rest frame of the cluster. If there are partons produced in the perturbative phase involved in the decay, they retain their original direction in the cluster rest frame, up to some Gaussian smearing. If the cluster mass is too low to decay into a pair of mesons, it decays into the lightest possible hadron and some energy and momentum is exchanged with the adjacent clusters. At the end we are left with the final state hadrons, some of which might still decay until the end of the simulation if they are very short-lived. []

1.5.3 Jet energy loss

Figure 15 shows the relevant medium modification phenomena for different regions of the phase space at time t , when a jet propagates through a thermal cloud of temperature T . As in practice jets propagate over a finite path-length L in QCD matter, Fig. 15 can be taken as a representation of the distribution of partonic jet fragments at moment $t \approx L$, when the jet escapes the medium.

The region marked as DGLAP is dominated by the primary vacuum splittings. This region is determined by $\theta > \theta_{\text{vac}}$ with

$$\theta_{\text{vac}} \propto 1/\sqrt{pt}. \quad (23)$$

Medium-induced parton branching fills the log p -log- θ -plane from the bottom up (in p) and from the inside out (in θ). This is because transverse momentum is acquired by Brownian motion in the medium, $k_\perp^2 \propto \hat{q}t$. Then the formation time constraint $t \geq p/k_\perp^2 \approx p/\hat{q}t$ implies that medium-induced quanta can be formed in the region $p \leq k_{\text{form}}$ where

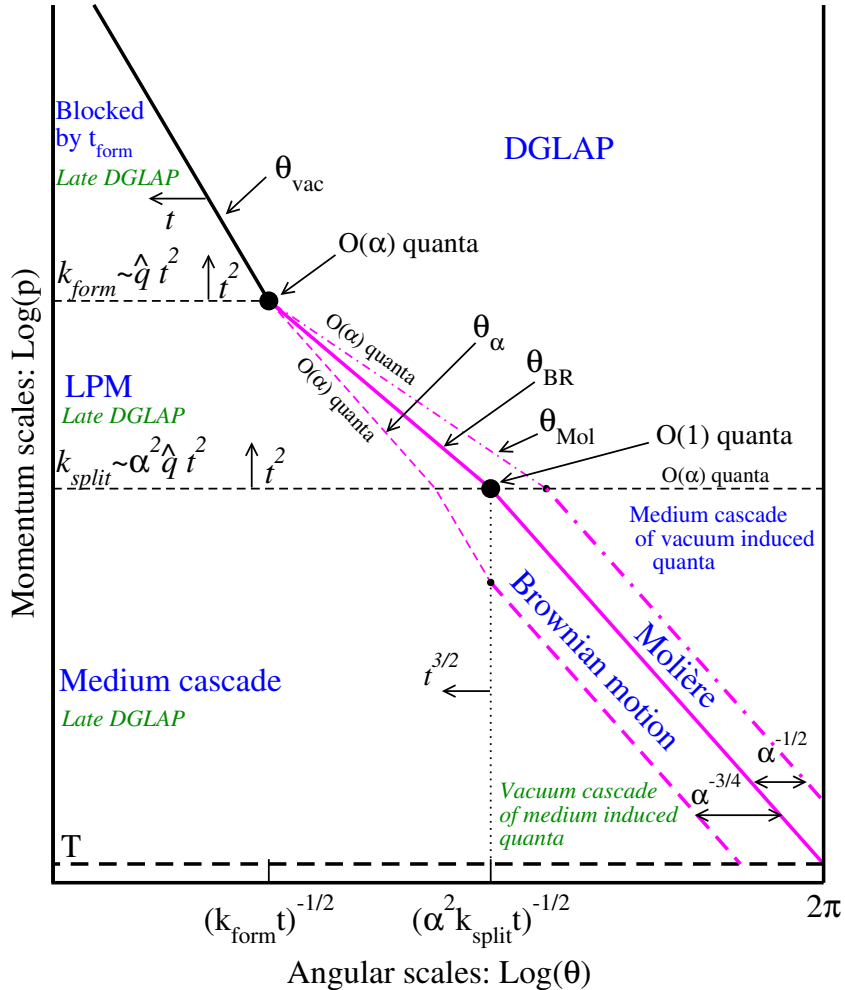


Figure 15: Parametrically accurate picture of how a medium-modified parton cascade fills the phase space. At time t , quanta can be formed up to momentum scale k_{form} and they are formed with $O(1)$ probability per $\log p$ at lower scale k_{split} . Quanta below k_{split} split further and their energy cascades to the thermal scale T in less than an epoch t . Transverse Brownian motion moves quanta up to the angle $\theta_{\text{BR}}(p)$ denoted by the thick purple line. The Molière region at larger θ is dominated by rare large angle scattering. At even larger angle, there are $O(\alpha_s)$ quanta per double logarithmic phase space from DGLAP ‘vacuum’ radiation, and for momenta below k_{split} these cascade within time t to T . After the jet escapes the medium, the jet and the emitted fragments will undergo vacuum radiation. This late time vacuum radiation emitted by the original parton dominates at sufficiently small $\log \theta$ (regions marked “late DGLAP” and bounded by θ_{vac} and θ_α), whereas the late time radiation of the fragments dominates in the region denoted by “Vacuum cascade of the medium induced quanta”. [66].

$$k_{\text{form}}(t) = \hat{q}t^2$$

733 .

734 The probability of finding a splittee with a momentum p with $p < k_{\text{form}}$ is

$$\frac{dP_{\text{find}}(t)}{d \log p} \propto \alpha_s t/t_{\text{form}}(p) \propto \alpha_s \hat{q}^{nicefrac{1}{2}} p^{-1/2} t \quad (24)$$

735 Not all quanta will stay where they were created. Those modes that have time
 736 to lose a significant fraction of their energy will cascade to a significantly lower
 737 scale p . For LPM-type radiation, the splitting that degrades energy the most is
 738 the hardest splitting.

739 The $\log p$ distribution has the same $\frac{1}{\sqrt{p}}$ dependence as in the LPM region

$$\frac{dn}{d \log p} = \frac{1}{p} \frac{d\epsilon}{d \log p} \approx \alpha_s \frac{\sqrt{\hat{q}t}}{\sqrt{p}} \quad (25)$$

740 Also the quanta originating from the DGLAP region will undergo medium
 741 interactions that will make the quanta radiate and split. The distribution of radi-
 742 ation is the same as from any other mode. Above a certain momentum scale k_{split}
 743 the distribution of originating daughters is

$$\frac{dP_{\text{find}}}{d \log p d \log \theta} \approx \alpha_s \frac{t}{t_{\text{split}}(p)}, \quad (26)$$

744 Note that the ratio t/t_{split} is smaller than 1 for nodes above k_{split} and therefore
 745 the number of daughters is smaller than the number of vacuum splitted quanta.
 746 Below k_{split} the cascade is similar to the medium cascade and the number of quanta
 747 become

$$\frac{dn}{d \log p d \log \theta} \approx \alpha_s \frac{t}{t_{\text{split}}(p)}, \text{ for } p < k_{\text{split}}(p) \quad (27)$$

748 The angular distribution is driven by two mechanisms; Multiple soft scatterings
 749 give rise to transverse Brownian motion, which determines the distribution at small
 750 angles. The typical angle reached in the LPM region is

$$\theta_{\text{BR}}(p) \approx \frac{\sqrt{\hat{q}t}}{p}, \text{ for } k_{\text{form}} > p > k_{\text{split}}, \quad (28)$$

751 while in the medium cascade region of the phase space this becomes

$$\theta_{\text{BR}}(p) \approx \left(\frac{T}{p}\right)^{\frac{3}{4}} \quad (29)$$

752 Large angular scales cannot be reached by Brownian motion, but can arise from
753 rare large angle scatterings, described by Molière [].

754 ...

755 "Jet quenching in heavy-ion collisions evolves multi-scale problems [?,66]. The ele-
756 mentary scattering and the subsequent branching process down to non-perturbative
757 scales are dominated by hard scales in the vacuum as well as in the medium. Soft
758 scales, of the order of the temperature of the medium, characterise the interac-
759 tions of soft partons produced in the shower with the QGP. Soft scales also rule
760 hadronisation, which is expected to take place in vacuum for sufficiently energetic
761 probes, even though some modifications can persist from modifications of color
762 flow [?, ?, ?]. Understanding the contributions from the different processes to the
763 jet shower evolution in medium and their scale dependence is crucial to constrain the
764 dynamics of jet energy loss in the expending medium, the role of colour
765 coherence [?], and fundamental medium properties like temperature dependent
766 transport coefficient [?, ?]. "

767 High momentum particles are very rare and they are only produced in the
768 initial collisions. After they are created they escape the medium before a thermal
769 equilibrium is reached. Thus they are not part of the pressure-driven collective
770 expansion. Instead high momentum yield is suppressed because of energy loss in
771 the medium. When propagating through the medium these partons lose energy as
772 they pass through the medium. This is referred to as jet quenching. Jet quenching
773 depends on the path lengths through the medium. Thus anisotropy in this region
774 is mainly dependent on the collision geometry and density of medium.

775 The energy loss of partons in medium is mainly due to QCD bremsstrahlung
776 and to elastic scatterings between the parton and the medium.

777 The radiative energy loss mechanism is given in terms of the transport coef-
778 ficient $\langle \hat{q} \rangle$, which describes the average momentum transfer between the medium
779 and parton [67]. The exact definition of this depends on the theoretical formalism
780 used to describe the energy loss mechanism.

781 Many of the energy loss models exploit the analogy between the QCD interac-
782 tion of parton propagating through the colored medium and the QED energy loss
783 of electron propagating through material. An electron propagating through matter
784 loses its energy by photon Bremsstrahlung radiation. In the simplest case, each
785 individual scattering center results in a single emission of a photon. This is known
786 as the Bethe-Heitler regime [68]. The energy spectrum of radiated photons dN/dE
787 is, in this case, proportional to $1/E$. However, the Bremsstrahlung photon, can be
788 radiated only when the distance between the scattering centers is larger than the
789 formation length. In the limit, when the scattering centers are closer than the
790 formation length, the Bremsstrahlung process is suppressed. This phenomenon

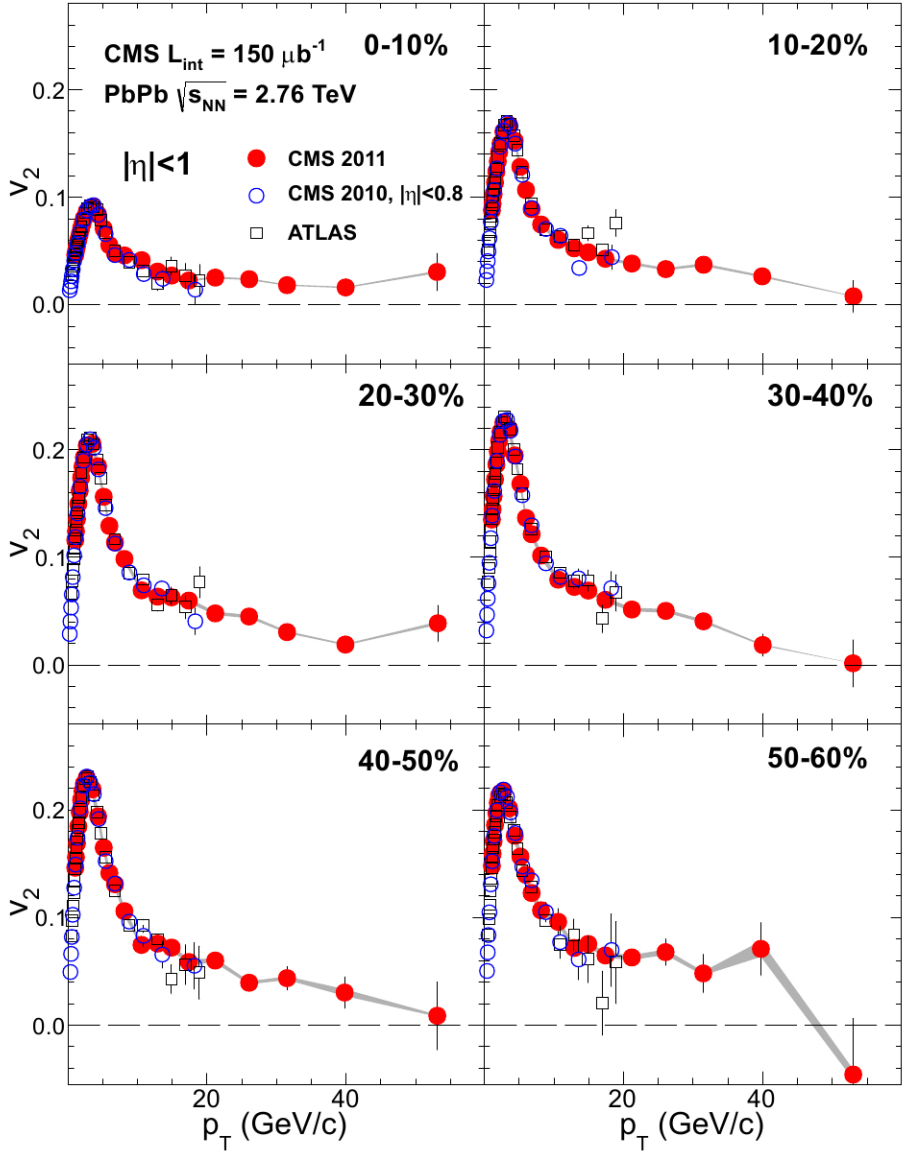


Figure 16: Elliptic flow, v_2 , as a function of the charged particle transverse momentum from 1 to 60 GeV/c with $|\eta| < 1$ for six centrality ranges in Pb-Pb collisions at $\sqrt{s_{NN}} = 2.76 \text{ TeV}$, measured by the CMS experiment. [61].

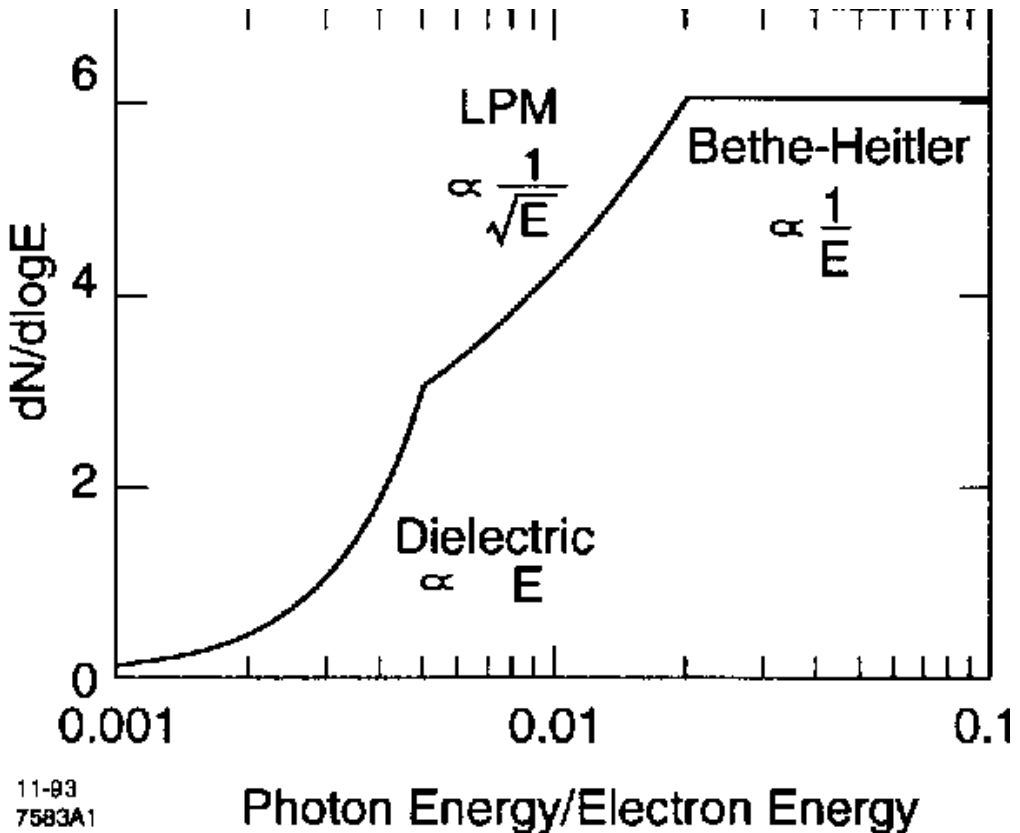


Figure 17: The expected bremsstrahlung spectrum for a electron propagating through material. [71].

is known as the Landau-Pomeranchuk-Migdal (LPM) [69, 70] suppression. The radiated spectrum in this regime is proportional to $1/\sqrt{E}$.

Lower energy photons are further suppressed by the destructive interference leading to the suppression of Bremsstrahlung photons of $E < \gamma\omega_p$, where ω_p is the plasma frequency of the radiator. This is known as Dielectric suppression. The photon energy distribution in this regime is proportional to the energy of the photon. A schematic view of the effect of these three regimes is shown in Fig. 17.

The simplest energy loss process is elastic QCD scattering off the medium partons. In elastic scatterings the recoil energy of the scattered partons are absorbed by the thermal medium, which reduces the energy of the initial parton. The mean energy loss from elastic scatterings can be estimated by

$$\langle \Delta E \rangle_{\text{el}} = \sigma \rho L \langle E \rangle_{\text{1scatt}} \propto L, \quad (30)$$

where σ is the interaction cross section and $\langle E \rangle_{\text{1scatt}}$ is the mean energy transfer of one individual scattering [72]. This assumption holds if the mean energy is

804 independent of the total energy of the parton (E). The transport coefficient of
 805 elastic scattering, $\langle \hat{q}_{\text{el}} \rangle = \langle \Delta E \rangle / L$, is defined as the mean energy loss per unit path
 806 length.

807 Another energy loss mechanism is medium-induced radiation. In QCD this
 808 radiation is mainly due to the elementary splitting processes, $q \rightarrow qg_r$ and $g \rightarrow gg_r$.
 809 Assuming that the parton is moving with the speed of light radiation energy loss
 810 can be estimated by

$$\langle \Delta E \rangle_{\text{rad}} \propto T^3 L^2, \quad (31)$$

811 where L is the length of the medium and T is its temperature [73]. The different
 812 exponents of L in equations 30 and 31 indicate that radiative energy loss is
 813 dominant over elastic energy loss.

814 There are several models that attempt to describe the nature of the energy loss
 815 mechanism. The most used models can be divided into four formalisms.

816 In the Gyulassy-Levai-Vitev (GLV) [74] opacity expansion model the radiative
 817 energy loss is considered on a few scattering centers N_{scatt} . The radiated gluon
 818 is constructed by pQCD calculation as summing up the relevant scattering am-
 819 plitudes in terms of the number of scatterings. Another approach into opacity
 820 expansion is the ASW model by Armesto, Salgado and Wiedermann [75].

821 Thermal effective theory formulation by Arnold, Moore and Yaffe (AMY) [76]
 822 uses dynamical scattering centers. It is based on leading order pQCD hard thermal
 823 loop effective field theory. This model assumes that because of the high temper-
 824 ature of the plasma the strong coupling constant can be treated as small. The
 825 parton propagating through the medium will lose energy from soft scatterings and
 826 hard scatterings.

827 The above models calculate the energy loss while the parton propagates through
 828 the medium, focusing on the pQCD part. The higher twist (HT) approach by Wang
 829 and Guo [77] implements the energy loss mechanism in the energy scale evolution
 830 of the fragmentation functions.

831 The last category is formed by the Monte Carlo methods. The PYTHIA event
 832 generator [78] is widely used in high-energy particle physics. Two Monte Carlo
 833 models based on PYTHIA describing the energy loss mechanism are PYQUEN [79]
 834 and Q-Pythia [80]. Other Monte Carlo models include JEWEL [81] and Ya-
 835 JEM [82].

836 Jet quenching in heavy-ion collisions is usually quantized with the nuclear
 837 modification factor R_{AA} , which is defined as

$$R_{AA}(p_T) = \frac{(1/N_{AA}^{\text{evt}}) dN^{AA}/dp_T}{\langle N_{\text{coll}} \rangle (1/N_{pp}^{\text{evt}}) dN^{pp}/dp_T} \quad (32)$$

838 where dN^{AA}/dp_T and dN^{pp}/dp_T are the yields in heavy-ion and proton-proton

839 collisions, respectively and $\langle N_{coll} \rangle$ is the average number of binary nucleon-nucleon
 840 collisions in one heavy-ion event. The number of binary collisions can be calculated
 841 from the Glauber model as shown in Sec. 1.3.2. From the point of view of direct
 842 production a heavy-ion collision can be estimated relatively well to be only a series
 843 of proton-proton collisions.

844 If the medium has no effect on high p_T particles the nuclear modification factor
 845 should be 1. At RHIC and LHC this has been observed to be as low as 0.2 because
 846 of jet quenching. Measurements of R_{AA} from different sources are shown in Fig. 18

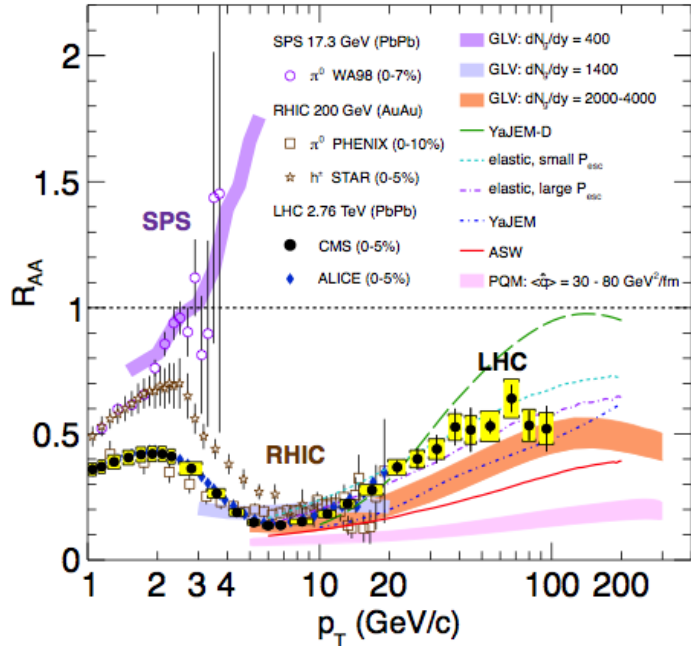


Figure 18: Measurements of the nuclear modification factor R_{AA} in central heavy-ion collisions at three different center-of-mass energies, as a function of p_T , for neutral pions (π^0), charged hadrons (h^\pm), and charged particles [83–87], compared to several theoretical predictions [34, 88–92]. The error bars on the points are the statistical uncertainties, and the yellow boxes around the CMS points are the systematic uncertainties. The bands for several of the theoretical calculations represent their uncertainties [93].

847 The nuclear modification factor can also be used to quantify anisotropy. In
 848 the study of anisotropy R_{AA} in-plane and out-of-plane can be compared. The
 849 distance traveled through medium is largest out-of-plane which leads to stronger
 850 suppression in this direction. The nuclear modification factor as a function of
 851 $\Delta\phi = \phi - \psi_n$ is given by

$$\begin{aligned}
R_{AA}(\Delta\phi, p_T) &= \frac{(1/N_{AA}^{evt}) d^2 N^{AA} / d\Delta\phi dp_T}{\langle N_{coll} \rangle (1/N_{pp}^{evt}) dN^{pp} / dp_T} \approx \frac{dN^{AA} / dp_T (1 + 2 \cdot v_2 \cos(2\Delta\phi))}{\langle N_{coll} \rangle dN^{pp} / dp_T} \\
&= R_{AA}^{incl}(p_T) (1 + 2 \cdot v_2 \cos(2\Delta\phi)). \tag{33}
\end{aligned}$$

852 The yield of proton-proton collisions is independent of the reaction plane and
853 the yield in heavy-ion collisions is modulated by the second harmonics. In Eq. (33)
854 R_{AA} is approximated only up to the second harmonics. From Eq. (33) it follows
855 that

$$\frac{R_{AA}(0, p_T) - R_{AA}(\pi/2, p_T)}{R_{AA}^{incl}(p_T)} \approx \frac{R_{AA}^{incl}(p_T) (1 + 2 \cdot v_2 - (1 - 2 \cdot v_2))}{R_{AA}^{incl}(p_T)} = 4 \cdot v_2 \tag{34}$$

856 The observed $R_{AA}(\Delta\phi, p_T)$ from PHENIX measurements in Au-Au collisions at
857 $\sqrt{s} = 200\text{GeV}$ [94] is compared to R_{AA} using v_2 via Eq. (33) in Fig. 19. They
858 agree very well within the statistical errors for all centrality and p_T bins.

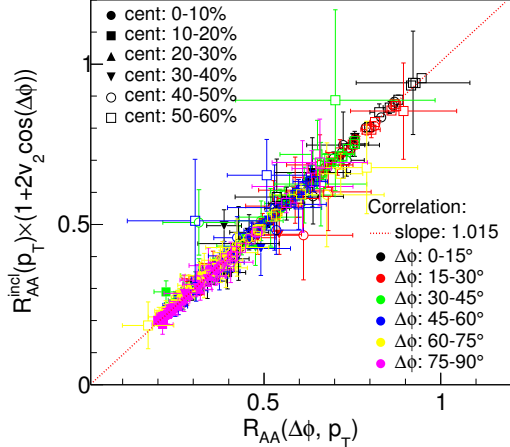


Figure 19: A comparison between observed $R_{AA}(\Delta\phi, p_T)$ and R_{AA} using v_2 from PHENIX measurements of Au-Au collisions at $\sqrt{s} = 200\text{GeV}$. On the X-axis is the measured $R_{AA}(\Delta\phi, p_T)$. On the y-axis is the inclusive R_{AA} multiplied by $1 + 2v_2 \cos(\Delta\phi)$ [94].

858 At high- p_T , the pQCD processes are dominant, hence the v_n (or $R_{AA}(\Delta\phi, p_T)$)
859 characterize the pathlength-dependence of the energy loss process.
860

861 Jet quenching is not the only high p_T phenomenon studied in heavy-ion colli-
862 sions. Another property is jet fragmentation. The high momentum parton created
863 in the initial collision fragments into a number of partons with smaller p_T . Jet
864 fragmentation occurs also in proton-proton collisions in the vacuum, but it can
865 be modified due to the presence of the medium. In order to study the jet frag-
866 mentation function ($D(z)$, where $z = p_T^h/p_T^{part}$) modification due the medium, we
867 use the two-particle correlations. The particle yield can be extracted from the
868 correlation function. The background from the flow processes is correlated and
869 needs to be subtracted to get the particle yield associated only with the jet. The
870 ratio of the jet yields in Au-Au and p-p collision $I_{AA} = Y^{Au+Au}/Y^{p+p}$ character-
871 izes the jet fragmentation modification [95]. I_{AA} probes the interplay between the
872 parton production spectrum, the relative importance of quark-quark, gluon-gluon
873 and quark-gluon final states, and energy loss in the medium.

874 **1.5.4 Monte Carlo Implementations**

875 **1.6 QGP in Small systems**

876 After the existence of QGP in heavy ion collisions has been established, attention
877 has been turned to small systems. Proton-proton (pp) and proton-Lead (pPb)
878 collisions have been studied at LHC and RHIC has studied a host of different
879 collision systems; namely proton-Gold (pAu), deuteron-Gold (dAu) and Helium³-
880 Gold (He³Au) collisions starting in 2000.

881 Already before the era of modern colliders, collective behaviour in proton-
882 proton collisions was considered by names like Heisenberg, Fermi and Bjorken. [96]
883 Eventually there were some experimental searches of QGP in pp and $p\bar{p}$ collisions
884 in E735 at Tevatron [97] and MiniMAX [98]. However no conclusive evidence was
885 found.

886 In the early years of RHIC these small systems were mostly considered as con-
887 trol measurement, for example in constraining nuclear modified parton distribution
888 functions (nPDFs) that determine the initial gluon distributions that determine
889 the first epoch of heavy ion collisions [99, 100].

890 In 2010 ultrahigh-multiplicity pp collisions were studied at CMS. The study
891 found that particles had a weak but clear preference to be emitted along a com-
892 mon transverse ϕ angle across all rapidities [101]. This seemed like behaviour
893 were similar to AA collisions, but it was argued that it could as well come from
894 momentum correlations present in the earliest moments of the collision.

895 In 2012 LHC ran its first pPb data taking period. Around the same time
896 dAu data was reexamined at RHIC. Now it was revealed that most of the flow
897 signatures attributed to hydrodynamic expansion in AA collisions also existed in
898 smaller systems.

899 -Sub nucleonic structure needed to describe intial conditions in pA, pp

900 **1.6.1 Collective phenomena**

901 The most rugged analysis of collective behaviour concerns the two (or more) parti-
 902 cle correlations, often parametrised via the relative azimuthal angle and pseudora-
 903 pidity differences, $\Delta\phi$ and $\Delta\eta$ respectively. Figure 21 shows two-particle correla-
 904 tions measurements in PbPb, pPb and pp collisions at the LHC. In PbPb collisions
 905 long-range correlations dominate over short-range phenomena. This shows in the
 906 two ridges at $\Delta\phi = 0$ and $\Delta\phi = \pi$. At $\Delta\phi \approx \Delta\eta \approx 0$, there is a peak coming from
 907 single jet fragmentation. Since the away-side jet can be spread out in $\Delta\eta$, this
 908 contribution disappears when compared to the flow contribution at the away side
 909 ridge. In pPb, and pp the near side peak is more distinguished and the away-side
 910 jet contribution starts to show. Still, one can see long-range correlations that seem
 911 like flow-like collective behaviour in both systems.

912 In addition to the two particle correlations, correlations have been observed in
 913 the form of v_n coefficients both at LHC and at RHIC. The results have also been
 914 described with hydrodynamical models, although the applicability of said models
 915 is questionable, because of the large Reynolds numbers in small systems. Figure
 916 20 shows results for v_2 in different collisions systems at RHIC as measured by
 917 PHENIX. These different systems provide also different initial geometries. dAu
 918 collisions naturally have an ellipsoidal form, while a He3 collision has a triangular
 919 form and thus produces larger triangular flow, v_3 components.

920 Other observations that produce flow-like results include mass ordered v_2 coeffi-
 921 cients and higher order harmonics coming from fluctuations in the initial geometry.

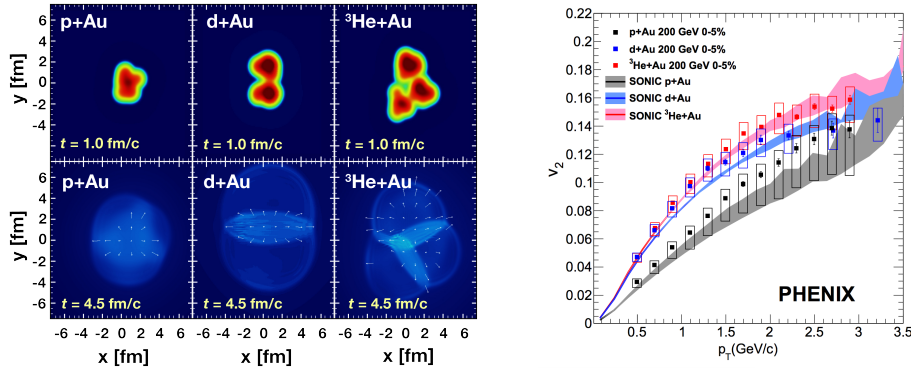


Figure 20: Calculations of the intial energy density in small collision systems at RHIC and the resulting hydrodynamic evolution.

922 Thus all the major collective flow phenomena observed in heavy-ion collisions have
 923 been also identified in small systems.

924 One open question is identifying the point the point, where flow-like correlations end. The question has proved challenging since low multiplicity events are
 925 dominated by non-flow phenomena. This makes observations in low multiplicity
 926 events model/method dependant. Different methods assess non-flow contributions
 927 differently. Thus some methods fail to observe a signal in cases, where others do
 928 and it is unclear whether this is true collective motion or it comes from non-flow
 929 contributions.

931 1.6.2 Absence of jet quenching

932 In A+A collisions, an important confirmation of the standard model comes from
 933 the energy loss of high p_T partons traversing the medium, referred to as jet quench-
 934 ing [102–104]. In 2003 the jet quenching effect was observed to disappear in d+Au
 935 collisions. This was taken as an indication that no QGP was created. Similarly at
 936 LHC no jet modification has been observed in pPb collisions. Fig. 22 shows the
 937 nuclear modification factor R_{pA} in pPb collisions as measured at the LHC.

938 The lack of jet modification seems surprising considering the multitude of flow
 939 observations supporting the existence of QGP in small systems. One possible
 940 explanation is simply the size of medium. In PbPb collision partons traversing
 941 through the medium lose energy to the medium. If the medium is very small there
 942 is limited time for interaction with the medium.

943 Calculations indicate that there should be modification in the most central
 944 pPb collisions, but selecting these in the analysis is complicated. In PbPb colli-
 945 sions most of the particle production comes from the medium and thus the total
 946 multiplicity is a good indicator of centrality. In pPb collisions, however the total
 947 multiplicity is smaller and is more strongly influenced by jet phenomena. Events

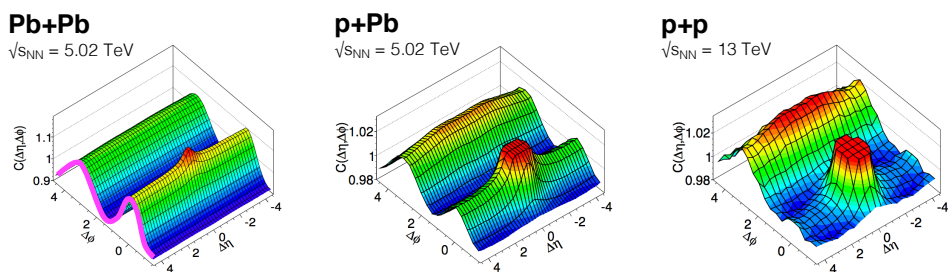


Figure 21: Two-particle correlation results in PbPb, pPb, and pp collisions at the LHC [1].

948 with jets have naturally larger multiplicities and are more likely to be classified as
 949 central events.

950 So far the only observable indicative of jet quenching in pPb collisions is the
 951 high $p_T v_2$. In heavy-ion collisions this is not explained by hydrodynamics. Instead
 952 it is assumed to come from jet quenching with different path lengths through the
 953 medium in different directions. In Fig.22 ATLAS and CMS measurements of v_2 in
 954 pPb and PbPb collisions are shown. The pPb results seem to follow a very similar
 955 pattern. But

Table 1: Summary of observations in small system

Observable	PbPb	pPb	pp
Jet RpA/RAA	Modified	No modification	-
Hadron RpA/RAA	Modified	No modification	-
Heavy flavors			
Jet shape	Broadening	No observations	-
Two-particle correlations	Ridge	Ridge	Ridge
v_2	Observed	Observed	Observed
Mass ordered flow			
Higher ordered harmonics			
High $p_T v_2$	Observed	Maybe	-

956 1.6.3 Centrality determination in small systems

957 In lead-lead collisions the total multiplicity of the event is a good indicator of the
 958 centrality of the collision. In proton-lead collisions the connection of multiplicity

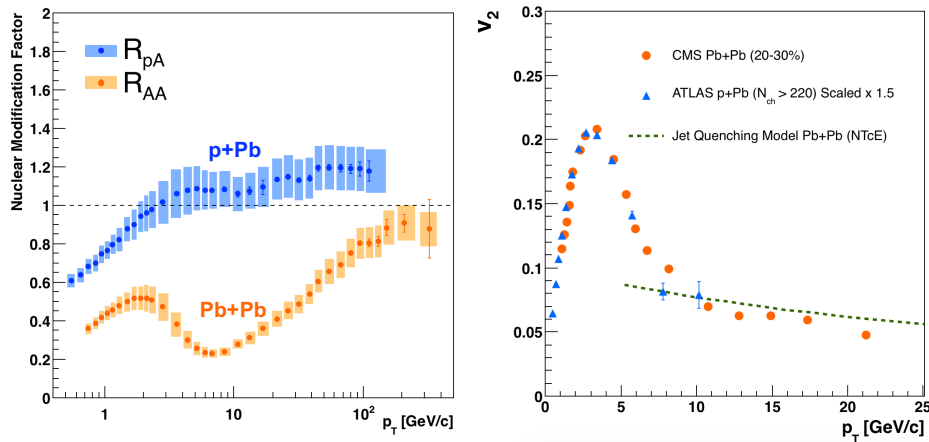


Figure 22: RpA in proton-lead collisions

ity and centrality is less clear. In p–Pb collisions the impact parameter is only loosely correlated to N_{part} or N_{coll} . Hence, although one uses traditionally the term centrality to refer to these measurements, the relevant parameters are N_{part} and N_{coll} [1].

The Glauber model [?] is generally used to calculate geometrical quantities of nuclear collisions (A–A or p–A). In this model, the impact parameter b controls the average number of participating nucleons N_{part} and the corresponding number of collisions N_{coll} . It is expected that variations of the amount of matter overlapping in the collision region will change the number of produced particles, and parameters such as N_{part} and N_{coll} have traditionally been used to describe those changes quantitatively, and to relate them to pp collisions.

The problem in p–Pb collisions, is that fluctuations in multiplicity coming from for example hard scatterings are of the same order as the differences in multiplicity between centrality classes. In Pb–Pb collisions these multiplicity fluctuations have little influence on the centrality determination, the range of N_{part} or N_{coll} is large and $P(M|v)$ converges quickly to a Gaussian with a small width relative to the range of v .

Thus in practice selecting high multiplicity one chooses not only large average N_{part} , but also positive multiplicity fluctuations leading to deviations from the binary scaling of hard processes. These fluctuations are partly related to qualitatively different types of collisions. High multiplicity nucleon-nucleon collisions show a significantly higher particle mean transverse momentum. They can be understood as harder collisions with larger momentum transfer Q^2 or as nucleon-nucleon collisions where multiple parton-parton interactions (MPI) take place. This is illustrated in Fig. 24.

Of particular interest are estimators from kinematic regions that are causally disconnected after the collision. The measurement of a finite correlation between them unambiguously establishes their connection to the common collision geometry. Typically these studies are performed with observables from well separated pseudorapidity (η) intervals, e.g. at zero-degree (spectators, slow-nucleons, deuteron break-up probability) and multiplicity in the rapidity plateau.

One centrality selection that is argued not to induce a bias on the binary scaling of hard processes is provided by the energy measurement with the Zero Degree Calorimeters (ZDC) in ALICE, due to their large η -separation from the central barrel detectors. They detect the "slow" nucleons produced in the interaction by nuclear de-excitation processes or knocked out by wounded nucleons.

Additional kinematic biases exist for events containing high- p_{T} particles, which arise from the fragmentation of partons produced in parton-parton scattering with large momentum transfer. Their contribution to the overall multiplicity increases with increasing parton energy and thus can introduce a trivial correlation between

the centrality estimator and the presence of a high- p_T particle in the event. For very peripheral collisions, the multiplicity range that governs the centrality for the bulk of soft collisions can represent an effective veto on hard processes. For the nuclear modification factor this would lead to $R_{pPb} < 1$.

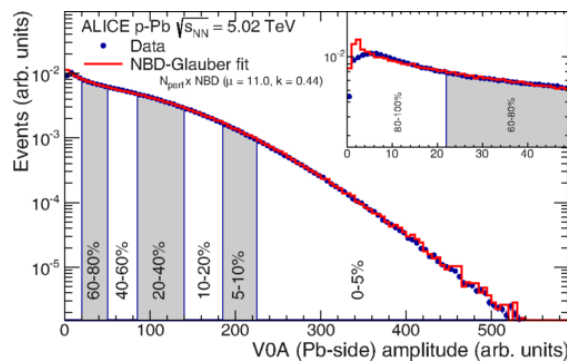


Figure 23: Distribution of the sum of amplitudes in the V0A hodoscopes (Pb-going), as well as the NBD-Glauber fit (explained in the text). Centrality classes are indicated by vertical lines. The inset shows a zoom-in on the most peripheral events. [1]

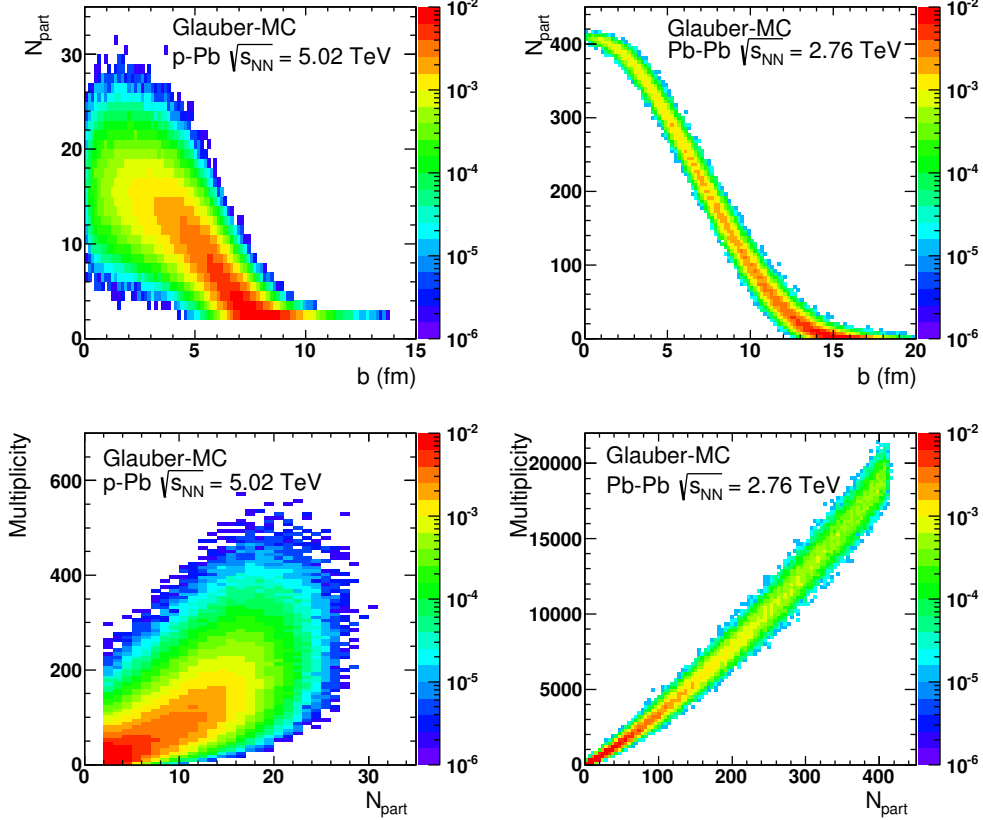


Figure 24: Top: Scatter plot of number of participating nucleons versus impact parameter; Bottom: Scatter plot of multiplicity versus the number of participating nucleons from the Glauber fit for V0A. The quantities are calculated with a Glauber Monte Carlo of p-Pb (left) and Pb-Pb (right) collisions. [1]

1003 2 Experimental setup and data samples

1004 The $\sqrt{s_{\text{NN}}} = 5.02$ TeV p–Pb ($1.3 \cdot 10^8$ events, $\mathcal{L}_{\text{int}} = 620 \text{ nb}^{-1}$) collisions were
1005 recorded in 2013 by the ALICE detector [105]. The details of the performance of
1006 the ALICE detector during LHC Run 1 (2009–2013) are presented in Ref. [106].

1007 The analysis uses charged tracks that are reconstructed with the Inner Track-
1008 ing System (ITS) [107] and the Time Projection Chamber (TPC) [108]. These
1009 detectors are located inside the large solenoidal magnet, that provides a homo-
1010 geneous magnetic field of 0.5 T. Tracks within a pseudorapidity range $|\eta| < 0.9$
1011 over the full azimuth can be reconstructed. The ITS is made up of the innermost
1012 Silicon Pixel Detector (SPD), the Silicon Drift Detector (SDD) and the outermost
1013 Silicon Strip Detector (SSD). Each of these consists of two layers. The TPC is a
1014 cylinder filled with gas. Gas is ionised along the path of charged particles. Liber-
1015 ated electrons drift towards the end plates of the cylinder where they are detected.
1016 Combining the information from the ITS and the TPC provides a resolution rang-
1017 ing from 1 to 10 % for charged particles with momenta from 0.15 to 100 GeV/c.
1018 For tracks without the ITS information, the momentum resolution is comparable
1019 to that of ITS+TPC tracks below transverse momentum $p_T = 10$ GeV/c, but for
1020 higher momenta the resolution reaches 20 % at $p_T = 50$ GeV/c [106, 109].

1021 Neutral particles used in jet reconstruction are reconstructed by the Electro-
1022 magnetic Calorimeter (EMCAL) [110]. The EMCAL covers an area with a range
1023 of $|\eta| < 0.7$ in pseudorapidity and 100 deg in azimuth. EMCAL is complimented
1024 with the Dijet Calorimeter (DCal) [111] and Photon Spectrometer (PHOS) [112]
1025 that are situated opposite of the EMCAL in azimuth. PHOS covers 70 degrees
1026 in azimuth and $|\eta| < 0.12$. The DCal is technologically identical to EMCal. The
1027 DCal coverage spans over 67 degrees in azimuth, but in pseudorapidity the mid
1028 region is occupied by the PHOS. In between PHOS and DCal active volumes, there
1029 is a gap of 10 cm. DCal is fully back-to-back with EMCal.

1030 The combination of charged tracks with $p_T > 0.15$ GeV/c and neutral particles
1031 with $p_T > 0.30$ GeV/c is used to construct jets.

1032 The V0 detector [113] provides the information for event triggering. The V0
1033 detector consists of two scintillator hodoscopes that are located on either side of
1034 the interaction point along the beam direction. It covers the pseudorapidity region
1035 $-3.7 < \eta < -1.7$ (V0C) and $2.8 < \eta < 5.1$ (V0A). For the 2013 p–Pb collisions
1036 events are required to have signals in both V0A and V0C. This condition is used
1037 later offline to reduce the contamination of the data sample from beam-gas events
1038 by using the timing difference of the signal between the two stations [106].

1039 EMCAL is also used to provide the jet trigger used in triggered datasets. EM-
1040 CAL can be used to trigger on single shower deposits or energy deposits integrated
1041 over a larger area. Latter case is used for jet triggers. The EMCAL trigger defini-

tion in the 2013 p–Pb collisions requires an energy deposit of either 10 GeV for the low threshold trigger or 20 GeV for the high threshold trigger in a 32×32 patch size.

In p–Pb collisions the tracks are selected following the hybrid approach [114] which ensures a uniform distribution of tracks as a function of azimuthal angle (φ). The momentum resolutions of the two classes of particles are comparable up to $p_T \approx 10$ GeV/ c , but after that, tracks without ITS requirements have a worse resolution [106, 109].

3 Experimental Details

3.1 CERN

The European Organization for Nuclear Research (CERN) is the largest particle physics laboratory in the world. CERN was founded in 1954. In 2019 CERN consists of 22 member states. Additionally CERN has contacts with a number of associate member states and various individual institutions. Some 12000 visiting scientists from over 600 institutions in over 70 countries come to CERN for their research. CERN itself is located near Geneva at the border of France and Switzerland and itself employs about 2500 people.

The laboratory includes a series of accelerators, which are used to accelerate the particle beams used. A schematic view of the complex as of 2019 is shown in Figure ???. In the framework of this thesis the main component is the Large Hadron Collider (LHC), the largest collider at CERN. LHC will be discussed in the chapter in more detail. Other accelerators in the series are used to inject the particle beam into LHC, but they are also used in itself for various experimental studies.

The second largest accelerator is the super proton synchrotron (SPS). It is final step before the particle beam is injected into LHC. Commissioned in 1976, it was the largest accelerator at CERN until the the Large Electron-Positron Collider (LEP) was finished in 1989. Originally it was used as a proton-antiproton collider and as such provided the data for the UA1 and UA2 experiments, which resulted in the discovery of the W and Z bosons. At the moment there are several fixed target experiments utilising the beam from SPS. These study the structure (COMPASS) and properties (NA61/SHINE) of hadrons, rare decays of kaons (NA62) and radiation processes in strong electromagnetic fields (NA63). Additionally the AWAKE and UA9 experiments are used for accelerator research and development.

-PS

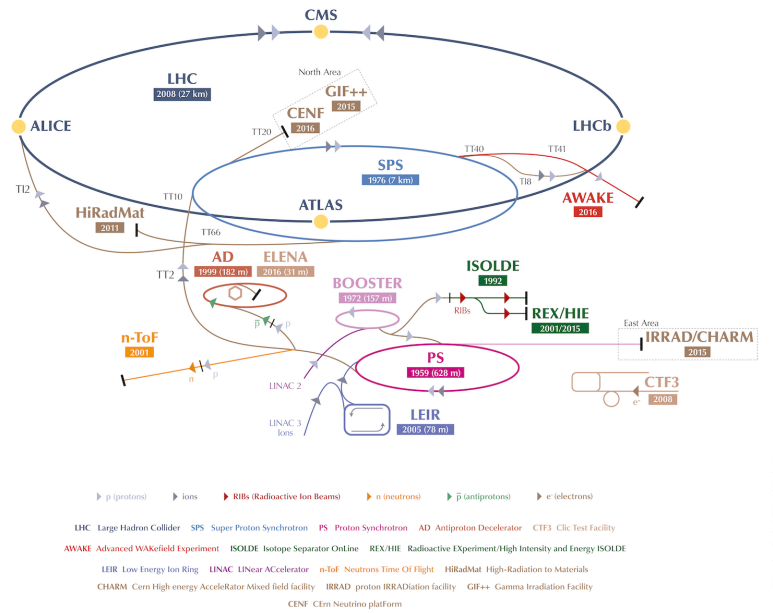


Figure 25: A schematic view of the accelerator complex at CERN. Before particles can be injected into the LHC they require a series of preliminary? acceleterarors. Until 2018 protons start their journey in LINAC2 (Linear Accelerator) and continue through the Booster, Proton Synchrotron (PS) and Super Proton Synchrotron (SPS). Between 2019 and 2020 LINAC2 will be replaced by LINAC4 [115]

1077 3.2 Large Hadron Collider

1078 The Large Hadron Collider (LHC) is the largest accelerator at CERN and the
1079 largest particle collider ever built. The LHC is designed to accelerate protons
1080 up to an energy of 8 TeV and lead ions up to 2.76 TeV per nucleon [?]. The design
1081 luminosity of the LHC is $10^{34} \text{ cm}^{-2} \text{ s}^{-1}$. In 20xx it achieved a record peak luminosity
1082 of xxx. For lead beams the design luminosity is xxx. All this is achieved with a
1083 ring of 26.7 km, that consists of 1232 superconducting dipole magnets that keep
1084 particles in orbit.

1085 The particles are accelerated through the use of radio-frequency (RF) cavities.
1086 The RF are build such that the electromagnetic waves become resonant and build
1087 up inside the cavity. Charges passing through the cavity feel the overall force
1088 and are pushed forward along the accelerator. As they consist of electromagnetic
1089 waves, the field in the RF cavity oscillates. Thus particles must enter the cavity at
1090 the correct phase of oscillation to receive a forward push. When timed correctly,
1091 the particles will feel zero accelerating voltage when they have exactly the correct
1092 energy. Particles with higher energies will be decelerated and particles with lower
1093 energies will be accelerated. This focuses particles in distinct bunches. The RF
1094 oscillation frequency at the LHC is 400.8 MHz. Thus RF "buckets" are separated
1095 by 2.5 ns. However only 10 % are actually filled with particles, so the bunch
1096 spacing in the LHC is 25 ns, at a bunch frequency of 40 MHz.

1097 With 7 TeV proton beams the dipole magnets used to bend the beam must
1098 produce a magnetic field of 8.33 T. This can be only achieved through making
1099 the magnets superconducting, which requires cooling them down with helium to a
1100 temperature of 1.9 K. The 1232 dipole magnets make up roughly 2/3 of the LHC
1101 circumference. The remaining part is made up of RF cavities, various sensors and
1102 higher multipole magnets used to keep the beam focused. The most notable of
1103 these are the 392 quadrupole magnets.

1104 The LHC is divided into octants, where each octant has a distinct function.
1105 Octants 2 and 8 are used to inject beam into the LHC from SPS. The 2 beams
1106 are crossed in octants 1,2,5 and 8. The main experiments are built around these
1107 crossing points. Octants 3 and 7 are used for beam cleansing. This is achieved
1108 through collimators that scatter particles with too high momentum or position
1109 offsets off from the beam. The RF cavities used for acceleration are located in
1110 octant 4 and octant 6 is used for dumping the beam. The beam dump is made
1111 up of two iron septum magnets, one for each beam, that will kick the beam away
1112 from machine components into an absorber when needed.

1113 **3.2.1 LHC experiments**

1114 As of 2018 there are four main experiments at the LHC; ALICE, ATLAS, CMS
1115 and LHCb and three smaller ones LHCf, TOTEM and MoEDAL. ALICE will be
1116 covered in section 3.3.

1117 ATLAS (A Toroidal LHC ApparatuS) and CMS (Compact Muon Solenoid) are
1118 the two largest experiments at the LHC. They are both multipurpose experiments
1119 designed to be sensitive to many different possible new physics signals. The biggest
1120 discovery made by these so far is the discovery of the Standard Model Higgs boson,
1121 which was simultaneously published by the experiments in 2012 [?, ?].

1122 The LHCb (LHC beauty) experiment [?] is made for studying the bottom
1123 (beauty) quark. Main physics goals include measurement of the parameters of CP
1124 violation with decays of hadron containing the bottom quark. One of the most
1125 important results published by LHCb is the first measurement of $B_s^0 \rightarrow \mu^+ \mu^-$
1126 decay, which was found to be in line with the Standard Model.

1127 In addition to the four large experiments there are three smaller experiments
1128 along the LHC ring. LHCf (LHC forward) is located at interaction point 1 with
1129 ATLAS. It aims to simulate cosmic rays by the particles thrown forwards by the
1130 collisions in ATLAS.

1131 TOTEM (TOTal Elastic and diffractive cross section Measurement) is located
1132 near the CMS experiment at point 5. This allows it to measure particles emerging
1133 from CMS with small angles. The main goals is to measure the total, elastic and
1134 inelastic cross-sections in pp collisions [?].

1135 The MoEDAL (Monopole and Exotics Detector At the LHC) experiment is
1136 located at the interaction point 8 together with the LHCb experiment. MoEDAL
1137 tries to measure signatures of hypothetical particles with magnetic charge, mag-
1138 netic monopoles.

1139 **3.3 ALICE**

1140 ALICE (A Large Ion Collider Experiment) [116] is the dedicated heavy ion ex-
1141 periment at the LHC. ALICE was designed to cope with the expected very high
1142 multiplicity environment of heavy ion collisions. The design allows measurement
1143 of a large number of low momentum tracks. The different detector subsystems are
1144 optimised to provide high momentum resolution and excellent particle identifica-
1145 tion capabilities over a broad range of momentum.

1146 A schematic view of the ALICE detector in 2018 is presented in Figure 26.
1147 This section will go through the composition of ALICE as it has been during
1148 run 2 between 2014 and 2018. The detector will go through significant upgrades
1149 during Long Shutdown 2 in 2019-2020. As in all the major high energy physics
1150 experiments the positioning of the detectors follows a layered structure. Closest to

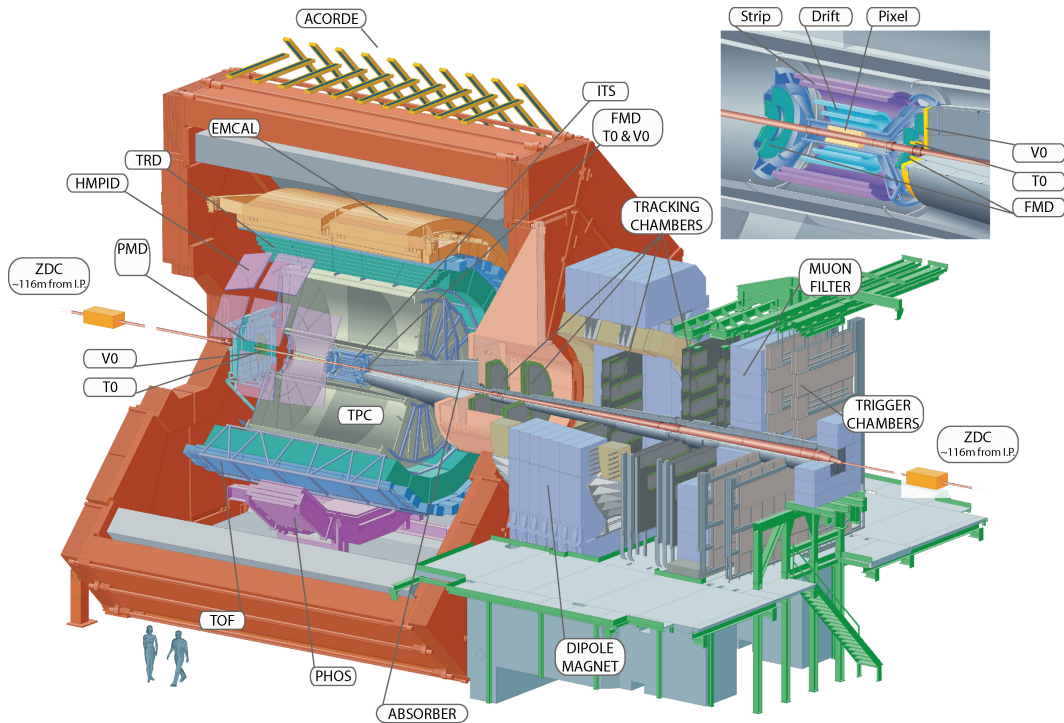


Figure 26: Schematic view of ALICE

the interaction point are the tracking detectors. The main task of these detectors is to locate the position of the primary interaction vertex accurately and to record the tracks of charged particles. To achieve this they need a very good spatial resolution close to the interaction point. Tracking detectors do not significantly alter the tracks of traversing particles. Thus they can be located in the innermost layers.

Calorimeters are designed to stop any particles hitting them and use the absorption to measure the energy of the particles. Thus they must be located behind the tracking detectors. ALICE has two separate calorimeter systems, the electromagnetic calorimeters measure mainly electrons and photons, while the muon detection system measures muons.

3.3.1 Tracking

The main design guideline for the tracking detectors in ALICE was the requirement to have good track separation and high granularity in the high multiplicity environment of heavy ion collisions. Before LHC was built the wildest estimates put the particle density at 8000 charged particles per unit of rapidity [1]. In reality the particle density turned out to be significantly smaller, about 1600 charged

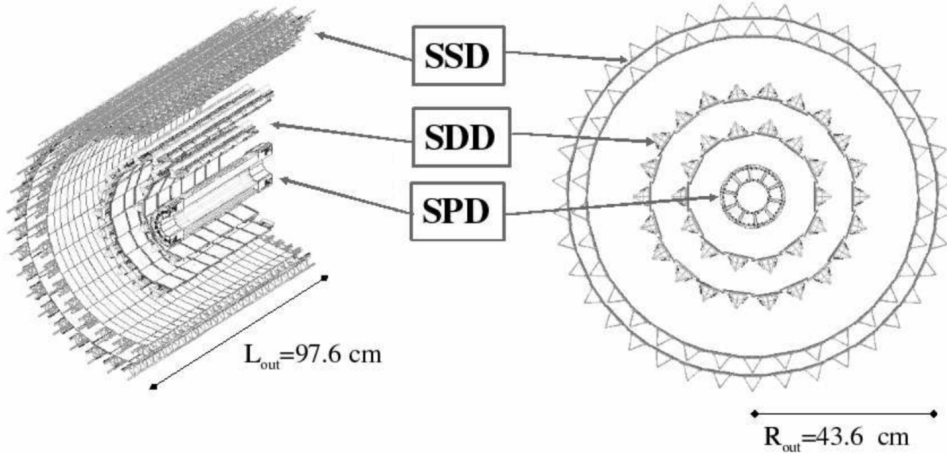


Figure 27: Schematic view of ALICE Inner Tracking System

1168 particles per rapidity unit. []

1169 The main tracking detector in ALICE is the Time Projection Chamber (TPC),
1170 discussed in more detail in section 3.3.2

1171 Between TPC and the beam pipe there is an array of six layers of silicon detec-
1172 tors, called the inner tracking system (ITS) [?]. The main tasks of the ITS are to
1173 locate the primary vertex with a resolution better than $100 \mu m$, to reconstruct the
1174 secondary vertices from decaying particles, to track and identify particles with mo-
1175 menta below 200 MeV and to compliment the momentum and angle measurements
1176 of TPC. During long shutdown 2 in 2019-2020 the entire ITS will be replaced [?].
1177 As of 2018 the two innermost layers are made of the silicon pixel detector (SPD).
1178 As it's the closest detector to the interaction point it requires are very high spatial
1179 resolution. Thus the choice of pixel technology is natural. In heavy ion collisions
1180 the particle density is around 50 particles per cm^2 .

1181 The next two layers are the silicon drift detector (SDD), which is made out of
1182 homogeneous neutron transmutation doped silicon. It is ionized when a charged
1183 particle goes through the material. The generated charge then drifts to the col-
1184 lection anodes, where it is measured. The maximum drift time in SDD is about 5
1185 μs . This design gives very good multitrack capabilities and provides two out of the
1186 four dE/dx samples in the ITS.

1187 The two remaining layers in the ITS are the silicon strip detector (SSD). The
1188 strips work in a similar way as silicon pixels, but by itself one layer only provides
1189 good resolution in one direction. Combining two crossing grids of strips provides 2
1190 dimensional detection. Each charged particle will hit two intervening strips. The
1191 position of the hit can be deduced from the place where the strips cross each other.

1192 **3.3.2 TPC**

1193 Time projection chamber (TPC) is a cylindrical detector filled with $88m^3$ of
1194 Ne – CO₂ (90/10 %) gas mixture. The gas is contained in a field cage that provides
1195 an uniform electric field of $400V/cm$ along the z-axis (along the beam direction).
1196 Charged particles traversing through the TPC volume will ionise the gas along
1197 their path. This liberates electors that drift towards the end plates of the cylin-
1198 der.

1199 The field cage is separated into two detection volumes by the central high
1200 voltage electrode. Both sides have a drift length of 2.5 m and inner/outer diameters
1201 of 1.2/5 m. This means the central electrode must provide a maximum potential
1202 of 100 kV to achieve the design field magnitude. The maximum time required for
1203 electrons to drift through the chamber is about $90 \mu s$.

1204 When electrons reach the end of the main cylinder they enter the readout
1205 chambers. The readout section of both sides consists of 18 outer chambers and
1206 18 inner chambers. Each of them are made of multiwire proportional chambers
1207 with cathode pad readout. This design is used in many TPCs before. During
1208 Long Shutdown 2 in 2019-2020, the multiwire chambers will be replaced by Gas
1209 Electron Multipliers (GEMs, see section 3.3.3).

1210 The relatively slow drift time of $90 \mu s$ is the limiting factor for the luminosity
1211 ALICE can take. The occupancy of the TPC must be kept in a manageable level.

1212 **3.3.3 TPC upgrade**

1213 During long shutdown 2 in 2019-2020 ALICE will go through significant modifica-
1214 tions. The goal is to be able have continuous readout [?] in heavy ion collisions at
1215 an interaction rate of 50 kHz. I have made a personal contribution to the quality
1216 assurance of the new GEM readout of TPC.

1217 ALICE will add a new Forward Interaction trigger (FIT) to replace the V0 and
1218 T0 detectors.

1219 Additionally the current inner tracking system (ITS) will be completely re-
1220 placed. The current layered structure with three different technologies will be
1221 replaced by an all pixel detector with significantly reduced pixel size. Additionally
1222 the first layer will be brought closer to the beam pipe. The new ITS will have
1223 better tracking efficiency and better impact parameter resolution.

1224 The muon detection will be complimented by the Muon Forward Tracker (MFT) [?].
1225 Based on the same technology as the new ITS, MFT will be placed before the
1226 hadron absorber that sits in front of the existing muon spectrometer. MFT should
1227 significantly increase the signal/background ratio in heavy quark measurements.

1228 Many subdetectors will make small improvements to enhance the readout rate.
1229 The central trigger processor will be replaced and ALICE will introduce a new

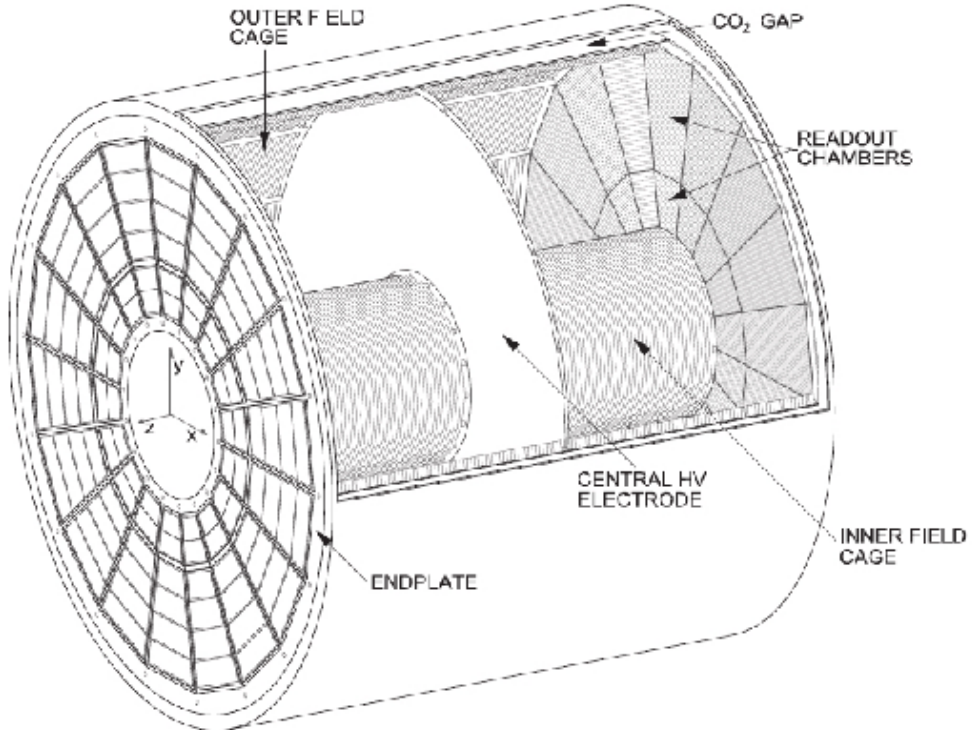


Figure 28: Schematic view of ALICE Time Projection Chamber

1230 framework O^2 that combines both online data acquisition and offline analysis.

1231 The detector restricting the readout the most at the moment is the TPC. The
 1232 current wire chamber based system limits the readout rate to 3.5 kHz. To achieve
 1233 the 50 kHz readout rate goal the wire chambers will be replaced by a Gas Electron
 1234 Multiplier (GEM) based system.

1235 TPC has a total of 36 inner and 36 outer readout chambers. Each of these will
 1236 consist of 4 layers of GEM foils. The inner chambers will only have one foil for
 1237 each layer. The outer chambers are separated into three sections, each with its
 1238 own layer of foils. Each gem foil is made up of a $50\ \mu\text{m}$ thick resistive capton layer,
 1239 coated on both sides by $5\mu\text{m}$ thick layers of copper. Each foils is separated into a
 1240 number (20-24) of distinct active areas. The active areas are pierced quite densely,
 1241 they have 50-100 holes in the area of a single mm^2 . The density of holes changes
 1242 from layer to layer. The two middle layers of foils have a larger (double) pitch
 1243 (smaller hole density) while the top and bottom layers have a smaller (normal)
 1244 pitch (larger hole density).

1245 The holes have a conical shape which they acquire during a two step chemical
 1246 etching process.

1247 The working principle of these foils is based on electrodynamics. **elaborate** There
1248 is a large potential difference (140-400 V) applied to the two sides of the foil, which
1249 results in large field in each hole. This acts both as a lens and an amplifier for
1250 the electrons. The amplification happens inside the holes where the field is the
1251 strongest.

1252 As opposed to wire chambers, which typically have one voltage setting, a GEM-
1253 based detector requires several independent voltage settings: there is a drift voltage
1254 which drives the electrons from the ionisation point to the GEM, an amplification
1255 voltage, and an extraction voltage that brings electrons from the GEM exit to the
1256 readout plane.

1257 The GEMs are designed to minimise ion backflow to allow continuous, ungated
1258 and untriggered readout.

1259 The purpose of the multilayered structure is to reduce the ion backflow []; not
1260 only one layer of GEM foils will be installed, but a 4 layer stack. In the stack there
1261 are 2 standard pitch GEM foils, where the pitch size, i.e. the separation of the
1262 holes inside a foil is around $140 \mu\text{m}$, and 2 large pitch GEM foils, there the hole
1263 spacing is two times larger, $280 \mu\text{m}$. The two outer layers will have standard pitch
1264 and the two middle layers have large pitch. The middle layers with large pitch
1265 serve as extra insulator against the ion backflow. Additionally the setup allows
1266 operating individual GEM foils at lower voltages and still have an increase in the
1267 gain of a few orders of magnitude.

1268 [?]

1269 Quality Assurance of the GEM foils

1270 The GEM foils are produced at CERN, where they will undergo a basic QA (QA-B)
1271 procedure, that includes

- 1272 • Coarse optical inspection to see any major defects, holes, cuts and dis-
1273 coloured regions
- 1274 • Short-term leakage current measurement

1275 Any problems found in the basic inspection are documented for later cross-
1276 checking.

1277 The advanced quality assurance (QA-A) is performed in two centers, one in
1278 the Helsinki Institute of Physics (HIP) and one in the Wigner Research Centre in
1279 Budapest. The QA-A procedure includes the following measurements

- 1280 • Long-term leakage current measurement
- 1281 • High-resolution optical scanning

Figure 29: An example image taken of a GEM foil with false colors.

1282 • Gain uniformity check (In Budapest)

1283 In the procedure foils are classified according to a traffic light system. Red
1284 means the foil didn't pass the basic selection criteria and thus cannot be used.
1285 Yellow means it might be usable and green means that the foil passed all evalua-
1286 tions.

1287 **3.3.4 Optical scanning**

1288 The etching process is a delicate one; many things can go wrong, that are not visible
1289 by eye in the coarse optical inspection. It is expected that the hole parameters are
1290 connected with the foil's electric properties [], so a precise optical measurement
1291 can help in classifying the foils. For example, smaller holes create more intense
1292 and focused fields, which would result in larger amplification of their avalanche
1293 electrons, i.e. the local gain would be larger.

1294 The foils are scanned with the help of a scanning robot. The setup along with
1295 most of the software was developed at the Detector Laboratory of the University
1296 of Helsinki []

1297 Each image is a false colour superposition of two images, one with foreground
1298 illumination and one with background illumination. In this way one can observe
1299 the three relevant diameters of the foil, the top, middle and bottom diameters. The
1300 background light highlights the middle holes, while the foreground illumination
1301 captures either the top or the bottom depending on the orientation of the foil as
1302 the foils are scanned from both sides.

1303 The setup takes images with area about 11.3 mm × 8.5mm

1304 **Long term HV measurement of the GEM foils**

1305 **3.3.5 Particle identification**

1306 One guiding principle in the design of ALICE was to achieve good particle iden-
1307 tification (PID) over a large part of phases space and for several different particle
1308 types. In ALICE there are several detectors taking part in the identification of
1309 particles.

1310 One of the particle identification detectors is the transition radiation detector
1311 (TRD) [?]. Its main task is identifying electors with momenta larger than 1 GeV.
1312 Transition radiation is produced when highly relativistic particles traverse the
1313 boundary between to media having different dielectric constants. The average
1314 energy of the emitted photon is approximately proportional to the Lorentz factor γ

1315 of the particle, which provides an excellent way of discriminating between electrons
1316 and pion. ALICE TRD is made of a composite layer of foam and fibres. The
1317 emitted photons are then measured in six layers of Xe/CO₂ filled time expansion
1318 wire chambers.

1319 The time of flight (TOF) detector uses a very simple physics principle, i.e.
1320 calculating the velocity of the particle using the time of flight between two points.
1321 Combining this with the momentum of particle, obtained from the tracking de-
1322 tectors, one can calculate the mass of the particle, which identifies particles. The
1323 TOF detector consists of multigap resistive wire chambers. These are stacks of
1324 resistive plates spaced equally. They allow time of flight measurements in large
1325 acceptance with high efficiency and with a resolution better than 100 ps.

1326 The third specific particle identification detector is the high momentum particle
1327 identification (HMPID) detector. The HMPID uses a ring imaging Cherenkov
1328 counter to identify particles with momenta larger than 1 GeV. Particles moving
1329 through a material faster than the speed of light in the material will produce
1330 Cherenkov radiation. The velocity of the particle determines the angle at which
1331 the radiation is emitted. Measuring this angle gives the velocity of the particle.
1332 This can be again used to calculate the mass of the particle, if the momentum is
1333 known. In HMPID the material is a liquid radiator and the photons are measured
1334 with multiwire proportional chambers in conjunction with photocathodes.

1335 In addition to the specific particle identification detectors, the general purpose
1336 tracking detectors can be used for identification through the use of specific energy
1337 loss of charged particles traversing through a medium and the transition radiation
1338 emitted by charged particles when crossing the boundary between two materials.

1339 dE/dx measurements are provided by the last four layers of the ITS detector, i.e.
1340 the SDD and the SSD, thanks to their analog readout. [117] ITS provides particle
1341 identification in the low p_T region, up to 1GeV, and pions reconstructed in the
1342 standalone mode can be identified down to 100 MeV. Similar to ITS the TPC
1343 detector provides specific energy loss measurements. TPC can identify charged
1344 hadrons up to p_T 1 – 2GeV as well as light nuclei, He3 and He4.

1345 3.3.6 Electromagnetic Calorimeter

1346 Calorimeters are designed to measure the energy of particles. Electromagnetic
1347 calorimeters specialise in detecting particles that interact primarily through the
1348 electromagnetic interaction, namely photons and electrons. They are required in
1349 many neutral meson and direct photon analyses. In addition the energy informa-
1350 tion enhance jet measurements.

1351 ALICE has two electromagnetic calorimeters, the photon spectrometer (PHOS) [112]
1352 and the electromagnetic calorimeter (EMCal) [?]. PHOS is a homogeneous calorime-
1353 ter that consists of scintillating PbWO₄ crystals, which generate a bremsstrahlung

shower and produce scintillation light. The energy of the particle determines the amount of light produced. To improve the charged particle rejection, PHOS includes a charged particle veto detector (CPV) [?]. PHOS is built to have a very fine granularity, making it well suited for measuring direct photons and neutral mesons.

EMCal is a sampling calorimeter. It consists of layers of lead and scintillator tiles. The lead tiles produce the shower and scintillator tiles the light. The signal is then read with wavelength shifting fibres. The acceptance of EMCal in the azimuthal angle is $80 \text{ deg} < \phi < 187 \text{ deg}$. During long shutdown 1 in 2013-2015, EMCal was extended with the di-jet calorimeter (DCal) [111], giving an additional acceptance region of $260 \text{ deg} < \phi < 320 \text{ deg}$. This provides partial back-to-back coverage. In comparison to PHOS, EMCal has coarser granularity, but a significantly larger acceptance, making it suitable for jet physics.

3.3.7 Forward detectors

ALICE includes a few small and specialised detectors of importance. The event time is determined with very good precision ($< 25 \text{ ns}$) by the T0 detector [?]. T0 consists of two sets of Cherenkov counters that are mounted around the beam pipe on both sides of the interaction point. T0 gives the luminosity measurement in ALICE.

Another small detector in the forward direction is the V0 detector [?]. This consists of two arrays of segmented scintillator counters located at $-3.7 < \eta < -1.7$ and $2.8 < \eta < 5.1$. V0 is used as a minimum bias trigger and for rejection of beam-gas background. Particle multiplicity in the forward direction can be related to the event centrality. Thus V0 is the main detector used in centrality determination in PbPb collisions.

The multiplicity measurement of V0 is complimented by the forward multiplicity detector (FMD) [?]. FMD includes five rings of silicon strip detectors that make up the FMD. FMD gives acceptance in the range $-3.4 < \eta < -1.7$ and $1.7 < \eta < 5.0$.

During long shutdown 2 in 2019-2020, V0 and T0 will be replaced by the Fast Interaction Trigger (FIT) detector [?]. For historical reasons elements of FIT are also referred to as V0+ and T0+. FIT will allow centrality, event plane, luminosity and interaction time determination in the continuous readout mode, that ALICE will operate in after 2020.

For photon multiplicity measurement ALICE has the photon multiplicity detector (PMD) [?]. PMD uses two planes of gas proportional counters with a cellular honeycomb structure. PMD gives the multiplicity and spatial distribution of photons in the region $2.3 < \eta < 3.7$.

On top of the ALICE magnet there is an array of 60 large scintillators called

1393 the ALICE cosmic ray detector (ACORDE) [?]. ACORDE is used as a trigger
1394 for cosmic rays for calibration and alignment.

1395 The only hadronic calorimeters in ALICE are the zero degree calorimeters
1396 (ZDC) [?], which are located next to the beam pipe in the machine tunnel about
1397 116 m from the interaction point. There are two sets of calorimeters. One is
1398 made of tungsten, specialising in measuring neutrons, while the other, made of
1399 brass, is specialised in measuring protons. In heavy ion and especially in proton-
1400 lead collisions, ZDC gives information about the centrality of the event. ZDC is
1401 meant to detect spectators, i.e. parts of the colliding ions that do not take part
1402 in the interaction. If there are more spectators, the collisions is likely to be more
1403 peripheral.

1404 A new detector installed during the long shutdown 1 is the ALICE diffractive
1405 detector (AD) [?]. AD consists of two assemblies, one in each side of the interaction
1406 point, both made of two layers of scintillators. These assemblies are situated about
1407 17 m and 19.5 m away from the interaction points. The pseudorapidity coverage is
1408 $-6.96 < \eta < -4.92$ and $4.78 < \eta < 6.31$. AD greatly enhances ALICE's capability
1409 for diffractive physics measurements that require a large pseudorapidity gap.

1410 3.3.8 Muon spectrometer

1411 Outside the main magnet, ALICE has a spectrometer dedicated to measuring
1412 muons [?]. In heavy ion physics muons are mainly used to measure the production
1413 of the heavy quark resonances J/ψ , Ψ' , Υ , Υ' and Υ'' .

1414 The muon spectrometer consists of three parts, the absorber, the muon tracker
1415 and the muon trigger. The absorber is meant to remove the hadronic background
1416 as efficiently as possible. After the absorber there are ten plates of thin cathode
1417 strip tracking stations with high granularity, the muon tracker. After the muon
1418 tracker there is a layer of iron to filter out any remaining particles, other than
1419 muons. The muon trigger is located behind this layer. The trigger consists of four
1420 resistive plate chambers.

1421 3.3.9 Trigger

1422 4 Event and track selection

1423 5 Analysis method

1424 5.1 Jet Finding

1425 The analysis is performed by analysing jet constituents. In each collision event, the
1426 jets are reconstructed using FastJet [118] with the anti- k_T algorithm [119]. Jets for
1427 $R=0.4$ are selected in $|\eta| < 0.25$ to satisfy the fiducial acceptance of the EMCAL. In
1428 jet reconstruction both charged tracks with $p_T > 0.15 \text{ GeV}/c$ and neutral cluster
1429 with $p_T > 0.30 \text{ GeV}/c$ are considered. In the analysis, results are presented in
1430 terms of the jet transverse momentum $p_{T,\text{jet}}$.

1431 5.1.1 Anti k_T algorithm

1432 Jets are reconstructed using the anti- k_T algorithm [119]. The algorithm works by
1433 trying to undo the splittings through combining pseudojets/tracks.

$$k_{T,i}^2 = p_{T,i}^{2p}$$

1434 For each pair of protojets the distance measure is calculated as

$$k_{T,(i,j)}^2 = \min(p_{T,i}^{2p}, p_{T,j}^{2p}) \frac{\Delta R_{i,j}^2}{D^2},$$

1435 where

$$R_{i,j} = (\phi_i - \phi_j)^2 + (y_i - y_j)^2$$

1436 If $k_{T,i}$ is the smallest quantity then the protojet is a jet and it is removed
1437 from further consideration. If $k_{T,(i,j)}$ is the smallest quantity the two protojets are
1438 merged. Iterate until no protojets are left.

1439 The choice of the power p in the distance measure depends on the algorithm
1440 used

- 1441 • $p = 1$: k_T algorithm
- 1442 • $p = 0$: Cambridge Aachen algorithm
- 1443 • $p = -1$: anti- k_T algorithm

1444 With the choice $p = -1$ in anti- k_T algorithm, the softest splittings are undone
1445 first.

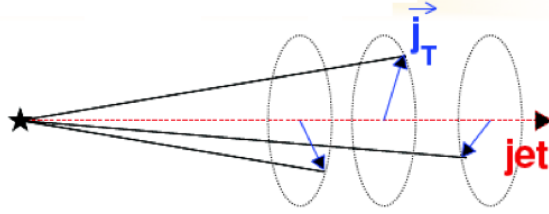


Figure 30: Illustration of \vec{j}_T . The jet fragmentation transverse momentum, \vec{j}_T , is defined as the transverse momentum component of the track momentum, \vec{p}_{track} , with respect to the jet momentum, \vec{p}_{jet} .

5.2 j_T

The jet fragmentation transverse momentum, j_T , is defined as the component of the constituent particle momentum, \vec{p}_a , transverse to the jet momentum, \vec{p}_{jet} . The resulting \vec{j}_T is illustrated in Fig. 30. The length of the \vec{j}_T vector is

$$j_T = \frac{|\vec{p}_{\text{jet}} \times \vec{p}_{\text{track}}|}{|\vec{p}_{\text{jet}}|}. \quad (35)$$

It is commonly interpreted as a transverse kick with respect to the initial hard parton momentum that is given to a fragmenting particle during the fragmentation process, which is a measure of the momentum spread of the jet fragments [1].

The reconstructed jet axis is used for j_T reference. Any charged track within a fixed cone with radius R is taken as a jet constituent, as opposed to using the constituent list provided by the jet algorithm. Anti- k_T produces jets that are very circular in shape. Thus this doesn't change the constituent list considerably. Neutral tracks are used only in jet reconstruction.

5.2.1 1 over j_T

j_T results are shown as

$$\frac{1}{j_T} \frac{dN}{dj_T}$$

distributions. The logic behind this is that j_T is inherently a two-dimensional observable, comprised of j_{Tx} and j_{Ty} components. So the actual physical observable would be

$$\frac{d^2N}{dj_{Tx} dj_{Ty}}$$

1462 Changing into polar coordinates with $j_{\text{Tr}} = j_{\text{T}}$ and θ gives

$$\frac{d^2N}{j_{\text{T}} dj_{\text{T}} d\theta},$$

1463 where j_{T} over the azimuth θ should stay constant and it can be integrated over
1464 giving

$$\frac{1}{2\pi} \frac{dN}{j_{\text{T}} dj_{\text{T}}}.$$

1465 5.3 Unfolding

1466 Extend unfolding

1467 The resulting j_{T} distributions are corrected for the detector inefficiency using
1468 the unfolding method. The response matrix for the unfolding is obtained from a
1469 PYTHIA [120] simulation.

Measured distributions are affected by two main factors; Limited acceptance -
The probability to observe a given event is less than one and limited resolution -
Quantity x cannot be determined exactly, but there is a measurement error. True
 $f(x)$ and measured $g(y)$ distributions are connected by a convolution integral.
Including statistical fluctuations this becomes

$$\hat{g}(y) = \int_a^b A(y, x) f(x) dx + \epsilon(y),$$

where A is the detector response obtained by Monte Carlo simulations and $\epsilon(y)$
is the term coming from statistical fluctuations. If x and y are discrete variables
we have

$$\hat{g}_i = \sum_{j=1}^m A_{ij} f_j + \epsilon_i,$$

Or in matrix form

$$\hat{g} = Af + \epsilon$$

If the only detector effect is limited acceptance, A is a diagonal matrix. In a
general discrete case the (naive) solution is obtained by the inverse matrix

$$\hat{f} = A^{-1} \hat{g}$$

1470 However this usually leads to oscillating solutions and determining the inverse
1471 matrix can be difficult.

1472 Two common methods to perform this inversion are Bayesian and SVD unfold-
1473 ing methods. Often the solution requires some additional *a priori*. For example
1474 the solution should be smooth in most cases.

1475 **5.3.1 Bayesian unfolding**

The bayesian (iterative) method is based on the Bayes formula [].

$$P(C_i|E_j) = \frac{P(E_j|C_i) P_0(C_i)}{\sum_{l=1}^{n_C} P(E_j|C_l) P_0(C_l)},$$

1476 i.e. Probability of Cause ("truth") C_i given Effect ("observed") E_j is proportional to the probability of observing E_j given C_i (response matrix) and the truth distribution $P_0(C_i)$.

At first P_0 is given some starting distribution, either a uniform distribution or some guess of the final distribution. Taking into account the inefficiency this gives

$$\hat{n}(C_i) = \frac{1}{\epsilon_i} \sum_{j=1}^{n_E} n(E_j) P(C_i|E_j),$$

where

$$P(C_i|E_j) = \frac{P(E_j|C_i) P_0(C_i)}{\sum_{l=1}^{n_C} P(E_j|C_l) P_0(C_l)},$$

and

$$\hat{n}(C_i) = \frac{1}{\epsilon_i} \sum_{j=1}^{n_E} n(E_j) P(C_i|E_j).$$

First $P(C_i|E_j)$ is calculated with the uniform distribution or best guess of the shape of the distribution. This is then used to calculate the new distribution $\hat{P}(C_i)$

$$\hat{N}_{true} = \sum_{i=1}^{n_C} \hat{n}(C_i), \hat{P}(C_i) = P(C_i|n(E)) = \frac{\hat{n}(C_i)}{\hat{N}_{true}}$$

1479 P_0 is then replaced with \hat{P} and the procedure is repeated until an acceptable 1480 solution is found.

1481 **5.3.2 Toy Monte Carlo**

remove? A toy Monte Carlo simulation was performed to see the performance in an ideal case. Sample jet p_T values from observed p_T distribution. Starting from this p_T start creating tracks with

$$p_{track} = z_{track} p_{T,jet}$$

1482 where z_{track} is sampled from the observed z distribution. All tracks below 0.15GeV 1483 are discarded. Sampling is continued until the sum of the track transverse momenta

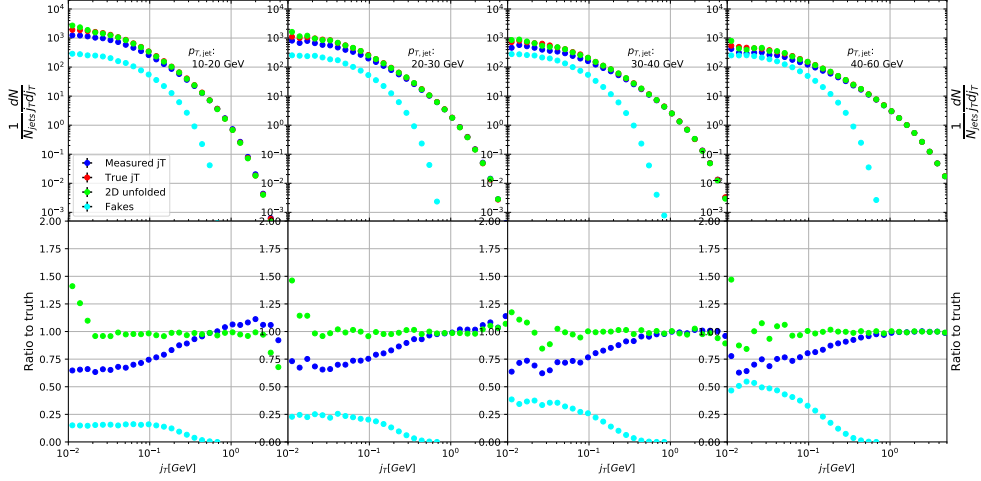


Figure 31: Results from unfolding in Toy Monte Carlo

1484 exceeds the jet transverse momentum. Jet is then defined as the sum of the track
 1485 momenta.

1486 Simultaneously a p_T dependant observation efficiency is applied to the tracks
 1487 and a separate observed jet is calculated using only the observed tracks. Addi-
 1488 tionally a set of fake tracks is added to the observed jet. Tracks are always either
 1489 observed or not at the true momentum. No smearing is added to the observed
 1490 momentum.

Afterwards the tracks are looped over for j_T calculation. For observed tracks we calculate j_T with respect to both the true jet axis and the observed jet. 2D Response matrix is filled with

$$(j_{T,\text{obs}}, p_{T,\text{jet},\text{obs}}, j_{T,\text{true}}, p_{T,\text{jet},\text{true}})$$

1491 In practice this is done with a set of 3D histograms, where $p_{T,\text{jet},\text{true}}$ determines
 1492 the histogram index and the remaining three values the bin in the 3D histogram.

1493 After creating the response matrices, an identical procedure is carried out the
 1494 create testing data. Now instead of filling response matrices, 2D histograms are
 1495 filled with $(j_{T,\text{obs}}, p_{T,\text{jet},\text{obs}})$ and $(j_{T,\text{true}}, p_{T,\text{jet},\text{true}})$

1496 The observed distributions are unfolded using RooUnfold's 2D Bayesian (iter-
 1497 ative) algorithm. Results are shown in figure 31.

1498 5.3.3 Pythia Response matrices

1499 Response matrices are filled through correlation between MC detector and particle
 1500 level jets and tracks.

Table 2: j_T and p_T ranges used in unfolding. The same ranges are used for detector and truth level.

	j_T	$p_{T\text{jet}}$
Min	0.01	5
Max	20	500

The ranges of both j_T and $p_{T\text{jet}}$ extend the ranges in end results. These are shown in Tab. 2. The ranges are the same in detector and particle level.

When calculating j_T for MC particles the code checks whether a corresponding detector level track exists and if that track had a j_T value. Additionally check for detector level tracks that don't have corresponding particle level track or that track does not have j_T value.

Possible cases:

- We find a corresponding track with a j_T value, response matrix is filled normally with $(j_T^{obs}, p_T^{obs}, j_T^{true}, p_T^{true})$
- We don't find a corresponding track. Record (j_T^{true}, p_T^{true}) as a miss
- We find a corresponding track, but it didn't have j_T value. Most likely because it was not part of a jet. Similary record (j_T^{true}, p_T^{true}) as a miss
- For detector level tracks with no correspondence in particle level set record cord (j_T^{obs}, p_T^{obs}) as a fake

5.3.4 2D response matrices

In the analysis code the response matrix is made of an array of 3 dimensional histograms, with $(j_{T,obs}, p_{T,obs}, j_{T,true})$ as axes. The histogram index gives the $p_{T,true}$ value.

5.3.5 Unfolding algorithm

As a primary method unfolding is performed with an iterative (bayesian) algorithm using the RooUnfold [121] package. The number of iterations used is 4.

5.3.6 Effect of number of iterations

The iterative unfolding algorithm permits the change of number of iterations. The unfolding was carried out using different numbers of iterations. The results from these different cases are shown in Fig. 32. The results are compared to the default unfolding algorithm with 4 iterations. The difference in results between the different cases is mostly less than 2.5%.

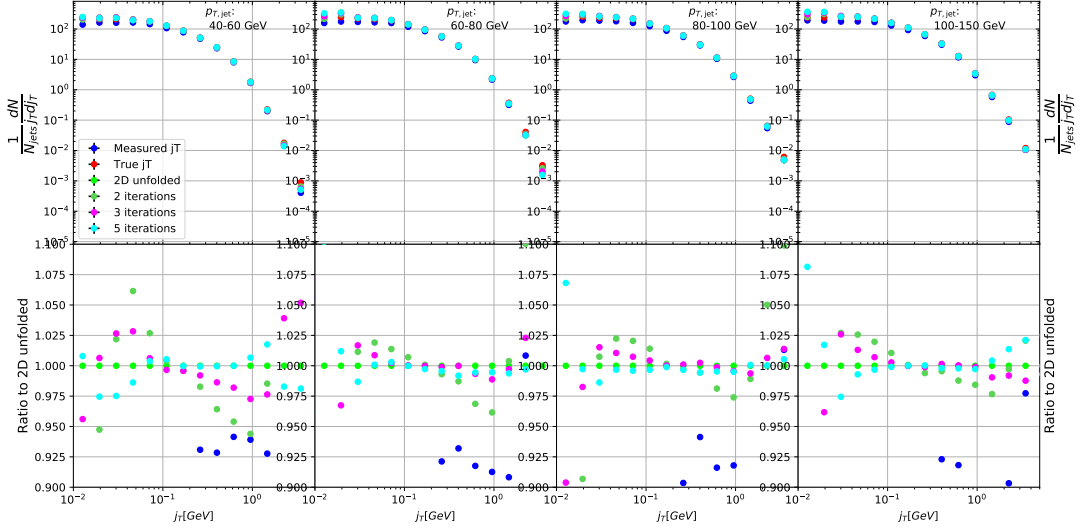


Figure 32: Unfolding with different number of iterations

1528 5.3.7 Effect of different prior

1529 The iterative algorithm requires a prior estimate of the shape of the distribution.
 1530 As a default prior the truth (particle level) distribution is used. To test the effect
 1531 of changing the prior we instead use the unfolded j_T distribution as prior. The
 1532 results are compared to the unfolding algorithm with the default prior. This is
 1533 shown in Fig. 33. The difference in results between the different cases is mostly less
 1534 than 2.5%.

1535 5.3.8 Effect of p_T truncation

1536 5.3.9 Unfolding closure test

1537 Pythia set is divided in 2 halves. First is used to fill the response matrices, as well
 1538 as record missed and fake tracks. Second half is used to test the effectiveness of
 1539 the unfolding method. Jet p_T distributions are shown in figure 35a and response
 1540 matrix are shown in figure 35b.

1541 Response matrices within single jet p_T bins are shown in figure 36. Results
 1542 from the closure test are shown in figure 37. In the lowest jet p_T bins unfolding
 1543 fails to recover the true distribution. The lowest jet p_T bins are dominated by
 1544 combinatorial jets and thus the true detector response is likely not retrieved.

1545 Above jet p_T 30-40 GeV the distribution is recovered well in the mid j_T region.
 1546 At $j_T < 0.1$ there is clear discrepancy. The final results are shown only for $j_T > 0.1$.
 1547 Additionally there is some discrepancy at very high j_T . This is taken into account

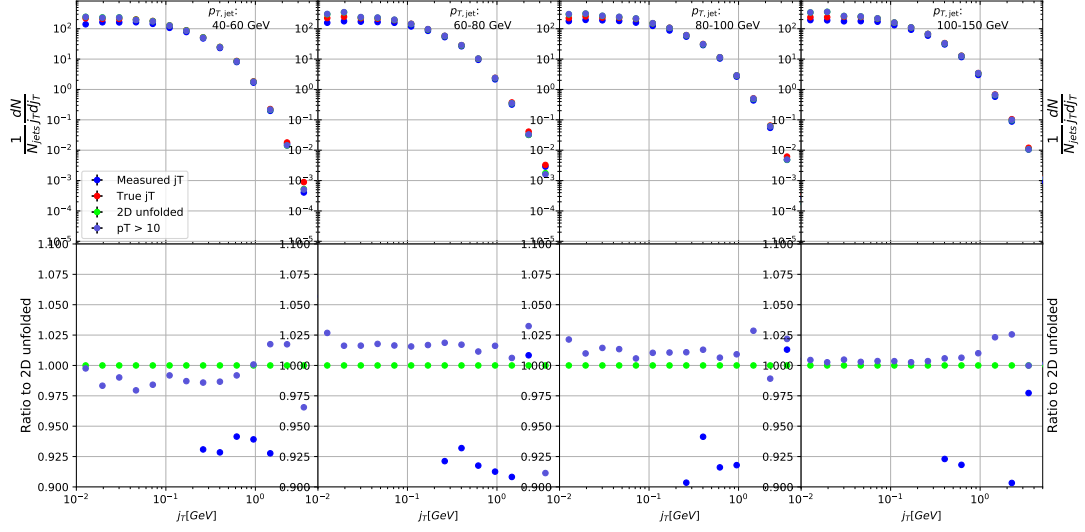


Figure 33: Effect of changing minimum jet p_T used in unfolding from 5 to 10 GeV

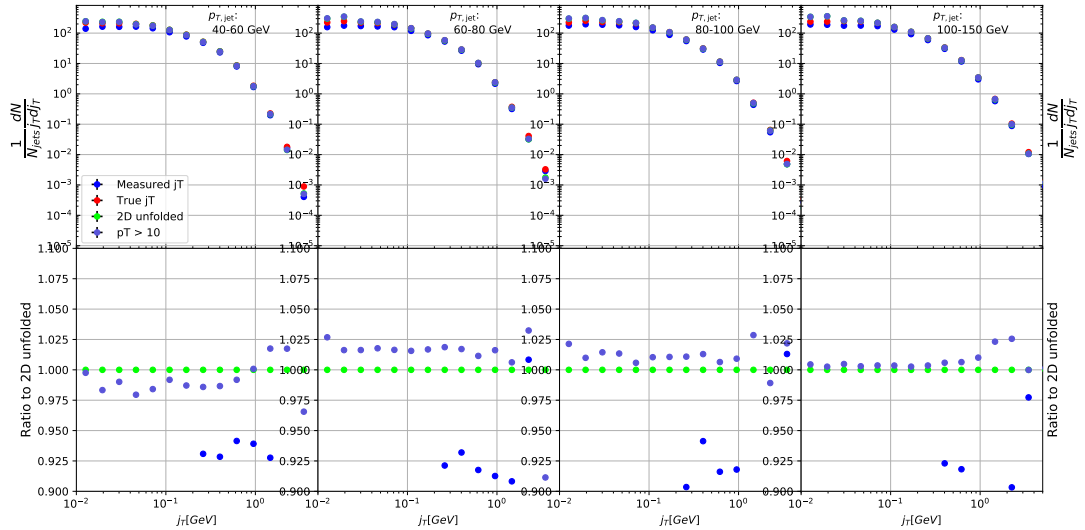
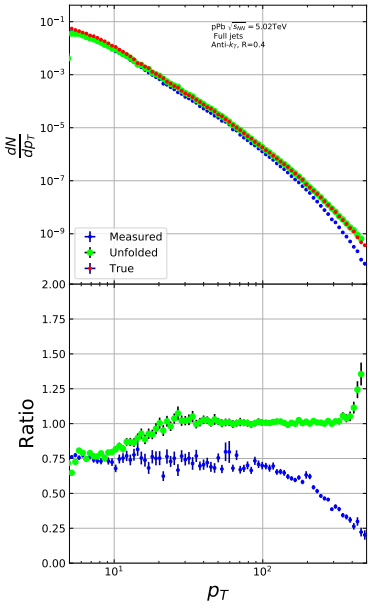
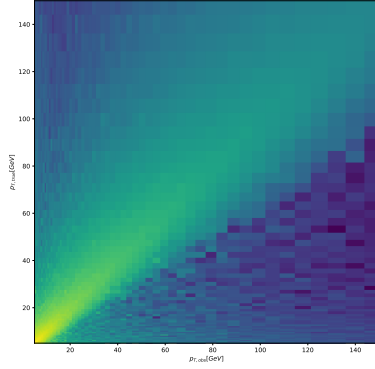


Figure 34: Effect of changing minimum jet p_T used in unfolding from 5 to 10 GeV



(a) Unfolded jet p_T distribution in Pythia closure test



(b) Jet p_T response matrix from unfolding closure test

in the unfolding systematics. (TODO: Show this)

1549 5.4 Background

1550 When calculating j_T distribution for jet constituents there is a contribution from
 1551 underlying event (UE), i.e. tracks that just happen to be close to the jet axis.
 1552 To find the signal coming from the actual jet we need to subtract the background
 1553 (UE) contribution. On a jet-by-jet basis this is impossible, so we try to estimate
 1554 the background by looking at regions of the detector where there are no tracks
 1555 from jets, but only uncorrelated tracks from the underlying event.

1556 The underlying event is estimated by looking at an imaginary jet cone perpen-
 1557 dicular to the observed jet axis ($\frac{\pi}{2}$ Rotation in ϕ). j_T is calculated for any tracks
 1558 found within this cone. The vector sum of the individual track momentum and
 1559 the imaginary jet axis is used as reference for j_T . The background obtained in
 1560 this manner is subtracted from the unfolded inclusive j_T distribution, which gives
 1561 the resulting signal distribution. To make sure there is no jet contribution in the
 1562 background, any events with jets inside the perpendicular cone are not used for
 1563 background estimation.

1564 We have two methods for background estimation. In the first we look at the
 1565 direction perpendicular to the jet. This is assumed to be the region least likely to
 1566 contain jet contributions.

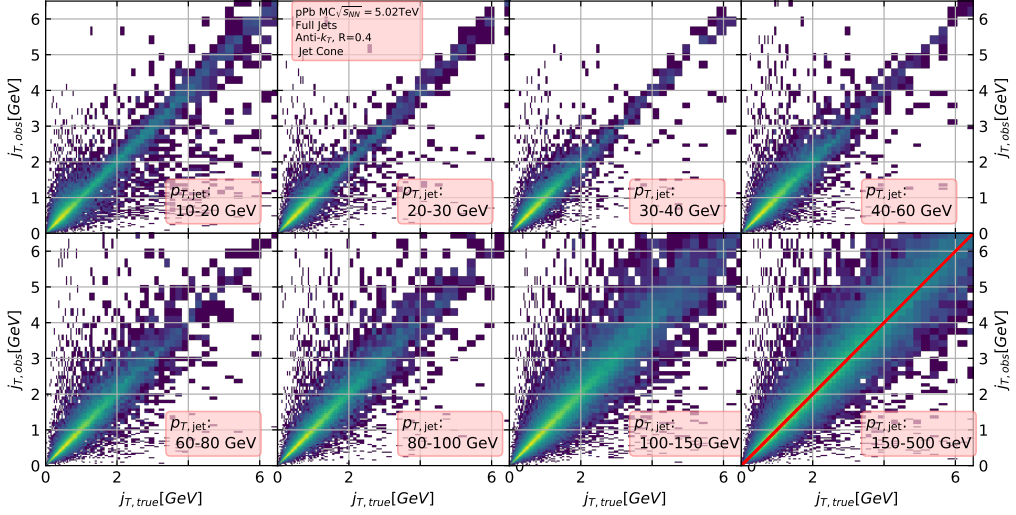


Figure 36: j_T Response matrices in single jet p_T bins

1567 In the second method we randomly assign the tracks of event new ϕ and η
 1568 values. The result is guaranteed to be uncorrelated.

1569 5.4.1 Perpendicular cone background

1570 After calculating the j_T values for tracks in the jet, we rotate the jet axis by $\frac{\pi}{2}$
 1571 in positive ϕ direction. We check that there are no other jets closer than $2R$ to
 1572 the rotated axis. If there are then background calculation is skipped for this jet.
 1573 Probability of this happening is 1-2% depending on the jet p_T bin.

1574 If we don't find other jets in the vicinity we move on to estimate the background.
 1575 We find all tracks within a cone of radius R around the rotated axis and calculate
 1576 j_T of these tracks with respect to the rotated axis. Auto-correlations are added to
 1577 match effect to jet. (see 5.4.3)

1578 5.4.2 Random background

1579 In the random background method we look at all tracks in the event, except for
 1580 tracks close to jets found by the jet algorithm. We randomly assign new η and ϕ
 1581 values to all tracks using uniform distribution. $|\eta| < 1.0$ p_T values are kept the
 1582 same. To increase statistics there is a possibility to create a number of random
 1583 tracks for each actual track. In the analysis we currently do this 10 times for each
 1584 track. Again the track p_T value is kept the same.

1585 We create a random jet cone from uniform η and ϕ distributions. Here $|\eta| <$
 1586 0.25. Now we calculate j_T of the random tracks with respect to the random cone

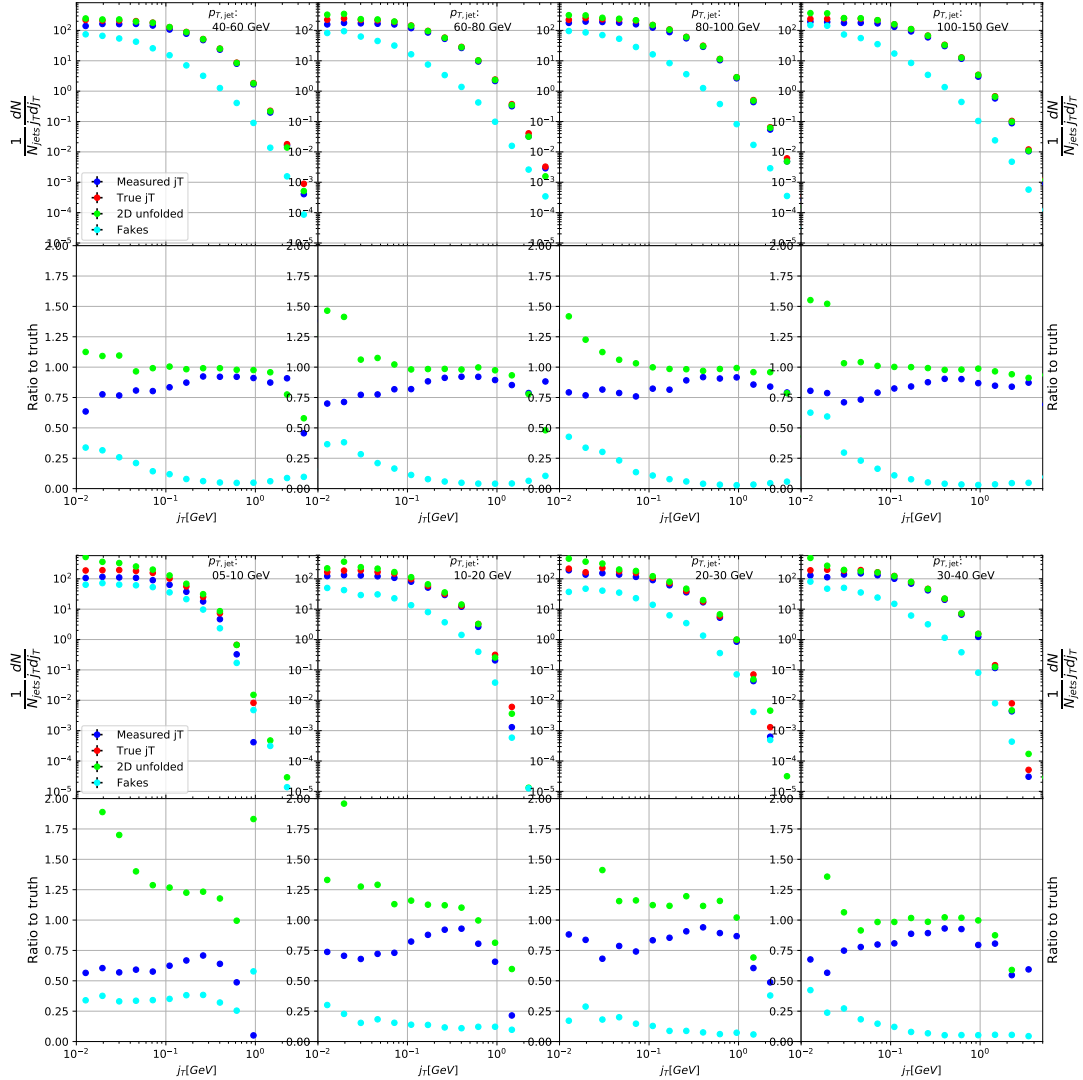
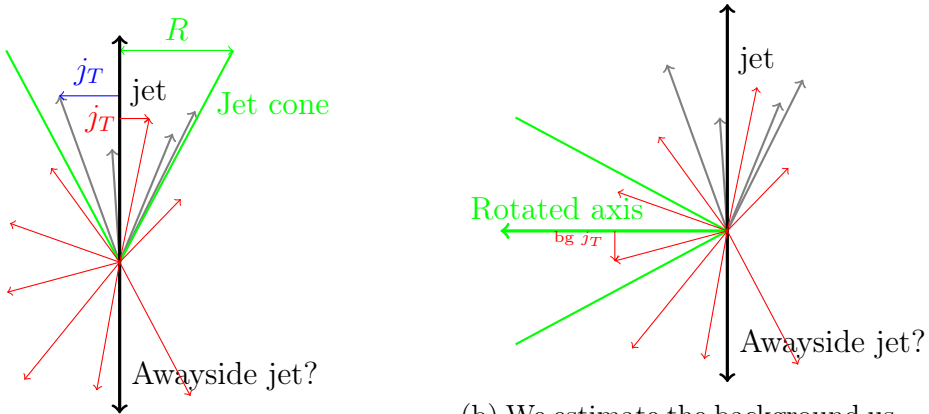
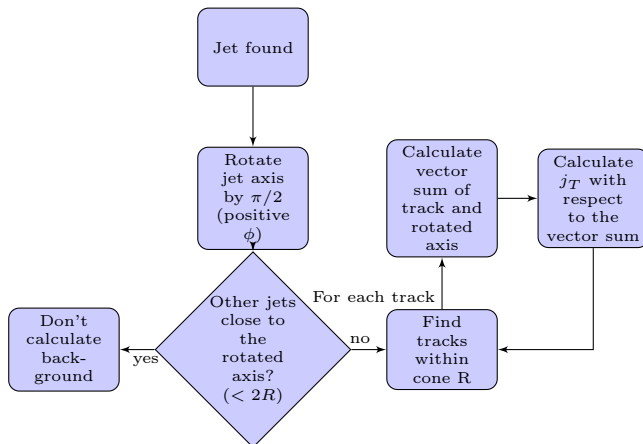


Figure 37: Pythia closure test results. Fake tracks include also tracks that do exist in the true dataset, but for one reason or another were not given j_T values. j_T is only calculated for tracks that are associated with jets



(a) Red is underlying event while gray tracks represent the signal
(b) We estimate the background using a cone where the axis is perpendicular to the jet axis



1587 axis. Auto-correlations are added before calculating j_T (see 5.4.3)

1588 5.4.3 Auto-correlations

1589 Jet axis is simply a vector sum of all its constituents. Thus having an additional
1590 track in the jet from the underlying event moves the jet axis towards this track.
1591 Since the axis is now closer to the track, it has a smaller j_T value. Assuming a 1
1592 GeV background track at the edge of a $R = 0.4$ the j_T value would be 0.4GeV.
1593 If this is added to a 5GeV jet, the j_T value becomes 0.33GeV. In a 50GeV jet it
1594 would be 0.39GeV. This is a region where the inclusive j_T distribution is domi-
1595 nated by background. The distribution is also steeply falling. Overestimating the
1596 background can lead to a situation where the background estimation exceeds the
1597 inclusive distribution.

1598 To take this effect into account we can't use a fixed axis for background, but
1599 it has to behave like a jet would when additional tracks are added. Thus before
1600 calculating j_T values we make a vector sum of the track and the axis used for back-
1601 ground, which is either the perpendicular cone axis or the random axis depending
1602 on the background method. In each case the momentum of this background axis
1603 is assumed to be the same as the jet which initiated the background estimation.

1604 In pPb data there is on average about one underlying event track in a $R = 0.4$
1605 cone.

1606 Extend Background, Perp. cone vs. Random

1607 5.5 Fitting

1608 The resulting signal distribution are fitted with a 2 component function shown in
1609 Eq. 36. Gaussian distribution is used for low j_T and an inverse gamma function is
1610 used for high j_T . The gaussian is taken to have the center at $j_T = 0$. In total this
1611 gives 5 parameters.

$$\frac{1}{N_{\text{jets}} j_T \text{d}j_T} \frac{\text{d}N}{\text{d}j_T} = \frac{B_2}{B_1 \sqrt{2\pi}} e^{-\frac{j_T^2}{2B_1^2}} + \frac{B_3 B_5^{B_4}}{\Gamma(B_4)} \frac{e^{-\frac{B_5}{j_T}}}{j_T^{B_4+1}} \quad (36)$$

1612 To achieve stable results the fitting is performed in two steps. First each
1613 component is fitted separately. Gaussian component is fitted to the low end in j_T .
1614 Inverse gamma component is fitted to j_T above 1 GeV/c. After getting the results
1615 from the individual fits they are combined into a single function with initial values
1616 from the individual results and an additional fit is performed. Fitting only the
1617 gaussian component to the entire distribution produces approximately the same
1618 result as the gaussian component in the two-component model.

1619 After getting the fit function $\sqrt{\langle j_T^2 \rangle}$ (RMS) and yield values are extracted
1620 separately from each component. The narrow component RMS is

$$\sqrt{\langle j_T^2 \rangle} = \sqrt{2}B_1,$$

1621 and the wide component RMS value is calculated as

$$\sqrt{\langle j_T^2 \rangle} = \frac{B_5}{\sqrt{(B_4 - 2)(B_4 - 3)}},$$

1622 where it is required that $B_4 > 3$.

1623 6 Systematic uncertainties

1624 Extend Systematics

1625 The systematic uncertainties in this analysis come from the background esti-
1626 mation, the unfolding procedure and the cuts used to select the tracks. Tracking
1627 uncertainties are estimated from variations of the track selection cuts defined in
1628 Sec. 2. The resulting variations in RMS are shown in Table 4. The uncertainties
1629 from unfolding and background subtraction are of the same magnitude.

1630 The systematics in background estimation were studied using an alternative
1631 method to extract the background, mainly the random background method. The
1632 resulting uncertainty is below 5% for the wide component RMS and below 9% for
1633 the narrow component RMS.

1634 The systematic uncertainty that arises from the unfolding procedure is esti-
1635 mated by performing the unfolding with two separate methods. Data corrected
1636 by the iterative unfolding method are used as the results and the SVD unfolding
1637 method is employed to estimate the uncertainty. In a PYTHIA closure test the
1638 true distribution was in general found to be between the unfolded distributions
1639 from the iterative and SVD method. The difference between the methods when
1640 unfolding data should give a reasonable estimate of the unfolding uncertainty. The
1641 resulting uncertainty is below 8% for both wide and narrow component RMS.

1642 The different source of the systematic uncertainty are considered as uncorre-
1643 lated and the values of each source are summed in quadrature. The resulting
1644 uncertainty is 9 % for the wide component RMS and 12 % for the narrow compo-
1645 nent RMS.

1646 There is no tracking and no unfolding uncertainty in the Monte Carlo simula-
1647 tions.

Table 3: Summary of systematic errors

Systematic	Wide RMS	Narrow RMS
Background	5 %	9 %
Unfolding	8 %	8 %
Tracking	? %	? %
Total	9 %	12%

1648 7 TPC Upgrade?

1649 8 Systematic errors

1650 8.1 Background subtraction

1651 Fits are performed on both perpendicular cone and random background signals.
 1652 Difference between them is taken as the systematic error. The fits for individ-
 1653 ual bins from the random background method are shown in figure 41. Resulting
 1654 differences between the methods for different components are shown in figure 40.

1655 8.2 Unfolding

1656 Unfolding is performed using both SVD and Bayesian unfolding. Difference be-
 1657 tween the methods is taken as the systematic error. Since SVD unfolding does
 1658 not have a 2 dimensional options, the unfolding is done bin by bin. The resulting
 1659 distributions after SVD unfolding and background subtraction with the perpendic-
 1660 ular cone method are shown in fig ???. Resulting differences between the methods
 1661 for different components are shown in figure 42.

1662 8.3 Tracking

1663 8.4 Combining systematics

1664 Resulting systematic errors are shown in table 4. Systematic errors are combined
 1665 bin-by-bin in quadrature to get the total systematic errors.

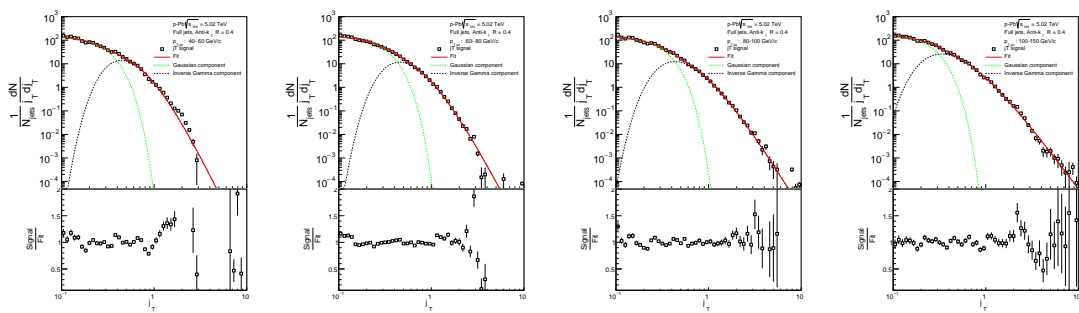


Figure 39: j_T signal with random background subtraction fits in different jet p_T bins

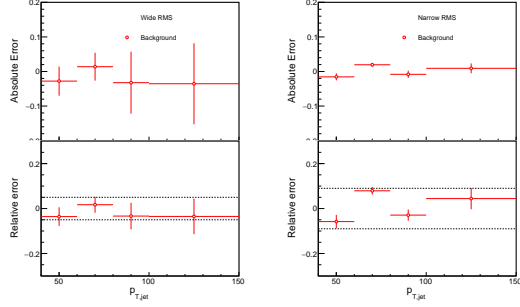


Figure 40: Differences between perpendicular cone and random background subtraction in the resulting RMS values.

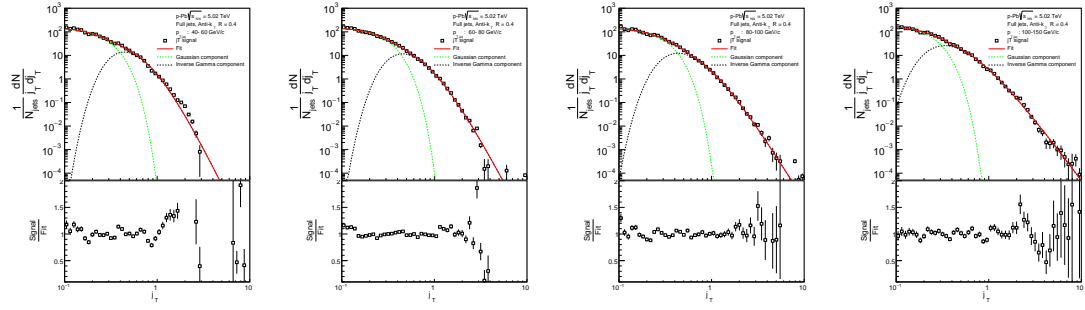


Figure 41: j_T signal with random background subtraction fits in different jet p_T bins

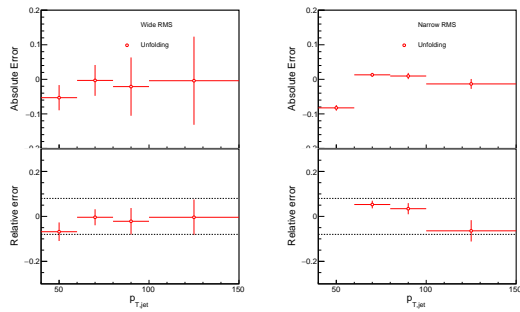


Figure 42: Differences between Bayesian and SVD unfolding in the resulting RMS values

Table 4: Summary of systematic errors

Systematic	Wide RMS	Narrow RMS
Background	5 %	9 %
Unfolding	8 %	8 %
Total	9 %	12%

1666 9 Results

1667 9.1 statistics

1668 Number of jets in different datasets and with different jet finders is shown in table
 1669 5. Background statistics for number of background cones (number of jets minus
 1670 number of discarded cones) are shown in table 6. Ratio of background cones to
 1671 number of jets is shown in table 7. The likelihood of having to discard a jet from
 background calculation is about 1-2%.

Table 5: Number of found jets by dataset and jet p_T bin

Jet p_T	5-10	10-20	20-30	30-40	40-60	60-80	80-100	100-150	150-500
MBFullR04	4969393	621753	32552	5584	1974	310	90	37	5
MBFullR05	4750567	826598	42373	5543	1719	276	73	29	3
MBChargedR04	3144538	673419	37783	4121	1009	148	36	12	1
MBChargedR05	2229247	175763	7961	1270	410	61	12	3	
TriggeredFullR04	187557	115927	78138	51317	39262	8621	2409	1167	171
TriggeredFullR05	99991	77147	48612	34325	28104	6342	1726	794	104
TriggeredChargedR04	37411	29945	18186	13148	11142	2517	675	326	44
TriggeredChargedR05	433155	175031	54789	19776	10626	1983	457	194	15

1672

Table 6: Number of background cones used in perpendicular cone background calculation

Jet p_T	5-10	10-20	20-30	30-40	40-60	60-80	80-100	100-150	150-500
MBFullR04	4947583	617895	32357	5548	1965	310	90	37	5
MBFullR05	4710217	815461	41584	5439	1698	273	73	29	3
MBChargedR04	3117495	661106	36739	4014	988	144	36	12	1
MBChargedR05	2195286	172919	7860	1249	406	61	12	3	
TriggeredFullR04	186574	115376	77949	51216	39196	8603	2405	1167	171
TriggeredFullR05	99102	76462	48320	34216	28038	6334	1722	794	103
TriggeredChargedR04	37160	29543	17988	13099	11129	2515	675	326	44
TriggeredChargedR05	313421	140707	45229	16243	8709	1604	377	154	14

Table 7: Ratio of background cone number to number of jets

MBFullR04	99.56%	99.38%	99.40%	99.36%	99.54%	100.00%	100.00%	100.00%	100.00%
MBFullR05	99.15%	98.65%	98.14%	98.12%	98.78%	98.91%	100.00%	100.00%	100.00%
MBChargedR04	99.14%	98.17%	97.24%	97.40%	97.92%	97.30%	100.00%	100.00%	100.00%
MBChargedR05	98.48%	98.38%	98.73%	98.35%	99.02%	100.00%	100.00%	100.00%	100.00%
TriggeredFullR04	99.48%	99.52%	99.76%	99.80%	99.83%	99.79%	99.83%	100.00%	100.00%
TriggeredFullR05	99.11%	99.11%	99.40%	99.68%	99.77%	99.87%	99.77%	100.00%	99.04%
TriggeredChargedR04	99.33%	98.66%	98.91%	99.63%	99.88%	99.92%	100.00%	100.00%	100.00%
TriggeredChargedR05	72.36%	80.39%	82.55%	82.13%	81.96%	80.89%	82.49%	79.38%	93.33%

1673 9.2 Data

1674 9.3 Inclusive results

1675 Results in figure 43

1676 As outlined in Section ?? the inclusive j_T distributions and corresponding
 1677 backgrounds are obtained for different jet p_T bins starting from $10 \text{ GeV} < p_{T\text{jet}} <$

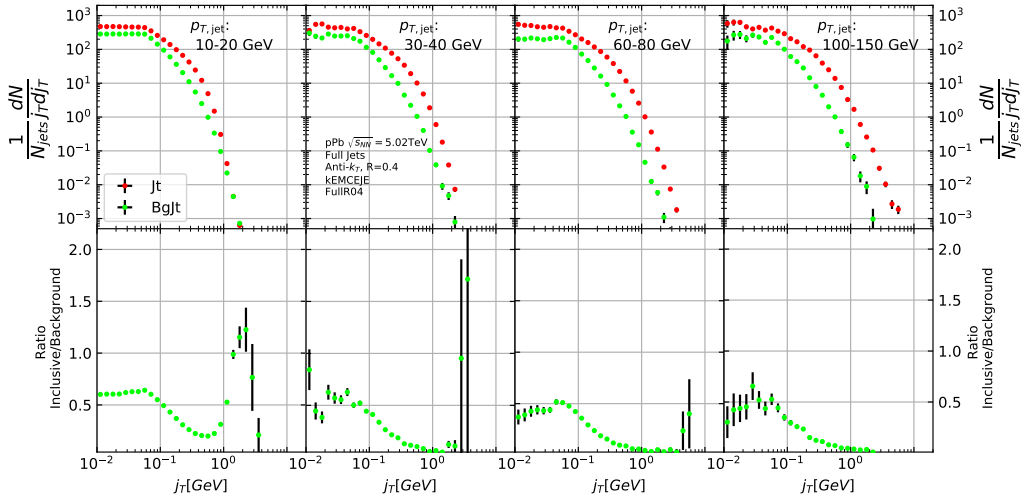


Figure 43: Inclusive j_T with background

1678 20 GeV. Later the lowest p_T bins are omitted because of problems in unfolding
1679 and fitting. The results are shown in Fig. 43. The background distribution the
1680 figure is obtained by the perpendicular cone method.

1681 9.4 Background

1682 Comparison between perpendicular cone and random background in figure 44. The
1683 advantage of the random background method is the added amount of statistics as
1684 the procedure can be repeated several times for each event. However, it seems that,
1685 especially in the highest $p_{T,jet}$ bins there is some jet contribution left at the high
1686 end. One should note that the results from perpendicular cone background show no
1687 observable change between $p_{T,jet}$ bins. It is a good indication that the background
1688 is actually dominated by the underlying event over the entire j_T region.

1689 9.5 Comparison between A and C side

1690 In 2013 there were some issues with tracking. To rule out effects on j_T distributions
1691 a study was performed comparing j_T distributions between A and C side. No
1692 systematic differences were observed.

1693 9.6 Subtracted signal

1694 Results in figure 46. Comparison between signals with different backgrounds in
1695 figure 47

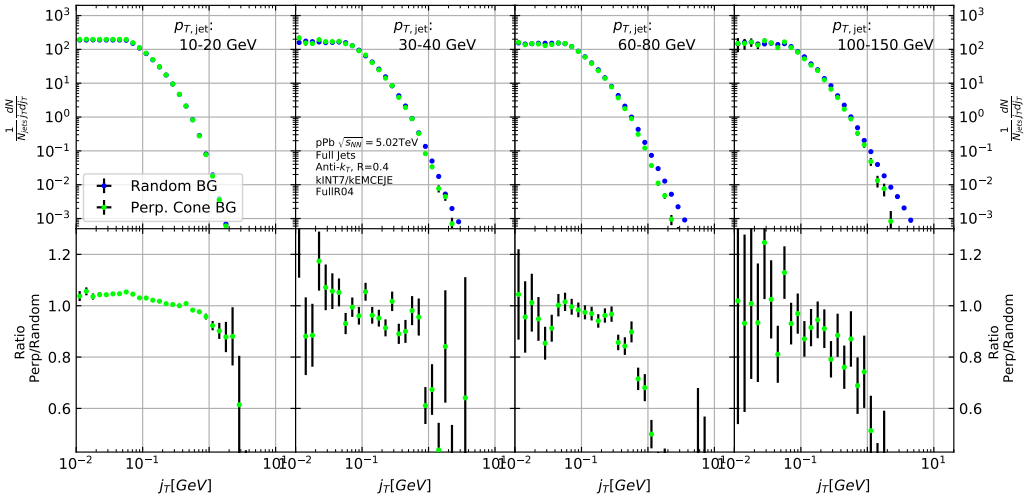


Figure 44: j_T background with two different methods

1696 9.7 Fitting

1697 Fits of j_T distributions in different jet p_T bins with $p_T > 40\text{GeV}$ are shown in figure
 1698 48. Additional jet p_T bins are shown in appendix ???. In lowest jet p_T bins the
 1699 jets are mainly combinatorial which makes background subtraction and unfolding
 1700 difficult and thus the signal can't be trusted.

1701 The fits describe the data well. There is some fluctuation of the order of 10 %
 1702 around the fit function. At hight j_T the statistical errors in the signal are large.

1703 9.7.1 Results

1704 RMS and yield results with systematic errors are shown separately in figure 49.
 1705 Figure 50 shows RMS values for both components combined. The figure also
 1706 includes results from a PYTHIA simulation.

1707 9.8 Comparison to dihadron results

1708 Comparison to RMS values in dihadron analysis [?] are shown in figure Dihadron
 1709 results from [?]. For comparison the dihadron trigger p_T bins are converted to jet
 1710 p_T bins and vice versa. Bin-by-bin comparison is still not possible, but dihadron
 1711 analysis gives systematically larger RMS values. This could be caused by several
 1712 kinematical factors. In jet j_T analysis the jet cone limits possible j_T values and
 1713 thus the width and RMS of the j_T distributions. The effect of this limitation can
 1714 be studied by changing the cone size as is described in section 9.9.

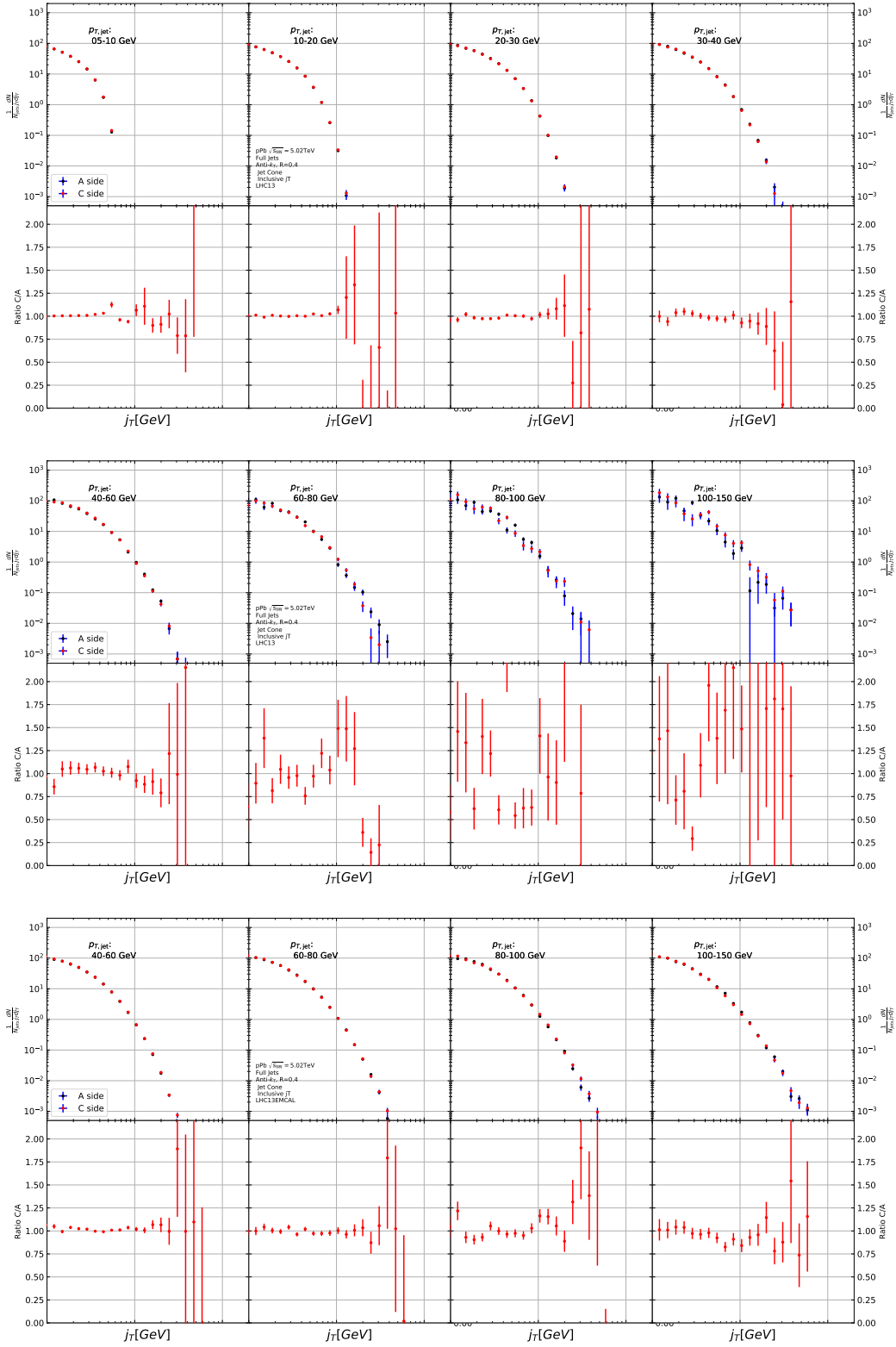


Figure 45: Comparison of inclusive j_{T8} distributions between A and C side for minimum bias and EMCAL triggered data.

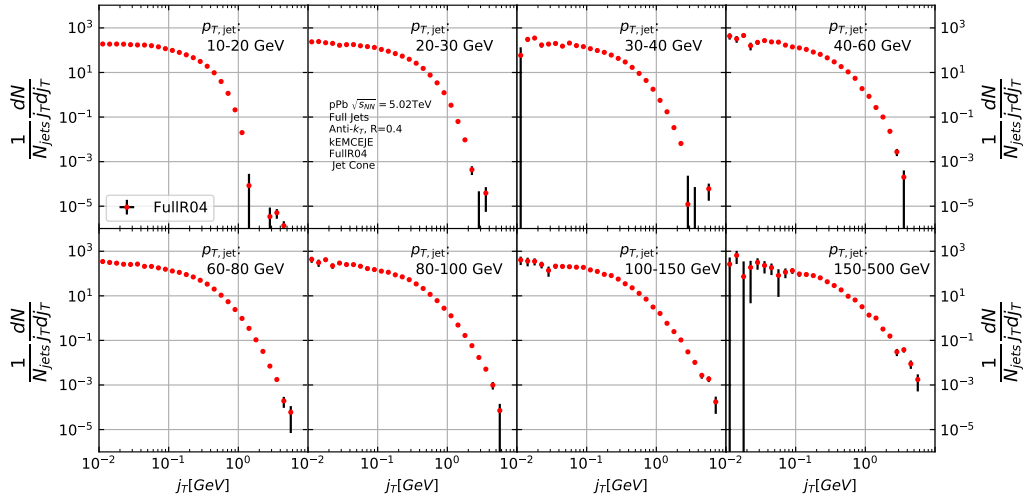


Figure 46: j_T signal with background subtracted

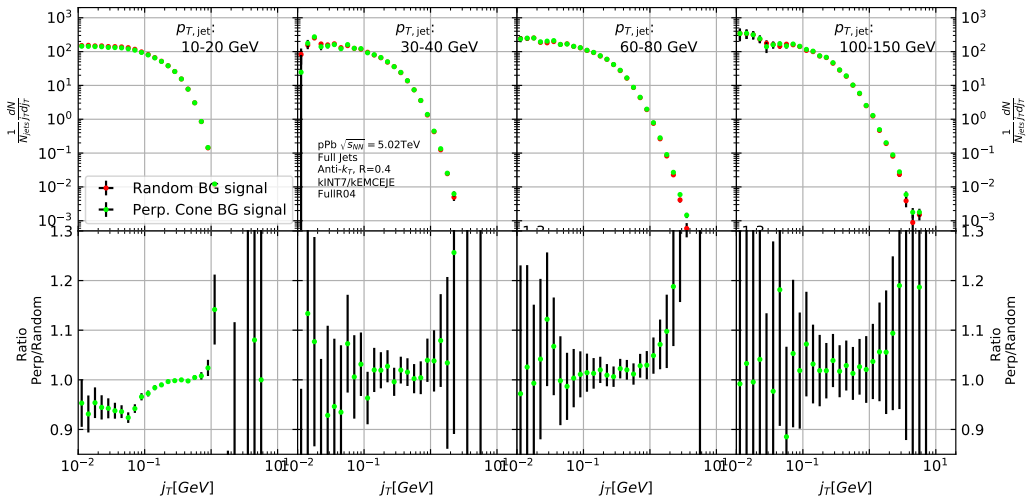


Figure 47: Comparison of the effect of background method on j_T signal.

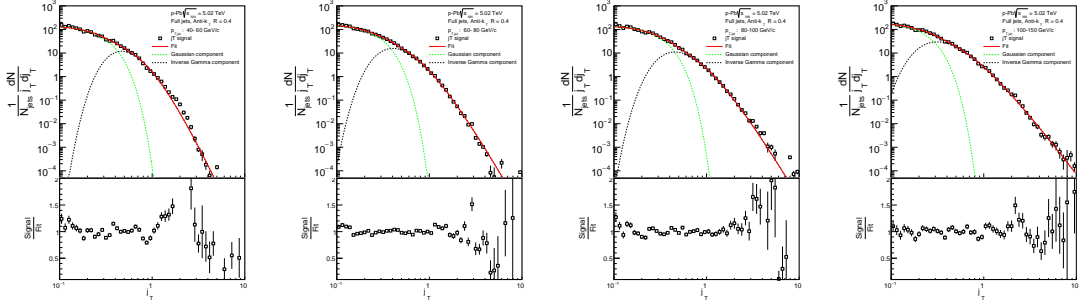


Figure 48: j_T signal fits in different jet p_T bins

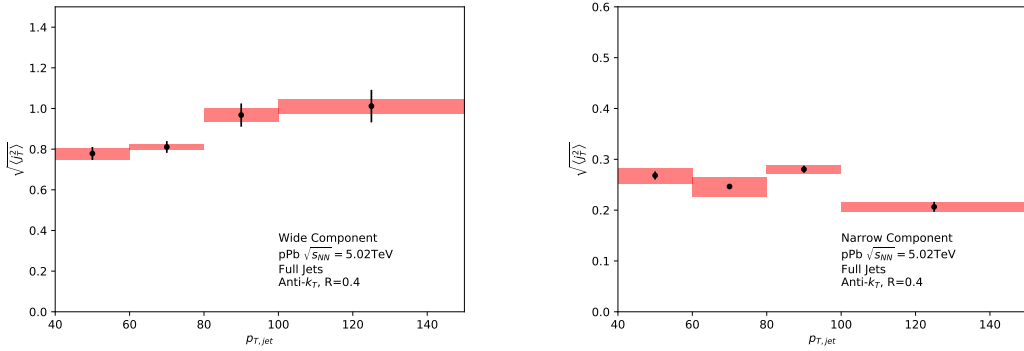


Figure 49: RMS values extracted from the fits for the gaussian (narrow) and inverse gamma (wide) components

1715 Comparison to j_T results from dihadron analysis [?] is shown in figure 56.
 1716 Trigger p_T bins used in dihadron analysis are converted to jet p_T bins using ob-
 1717 served average jet p_T values in leading track momentum bins. Similarly jet p_T bins
 1718 are converted to $p_{T,trigger}$ bins using average leading track p_T values in $p_{T,jet}$ bins.

1719 The trends are similar in dihadron and jet j_T results. Wide component RMS
 1720 values tend to increase with increasing $p_{T,trigger}/p_{T,jet}$. Narrow component RMS
 1721 increases slightly in dihadron analysis but not in jet j_T , WHY? (Depends on $x_{||}$
 1722 bin in dihadron)

1723 In general dihadron j_T gives wider distributions with larger RMS values. In
 1724 jet analysis the cone size limits width and thus the RMS values. The effect of this
 1725 limitation can be studied by changing the cone size as is described in section 9.9.

1726 Additionally the leading track is an imperfect estimate of the jet/original par-
 1727 ton. Because the leading track in general is at an angle compared to the jet axis,
 1728 the resulting j_T values are different. In practice the jet axis found by the jet finding
 1729 algorithm tends to minimize the average j_T of jet constituents. Thus the yield at

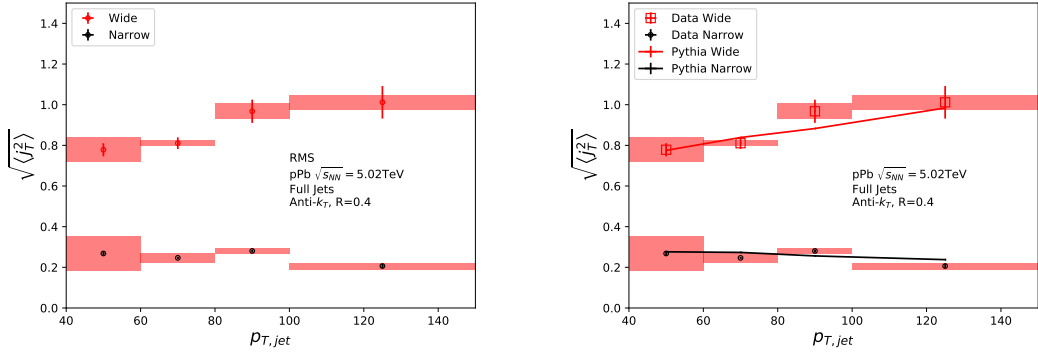


Figure 50: RMS values extracted from the fits for the gaussian (narrow) and inverse gamma (wide) components

¹⁷³⁰ high j_T is limited and the RMS values are smaller.

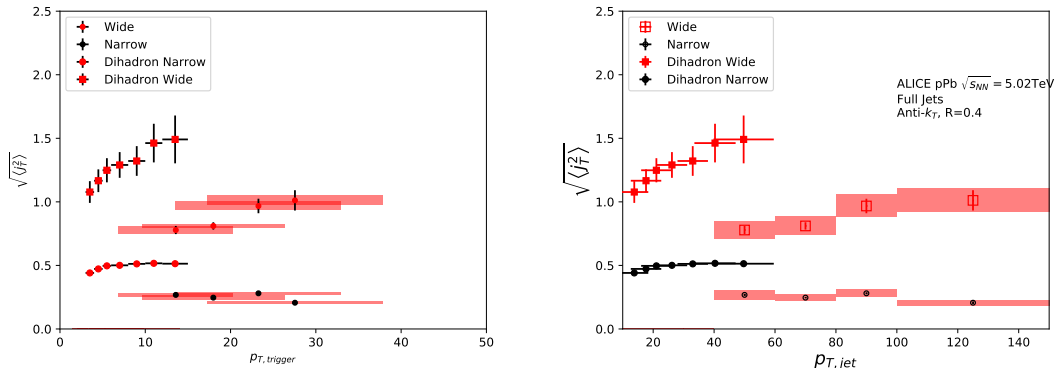


Figure 51: Jet j_T results are compared to results obtained in the dihadron analysis. This is done both in jet p_T and trigger p_T bins by converting between them.

¹⁷³¹ 9.9 Different R parameters

¹⁷³² Study the effect of cone sizes on j_T distribution in particle level Pythia.

¹⁷³³ Increasing the cone size of jets gives more room for high j_T tracks. This is seen
¹⁷³⁴ in the individual j_T distributions as increased high j_T production. At low j_T there
¹⁷³⁵ is no change.

¹⁷³⁶ When looking at RMS values from wide component we see an increase/decrease
¹⁷³⁷ of about 10% when going from $R = 0.4$ to $R = 0.5/R = 0.3$.

1738 The message from narrow component RMS values is less clear. At low jet p_T
 the behaviour is similar, but at high p_T the order is reversed.

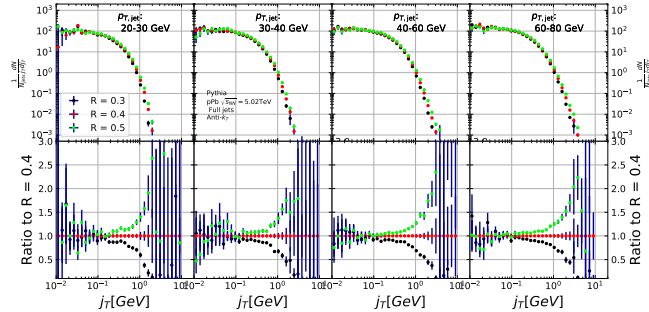


Figure 52: Effect of changing R parameter in jet finding on j_T distributions

1739

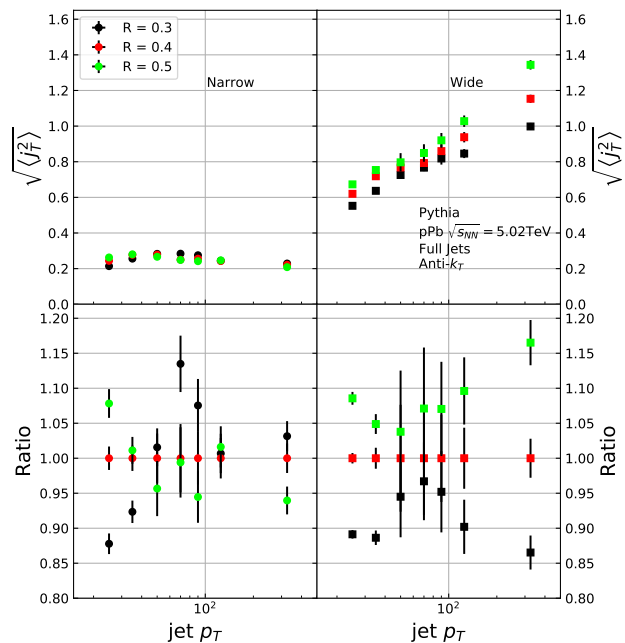


Figure 53: Effect of changing R parameter in jet finding on narrow and wide component RMS values. Wide component RMS values increase with increasing cone size.

1740 10 Discussion

1741 10.1 Discussion

1742 10.1.1 Dihadron j_T

1743 The jet fragmentation transverse momentum j_T has been studied previously at
 1744 ALICE with dihadron correlations [2]. The study took the leading hadron in
 1745 each event and calculated j_T for any near-side tracks with respect to the leading
 1746 hadron. Thus there is no kinematical limit to j_T from the jet cone. In the analysis
 1747 the background shape is estimated using pairs with large $\Delta\eta$. The normalisation of
 1748 the background is done when fitting the j_T distribution. The inclusive and signal
 1749 distributions from the analysis are shown in Fig. 54. The inclusive distribution is
 1750 fitted with a three component function,

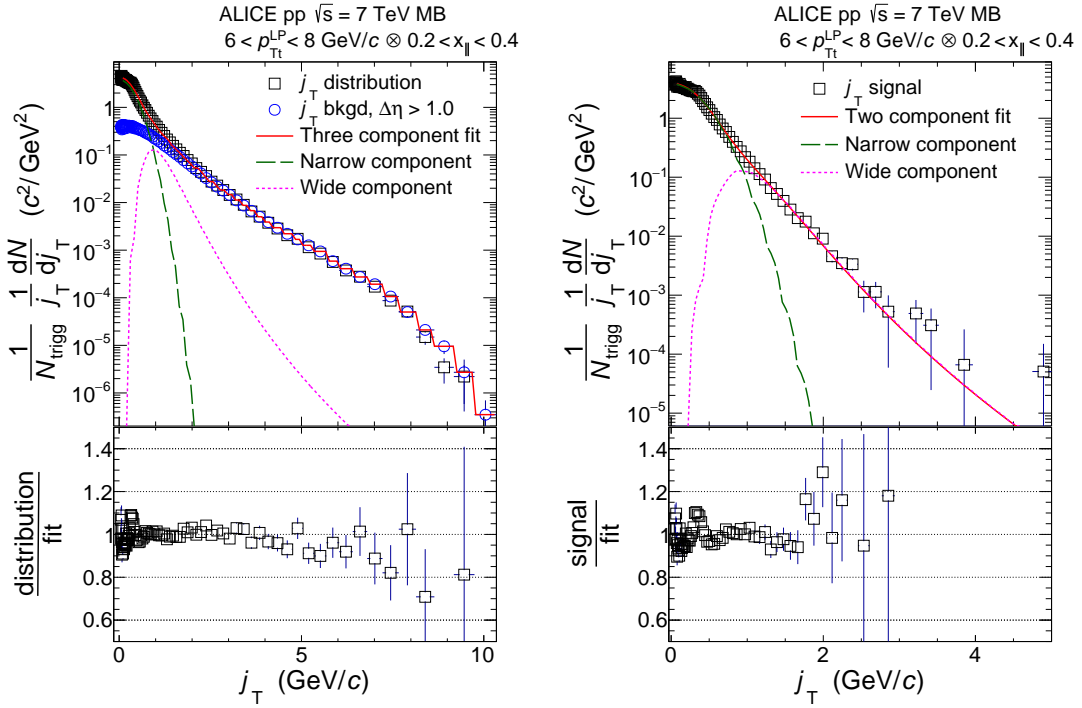


Figure 54: *Left:* Measured j_T distribution including a three-component fit. The three components describe the background (circular symbols), hadronization (long dashed line), and showering (short dashed line). *Right:* The same j_T distribution but with background subtracted.

1751 The analysis was the first to introduce this factorisation of j_T into components.
 1752 At $j_T \approx 0.4 \text{ GeV}$ there is a small bump in the distribution to fit ratio. This
 1753 was attributed to cases where the trigger particle decayed after hadronisation. As

it is difficult to correct for, this bump is included in the systematic errors of the results.

The RMS results from the fitting in both pp and p-Pb collisions are shown in Fig. 55. Qualitatively the results are similar to jet j_T results. The RMS value of the wide component has an increasing trend with respect to p_{Tt}/p_{Tjet} , while the RMS value of the narrow component stays constant. Both components are well described by PYTHIA simulations.

In the dihadron analysis there is no difference between pp and p-Pb results.

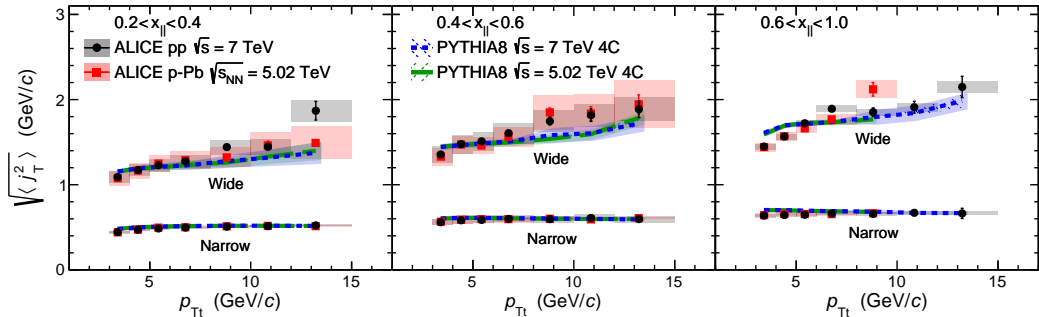


Figure 55: RMS values of the narrow and wide j_T components in the dihadron correlation analysis. Results from pp collisions at $\sqrt{s} = 7$ TeV (circular symbols) and from p-Pb collisions at $\sqrt{s_{NN}} = 5.02$ TeV (square symbols) are compared to PYTHIA 8 tune 4C simulations at $\sqrt{s} = 7$ TeV (short dashed line) and at $\sqrt{s} = 5.02$ TeV (long dashed line). Different panels correspond to different x_{\parallel} bins with $0.2 < x_{\parallel} < 0.4$ on the left, $0.4 < x_{\parallel} < 0.6$ in the middle, and $0.6 < x_{\parallel} < 1.0$ on the right. The statistical errors are represented by bars and the systematic errors by boxes. [2]

Comparison between jet and dihadron j_T results shown in Fig. 56. Trigger p_T bins used in dihadron analysis are converted to jet p_T bins using observed average jet p_T values in leading track momentum bins. Similarly jet p_T bins are converted to $p_{T\text{trigger}}$ bins using average leading track p_T values in $p_{T\text{jet}}$ bins.

In general dihadron j_T gives wider distributions with larger RMS values. There are several factors that could explain this. In jet analysis the cone size limits width and thus the RMS values. With increasing cone size one gets increasing wide RMS values as seen in Fig. 57. This should be the dominant factor.

Effect of the R parameter choice is studied in PYTHIA. Having a fixed cone puts hard limits on the possible j_T values. Increasing the cone size loosens these limits and allows higher j_T values. The results are shown in Fig. 57. Left hand side shows the j_T distributions. There is very little change in low j_T but at high j_T the yield increases.

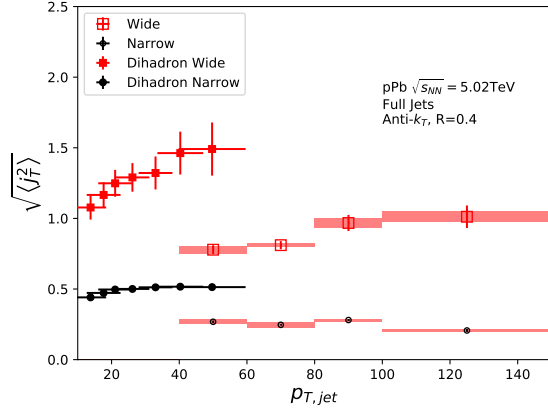


Figure 56: Comparison of results with dihadron j_T results. Dihadron trigger p_T bins are converted to jet p_T bins using observed mean $p_{T,jet}$ values in $p_{T,trigger}$ bins. Dihadron results are for $0.2 < x_{||} < 0.4$

This is also seen in the RMS values shown in the right hand side of Fig. 57, where the change in wide component RMS is about 10% when going from $R = 0.4$ to $R = 0.3$ or $R = 0.5$. With the narrow component values the situation is less clear. At low jet p_T larger R parameter leads to larger RMS values, but at high $p_{T,jet}$ the situation is reversed; increasing the R parameter decreases RMS values.

Additionally the leading track is an imperfect estimate of the jet/original parton. Because the leading track in general is at an angle compared to the jet axis, the resulting j_T values are different. In practice the jet axis found by the jet finding algorithm tends to minimize the average j_T of jet constituents. Thus the yield at high j_T is limited and the RMS values are smaller.

A PYTHIA study was performed where j_T was calculated with respect to the leading track momentum, instead of the jet axis. The results are shown in Fig. 58. The resulting j_T distributions are significantly wider than j_T distributions from the typical method. The effect seems to be larger than the effect seen in comparing different R values.

Lastly the results from the dihadron analysis are done in $p_{T,trigger}$ bins. This favours hard jets, i.e. jets where the leading hadron carries a large momentum fraction and the jet multiplicity is small. In $p_{T,jet}$ bins jets are more likely to be soft, i.e. small leading momentum fraction and high multiplicity jets.

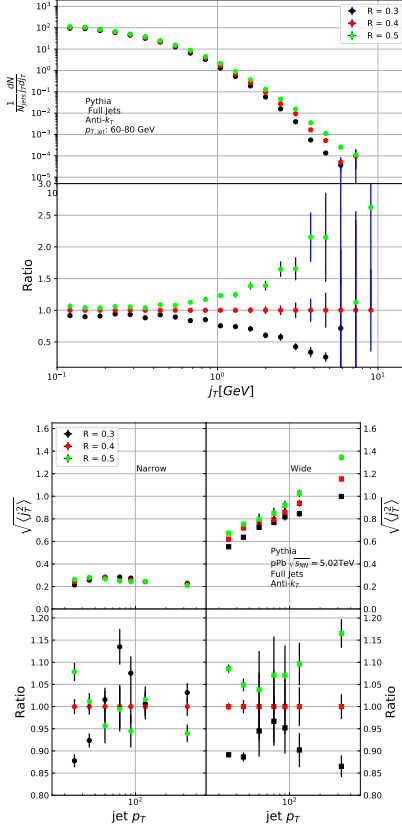


Figure 57: Effect of changing R parameter in jet finding on j_T distributions

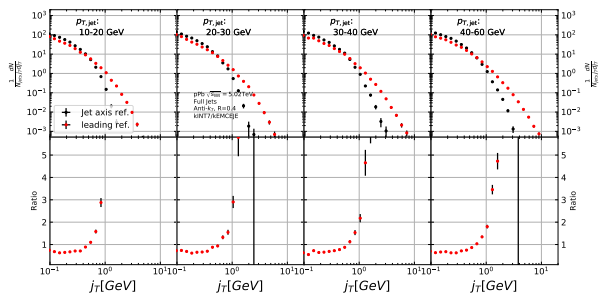


Figure 58: Results of calculating j_T with respect to the jet axis or the leading hadron. The assumption is that because the leading hadron is an imperfect estimate of the jet axis, low j_T tracks should on average be shifted to higher j_T

₁₇₉₄ **11 Summary**

₁₇₉₅ In this work two distinct j_T components were extracted for narrow and wide contri-
₁₇₉₆ butions using jet reconstruction. RMS values for both components were obtained.
₁₇₉₇ The width of the wide component is found to increase for increasing $p_{T\text{jet}}$. This
₁₇₉₈ is in part explained by the changing kinematical limits when going to higher $p_{T\text{jet}}$
₁₇₉₉ which allows higher $p_{T\text{track}}$. Additionally the larger phase space allows stronger
₁₈₀₀ parton splitting. The results are qualitatively compatible with previous studies
₁₈₀₁ that studied j_T using two-particle correlations.

₁₈₀₂ **References**

- ₁₈₀₃ [1] ALICE, J. Adam *et al.*, Phys. Rev. **C91**, 064905 (2015), 1412.6828.
- ₁₈₀₄ [2] <https://alice-publications.web.cern.ch/node/3655>, 2018.
- ₁₈₀₅ [3] PHENIX Collaboration, K. Adcox *et al.*, Nucl.Phys. **A757**, 184 (2005), nucl-ex/0410003.
- ₁₈₀₆
- ₁₈₀₇ [4] STAR Collaboration, J. Adams *et al.*, Nucl.Phys. **A757**, 102 (2005), nucl-ex/0501009.
- ₁₈₀₈
- ₁₈₀₉ [5] J.-Y. Ollitrault, Phys. Rev. D **46**, 229 (1992).
- ₁₈₁₀ [6] U. Heinz and P. Kolb, Nucl. Phys. **A702**, 269 (2002).
- ₁₈₁₁ [7] E. Shuryak, Prog. Part. Nucl. Phys. **62**, 48 (2009).
- ₁₈₁₂ [8] ATLAS Collaboration, J. Jia, Nucl.Phys.A904-905 **2013**, 421c (2013), 1209.4232.
- ₁₈₁₃
- ₁₈₁₄ [9] R. A. Lacey *et al.*, (2012), 1207.1886.
- ₁₈₁₅ [10] R. Bjorklund, W. Crandall, B. J. Moyer, and H. York, Phys. Review **77**, 213 (1950).
- ₁₈₁₆
- ₁₈₁₇ [11] W. Heisenberg, Zeitschrift für Physik **77**, 1 (1932).
- ₁₈₁₈ [12] M. Gell-Mann, Phys. Rev. **125**, 1067 (1962).
- ₁₈₁₉ [13] M. Gell-Mann, Phys. Lett. **8**, 214 (1964).
- ₁₈₂₀ [14] O. Greenberg, Phys. Rev. Lett. **13**, 598 (1964).
- ₁₈₂₁ [15] Crystal Ball Collaboration, D. Williams *et al.*, Phys.Rev. **D38**, 1365 (1988).
- ₁₈₂₂ [16] W. Krolikowski, Nuovo Cim. **A27**, 194 (1975).
- ₁₈₂₃ [17] D. J. Gross and F. Wilczek, Physical Review Letters **30**, 1343 (1973).
- ₁₈₂₄ [18] H. D. Politzer, Physical Review Letters **30**, 1346 (1973).
- ₁₈₂₅ [19] D. J. Gross and F. Wilczek, Physical Review D **8**, 3633 (1973).
- ₁₈₂₆ [20] D. J. Gross and F. Wilczek, Physical Review D **9**, 980 (1974).
- ₁₈₂₇ [21] H. Georgi and H. D. Politzer, Physical Review D **9**, 416 (1974).

- ₁₈₂₈ [22] H. Fritzsch, M. Gell-Mann, and H. Leutwyler, Physics Letters B **47**, 365
₁₈₂₉ (1973).
- ₁₈₃₀ [23] I. Flegel and P. Söding, CERN courier (2004).
- ₁₈₃₁ [24] R. Brandelik *et al.*, Physics Letters B **86**, 243 (1979).
- ₁₈₃₂ [25] J. K. L. MacDonald, Phys. Rev. **43**, 830 (1933).
- ₁₈₃₃ [26] C. Berger *et al.*, Physics Letters B **86**, 418 (1979).
- ₁₈₃₄ [27] J. Collins and M. Perry, Phys. rev. Lett. **34**, 1353 (1975).
- ₁₈₃₅ [28] E. Shuryak, Phys. Reps. **61**, 71 (1980).
- ₁₈₃₆ [29] K. Rajagopal, SLAC Beam Line **31-2**, 9 (2001).
- ₁₈₃₇ [30] P. Kovtun, D. Son, and A. Starinets, Phys.Rev.Lett. **94**, 111601 (2005),
₁₈₃₈ hep-th/0405231.
- ₁₈₃₉ [31] R. A. Lacey *et al.*, Phys. Rev. Lett. **98**, 092301 (2007).
- ₁₈₄₀ [32] E. Lofgren, *ACCELERATOR DIVISION ANNUAL REPORTS, 1 JULY*
₁₈₄₁ *1972 12/31/1974* (, 1975).
- ₁₈₄₂ [33] D. S. Barton, Heavy ion program at bnl: Ags, rhic, in *Proc. 1987 Particle*
₁₈₄₃ *Accelerator Conference, Washington, D.C., March, 1987*, 1987.
- ₁₈₄₄ [34] I. Vitev and M. Gyulassy, Phys.Rev.Lett. **89**, 252301 (2002), hep-
₁₈₄₅ ph/0209161.
- ₁₈₄₆ [35] S. Choi and K. S. Lee, Phys. Rev. C **84**, 064905 (2011).
- ₁₈₄₇ [36] A. Kovalenko *et al.*, Status of the nuclotron, in *Proceedings of EPAC Vol. 94*,
₁₈₄₈ pp. 161–164, 1994.
- ₁₈₄₉ [37] NA61/SHINE, K. Grebieszkow, PoS **CPOD2013**, 004 (2013).
- ₁₈₅₀ [38] BRAHMS Collaboration, I. Arsene *et al.*, Nucl.Phys. **A757**, 1 (2005), nucl-
₁₈₅₁ ex/0410020.
- ₁₈₅₂ [39] B. Back *et al.*, Nucl.Phys. **A757**, 28 (2005), nucl-ex/0410022.
- ₁₈₅₃ [40] S. A. Voloshin, A. M. Poskanzer, and R. Snellings, (2008), 0809.2949.
- ₁₈₅₄ [41] S. A. Voloshin, A. M. Poskanzer, A. Tang, and G. Wang, Phys.Lett. **B659**,
₁₈₅₅ 537 (2008), 0708.0800.

- ₁₈₅₆ [42] H. Holopainen, H. Niemi, and K. J. Eskola, Phys.Rev. **C83**, 034901 (2011), 1007.0368.
- ₁₈₅₈ [43] ALICE Collaboration, Phys. Rev. C **88**, 044909 (2013).
- ₁₈₅₉ [44] M. L. Miller, K. Reygers, S. J. Sanders, and P. Steinberg, Ann.Rev.Nucl.Part.Sci. **57**, 205 (2007), nucl-ex/0701025.
- ₁₈₆₁ [45] R. Glauber, Lectures in theoretical physics, 1959.
- ₁₈₆₂ [46] W. Czyż and L. Maximon, Annals of Physics **52**, 59 (1969).
- ₁₈₆₃ [47] A. Białas, M. Bleszyński, and W. Czyż, Nuclear Physics B **111**, 461 (1976).
- ₁₈₆₄ [48] PHENIX Collaboration, S. Afanasiev *et al.*, Phys.Rev. **C80**, 054907 (2009), 0903.4886.
- ₁₈₆₆ [49] J.-Y. Ollitrault, Eur.J.Phys. **29**, 275 (2008), 0708.2433.
- ₁₈₆₇ [50] P. Romatschke, Int.J.Mod.Phys. **E19**, 1 (2010), 0902.3663.
- ₁₈₆₈ [51] L. LD, Izv. Akad. Nauk Ser. Fiz. **17**, 51 (1953).
- ₁₈₆₉ [52] H. Song, S. Bass, and U. W. Heinz, (2013), 1311.0157.
- ₁₈₇₀ [53] H. Niemi, G. Denicol, P. Huovinen, E. Molnar, and D. Rischke, Phys.Rev. **C86**, 014909 (2012), 1203.2452.
- ₁₈₇₂ [54] K. A. *et al.* [ALICE Collaboration], Phys. Rev. Lett **106** (2011), 032301.
- ₁₈₇₃ [55] J.-Y. Ollitrault, Phys.Rev. D **48**, 1132 (1993), hep-ph/9303247.
- ₁₈₇₄ [56] P. Danielewicz and G. Odyniec, Physics Letters B **157**, 146 (1985).
- ₁₈₇₅ [57] P. Danielewicz and M. Gyulassy, Physics Letters B **129**, 283 (1983).
- ₁₈₇₆ [58] T. Abbott *et al.*, Phys. Rev. Lett. **70**, 1393 (1993).
- ₁₈₇₇ [59] S. Voloshin and Y. Zhang, Z.Phys. **C70**, 665 (1996), hep-ph/9407282.
- ₁₈₇₈ [60] E877 Collaboration, J. Barrette *et al.*, Phys.Rev.Lett. **73**, 2532 (1994), hep-ex/9405003.
- ₁₈₈₀ [61] CMS Collaboration, S. Chatrchyan *et al.*, Phys.Rev.Lett. **109**, 022301 (2012), 1204.1850.

- ₁₈₈₂ [62] Y. I. Azimov, Y. L. Dokshitzer, V. A. Khoze, and S. I. Trovan, Zeitschrift
₁₈₈₃ für Physik C Particles and Fields **27**, 65 (1985).
- ₁₈₈₄ [63] B. Andersson, G. Gustafson, G. Ingelman, and T. Sjöstrand, Physics Reports
₁₈₈₅ **97**, 31 (1983).
- ₁₈₈₆ [64] A. Buckley *et al.*, Phys. Rept. **504**, 145 (2011), 1101.2599.
- ₁₈₈₇ [65] M. Bahr *et al.*, Eur. Phys. J. **C58**, 639 (2008), 0803.0883.
- ₁₈₈₈ [66] A. Kurkela and U. A. Wiedemann, Phys. Lett. **B740**, 172 (2015), 1407.0293.
- ₁₈₈₉ [67] R. Baier, Y. L. Dokshitzer, A. H. Mueller, S. Peigne, and D. Schiff, Nucl.
₁₈₉₀ Phys. **B484**, 265 (1997), hep-ph/9608322.
- ₁₈₉₁ [68] W. H. H. Bethe and, Proc.Roy.Soc.Lond. **A146** (1934).
- ₁₈₉₂ [69] L. D. Landau and I. Pomeranchuk, Dokl. Akad. Nauk Ser. Fiz. **92**, 535
₁₈₉₃ (1953).
- ₁₈₉₄ [70] A. B. Migdal, Phys. Rev. **103**, 1811 (1956).
- ₁₈₉₅ [71] P. Bosted *et al.*, Quantum-mechanical suppression of bremsstrahlung*, 1993.
- ₁₈₉₆ [72] A. Majumder and M. Van Leeuwen, Prog.Part.Nucl.Phys. **A66**, 41 (2011),
₁₈₉₇ 1002.2206.
- ₁₈₉₈ [73] F. Dominguez, C. Marquet, A. Mueller, B. Wu, and B.-W. Xiao, Nucl.Phys.
₁₈₉₉ **A811**, 197 (2008), 0803.3234.
- ₁₉₀₀ [74] M. Gyulassy, P. Levai, and I. Vitev, Nucl.Phys. **B571**, 197 (2000), hep-
₁₉₀₁ ph/9907461.
- ₁₉₀₂ [75] U. A. Wiedemann, Nucl.Phys. **B588**, 303 (2000), hep-ph/0005129.
- ₁₉₀₃ [76] P. B. Arnold, G. D. Moore, and L. G. Yaffe, JHEP **0112**, 009 (2001), hep-
₁₉₀₄ ph/0111107.
- ₁₉₀₅ [77] X.-N. Wang and X.-f. Guo, Nucl.Phys. **A696**, 788 (2001), hep-ph/0102230.
- ₁₉₀₆ [78] T. Sjostrand, S. Mrenna, and P. Z. Skands, Comput.Phys.Commun. **178**,
₁₉₀₇ 852 (2008), 0710.3820.
- ₁₉₀₈ [79] I. Lokhtin and A. Snigirev, Eur.Phys.J. **C45**, 211 (2006), hep-ph/0506189.
- ₁₉₀₉ [80] N. Armesto, L. Cunqueiro, and C. A. Salgado, Nucl.Phys. **A830**, 271C
₁₉₁₀ (2009), 0907.4706.

- ₁₉₁₁ [81] K. Zapp, G. Ingelman, J. Rathsman, J. Stachel, and U. A. Wiedemann, Eur.Phys.J. **C60**, 617 (2009), 0804.3568.
- ₁₉₁₃ [82] T. Renk, Phys.Rev. **C79**, 054906 (2009), 0901.2818.
- ₁₉₁₄ [83] ALICE Collaboration, K. Aamodt *et al.*, Phys.Lett. **B696**, 30 (2011), 1012.1004.
- ₁₉₁₆ [84] WA98 Collaboration, M. Aggarwal *et al.*, Eur.Phys.J. **C23**, 225 (2002), nucl-ex/0108006.
- ₁₉₁₈ [85] D. G. d'Enterria, Phys.Lett. **B596**, 32 (2004), nucl-ex/0403055.
- ₁₉₁₉ [86] PHENIX Collaboration, A. Adare *et al.*, Phys.Rev.Lett. **101**, 232301 (2008), 0801.4020.
- ₁₉₂₁ [87] STAR Collaboration, J. Adams *et al.*, Phys.Rev.Lett. **91**, 172302 (2003), nucl-ex/0305015.
- ₁₉₂₃ [88] A. Dainese, C. Loizides, and G. Paic, Eur.Phys.J. **C38**, 461 (2005), hep-ph/0406201.
- ₁₉₂₅ [89] I. Vitev, J.Phys. **G30**, S791 (2004), hep-ph/0403089.
- ₁₉₂₆ [90] C. A. Salgado and U. A. Wiedemann, Phys.Rev. **D68**, 014008 (2003), hep-ph/0302184.
- ₁₉₂₈ [91] N. Armesto, A. Dainese, C. A. Salgado, and U. A. Wiedemann, Phys.Rev. **D71**, 054027 (2005), hep-ph/0501225.
- ₁₉₃₀ [92] T. Renk, H. Holopainen, R. Paatelainen, and K. J. Eskola, Phys.Rev. **C84**, 014906 (2011), 1103.5308.
- ₁₉₃₂ [93] CMS Collaboration, S. Chatrchyan *et al.*, Eur.Phys.J. **C72**, 1945 (2012), 1202.2554.
- ₁₉₃₄ [94] PHENIX Collaboration, S. Afanasiev *et al.*, Phys. Rev. C **80**, 054907 (2009).
- ₁₉₃₅ [95] ALICE Collaboration, K. Aamodt *et al.*, Phys.Rev.Lett. **108**, 092301 (2012), 1110.0121.
- ₁₉₃₇ [96] J. L. Nagle and W. A. Zajc, Ann. Rev. Nucl. Part. Sci. **68**, 211 (2018), 1801.03477.
- ₁₉₃₉ [97] E735, T. Alexopoulos *et al.*, Phys. Rev. **D48**, 984 (1993).

- ¹⁹⁴⁰ [98] MiniMax, T. C. Brooks *et al.*, Phys. Rev. **D61**, 032003 (2000), hep-ex/9906026.
- ¹⁹⁴¹
- ¹⁹⁴² [99] C. Shen, Z. Qiu, and U. Heinz, Phys. Rev. **C92**, 014901 (2015), 1502.04636.
- ¹⁹⁴³ [100] PHENIX, A. Adare *et al.*, Phys. Rev. **C94**, 064901 (2016), 1509.07758.
- ¹⁹⁴⁴ [101] C. A. Salgado and J. P. Wessels, Ann. Rev. Nucl. Part. Sci. **66**, 449 (2016).
- ¹⁹⁴⁵ [102] M. Gyulassy, I. Vitev, X.-N. Wang, and B.-W. Zhang, p. 123 (2003), nucl-th/0302077.
- ¹⁹⁴⁶
- ¹⁹⁴⁷ [103] E. Norbeck, K. Šafařík, and P. A. Steinberg, Annual Review of Nuclear and Particle Science **64**, 383 (2014), <https://doi.org/10.1146/annurev-nucl-102912-144532>.
- ¹⁹⁴⁸
- ¹⁹⁴⁹
- ¹⁹⁵⁰ [104] A. Accardi, F. Arleo, W. K. Brooks, D. D'Enterria, and V. Muccifora, Riv. Nuovo Cim. **32**, 439 (2010), 0907.3534.
- ¹⁹⁵¹
- ¹⁹⁵² [105] ALICE, K. Aamodt *et al.*, JINST **3**, S08002 (2008).
- ¹⁹⁵³ [106] ALICE, B. B. Abelev *et al.*, Int. J. Mod. Phys. **A29**, 1430044 (2014), 1402.4476.
- ¹⁹⁵⁴
- ¹⁹⁵⁵ [107] ALICE, K. Aamodt *et al.*, JINST **5**, P03003 (2010), 1001.0502.
- ¹⁹⁵⁶ [108] J. Alme *et al.*, Nucl. Instrum. Meth. **A622**, 316 (2010), 1001.1950.
- ¹⁹⁵⁷ [109] ALICE, B. Abelev *et al.*, JHEP **03**, 053 (2012), 1201.2423.
- ¹⁹⁵⁸ [110] ALICE, P. Cortese *et al.*, (2008).
- ¹⁹⁵⁹ [111] J. Allen *et al.*, Report No. CERN-LHCC-2010-011. ALICE-TDR-14-add-1, 2010 (unpublished).
- ¹⁹⁶⁰
- ¹⁹⁶¹ [112] ALICE, G. Dellacasa *et al.*, (1999).
- ¹⁹⁶² [113] ALICE Collaboration, *Technical Design Report on Forward Detectors: FMD, T0 and V0*, 2004.
- ¹⁹⁶³
- ¹⁹⁶⁴ [114] ALICE, B. Abelev *et al.*, Phys. Lett. **B719**, 29 (2013), 1212.2001.
- ¹⁹⁶⁵ [115] 2019.
- ¹⁹⁶⁶ [116] T. ALICE Collaboration *et al.*, Journal of Instrumentation **3**, S08002 (2008).

- ¹⁹⁶⁷ [117] for the ALICE, C. Zampolli, Particle Identification with the ALICE detector at the LHC, in *Proceedings, PLHC2012: Physics at the LHC 2012 (PLHC2012): Vancouver, BC, Canada, June 4-9, 2012*, 2012, 1209.5637.
- ¹⁹⁷⁰ [118] M. Cacciari, G. P. Salam, and G. Soyez, Eur. Phys. J. **C72**, 1896 (2012), 1111.6097.
- ¹⁹⁷² [119] M. Cacciari, G. P. Salam, and G. Soyez, JHEP **04**, 063 (2008), 0802.1189.
- ¹⁹⁷³ [120] T. Sjöstrand, S. Mrenna, and P. Z. Skands, Comput. Phys. Commun. **178**, 852 (2008), 0710.3820.
- ¹⁹⁷⁵ [121] Roounfold: Root unfolding framework, <http://hepunx.rl.ac.uk/~adye/software/unfold/RooUnfold.html>, 2013.